École polytechnique de Louvain

Mutiscale modeling of the high cycle fatigue of thermoplastic polymer solids

Author: **Georgios Tsilimidos**
Supervisor: **Issam Doghri**
Readers: **Laurent Delannay, Mohamed Haddad, Domenico Magisano, Grzegorz Lesiuk**
Academic year 2023–2024
Master [120] in Mechanical Engineering

Acknowledgements

I would like first and foremost to thank my supervisor, Pr. Issam Doghri, for his continuous support and guidance. His insights and profound knowledge of the subject have been a constant source of motivation. I am deeply appreciative of all the opportunities he has provided.

I would like to extend my gratitude to Mohamed Haddad for his continuous encouragement and support throughout the work on this thesis. I am thankful for the time he dedicated to me.

Additionally, I would like to thank Anthony Hun for the engaging conversations we had and for the advice and guidance he provided.

I am also grateful to Chiheb Naili for his kindness and support.

Last but not least, I would like to thank my family, who has been a constant source of support. Special thanks to my parents and my brother, for their constant and unconditional support, without them I would not be here. I wish also to express my gratitude to my friends for their valuable advices and guidance in both professional and personal life. This work is dedicated to them.

Abstract

Accurate prediction of fatigue failure in thermoplastic polymer solids, especially those produced through additive manufacturing, remains challenging. Traditional models relying on macroscopic fatigue criteria fail to give accurate predictions of teh fatigue lifetime. This study introduces a novel methodology including microstructural details into fatigue predictions, specifically for materials manufactured using the Selective Laser Sintering (SLS) process.

The primary contribution is the development of a coupled time and space homogenization method for viscoelastic-viscoplastic (VEVP) composites under cyclic loading. This method demonstrates significant accuracy in predicting the response within material phases at a low computational cost, even for high cycle fatigue (HCF) scenarios.

The study utilizes a Representative Volume Element (RVE) modeling approach, assuming that in HCF, the majority of the material volume remains viscoelastic, with viscoplastic deformation accumulating at weak spots, which represent preexisting defects and inhomogeneities of the material. This approach effectively predicts interactions between weak spots and the matrix while maintaining computational efficiency.

The proposed model, while not always accurate, showed promising results that suggest it could be applied to a wide range of loading conditions with further refinement.

Overall, this work presents a valuable tool for engineers and researchers, far better than the phenomenological and empirical models commonly used in the industry for fatigue life assessment.

Abbreviations

MT Mori-Tanaka

VE Viscoelastic(ity)

VEVP Viscoelastic(ity)-Viscoplastic(ity)

VEVPD Viscoelastic(ity)-Viscoplastic(ity)-Damage(d)

MFH Mean-Field Homogenization

RVE Representative Volume Element

TPU Thermoplastic polyurethane

HCF High cycle fatigue

LCT Laplace Carson Transform

Notations

Symbols

$\dot{x}$	Time derivative.
$(\bullet)_M, \langle\bullet\rangle$	Average in time.
$\widetilde{(\bullet)}$	Fluctuation in time.
$\bar{(\bullet)}$	Average value over all the RVE.
$\langle.\rangle_\Omega$	Average value over all the volume Ω.
$\langle.\rangle_{\Omega_r}$	Average value over phase r.

Scalars and scalar-valued functions

t_M	Macro-chronological time.
τ	Micro-chronological time.
E	Young's modulus.
ν	Poisson's ratio.
σ_{eq}	von Mises equivalent stress.
σ_{eq}^{pred}	Trial equivalent stress.
f	Yield function.
$p, \dot{p}$	Accumulated plastic strain and its corresponding rate.
$R(p)$	Hardening function.
g_v	Viscoplastic function.
G_i	Shear modulus (weight) of i-th term of Prony series.

g_i	Shear relaxation time of i-th term of Prony series.
K_j	Bulk modulus (weight) of j-th term of Prony series.
k_j	Bulk relaxation time of j-th term of Prony series.
D	Damage scalar variable.

Second-order tensors

$\mathbf{1}$	Second-order identity tensor.
$\boldsymbol{\sigma}$	Cauchy stress tensor.
$\boldsymbol{\varepsilon}$	Infinitesimal strain tensor.
$\boldsymbol{\varepsilon}^{\boldsymbol{ve}}$	Viscoelastic strain tensor.
$\boldsymbol{\varepsilon}^{\boldsymbol{vp}}, \dot{\boldsymbol{\varepsilon}}^{\boldsymbol{vp}}$	Viscoplastic strain tensor and its corresponding rate.

Fourth-order tensors

$\mathbb{C}^{ve}$	Relaxation tensor.
$\mathbb{I}$	Symmetric fourth-order identity tensor.
$\mathbb{I}^{vol}$	Volumetric operator: $\mathbb{I}^{vol} \equiv \frac{1}{3}\mathbf{1} \otimes \mathbf{1}$.
$\mathbb{I}^{dev}$	Deviatoric operator: $\mathbb{I}^{dev} \equiv \mathbb{I} - \mathbb{I}^{vol}$.

Throughout the thesis, the following notations and conventions are used. Boldface symbols designate second- or fourth-rank tensors. The former are designated by lowercase symbols (e.g. $\boldsymbol{\sigma}$). The latter are denoted by uppercase symbols(e.g. $\mathbb{C}^{ve}$).
Einstein's summation convention over repeated indices (i, j, k or l) is used, unless otherwise indicated. Tensor operations are expressed as follows:

$$\boldsymbol{a} : \boldsymbol{b} = \boldsymbol{a}_{ij}\boldsymbol{b}_{ji}; \quad (\mathbb{C} : \boldsymbol{a})_{ij} = \mathbb{C}_{ijkl}\boldsymbol{a}_{lk};$$
$$\mathbb{C} :: \mathbb{D} = \mathbb{C}_{ijkl}\mathbb{D}_{lkji}; \quad (\boldsymbol{a} \otimes \boldsymbol{b})_{ijkl} = \boldsymbol{a}_{ij}\boldsymbol{b}_{kl};$$

Contents

List of Figures

Chapter 1

Introduction

1.1 Importance of fatigue analysis in polymer engineering

The importance of fatigue is evident: "although exact numbers are not available, it is expected that at least half of all mechanical failures are due to fatigue" [4]. As one can imagine, the cost to replace the structures that fail due to fatigue is substantial. Therefore, it is crucial to understand the physics of fatigue to establish a cause-and-effect relationship that can help reduce the likelihood of such failures.

Fatigue analysis is particularly important in polymer engineering due to the extensive use of polymer materials in various industrial applications. Polymers are popular for their light weight, corrosion resistance and ability to be manufactured in complex shapes. However, their mechanical performance, especially under cyclic loading conditions, is a significant concern. Understanding the fatigue behavior of polymers is essential for predicting their lifespan and ensuring the safety and reliability of polymer-based components. This analysis is very important in applications such as automotive, aerospace, consumer electronics, where materials are subjected to repeated loadings over their operational life.

From an experimental point of view, fatigue tests are both expensive and time-consuming, as it can take up to weeks just for a single test. Additionally, the loading conditions and specimen geometries are limited, failing to fully replicate the complex conditions of an actual part. On the other hand, numerical simulations can overcome these limitations and provide a more accurate approximation of the reality. However, the computational cost of fatigue modeling is very high, which can potentially make it impractical. Predicting the life span of a structure by solving a multi-scale problem that includes long-term effects through cyclic loading, complex geometries and the non-linear behavior of materials presents a great scientific challenge.

1.2 Background information on fatigue modeling of thermoplastic polymer solids

Fatigue modeling of thermoplastic polymers involves studying their response to cyclic loading, which can lead to material degradation and failure over time. Traditional approaches often assume homogeneous material properties and employ macroscopic approaches to predict fatigue life. However, polymers are inherently heterogeneous at the microstructural level, containing porosity and defects that influence their fatigue behavior.

It should be pointed out that, although many experimental studies on thermoplastic polymers have been conducted, the current knowledge about these materials is limited, especially compared to the understanding of metals.

The fatigue of polymers typically occurs in two main stages. The first stage involves the gradual degradation of the material's mechanical properties until a crack initiates and the second stage the propagation of the crack up to the final fracture of the structure.

Recent advancements in computational methods have enabled more accurate predictions by incorporating multiscale approaches. Hun et al. [1] proposed an efficient modeling procedure for viscoelastic solids subjected to large numbers of loading cycles by extending the Laplace-Carson transform method. A time-homogenization method was developed by Haouala & Doghri [3] for the calculation of the response under a high number of cycles with limited computational burden. The work of Haddad et al. [2] presented an incremental secant MFH scheme for accurate predictions in the case of VEVP RVEs. Finally, a previous Master thesis demonstrated effective methodologies for fatigue modeling using homogeneous materials and emphasized the importance of computational efficiency in predicting fatigue life. However, these approaches do not fully capture the localized damage mechanisms observed in real-world applications.

There have been some promising attempts to model the fatigue of thermoplastic polymers in a multiscale manner. Among these, the work of Krairi et al. [5] stands out. In this study, a novel RVE modeling approach was proposed to model HCF, achieving good predictions.

1.3 Present work

1.3.1 Motivation

Additive manufacturing techniques have emerged in recent years allowing to produce structures with complex geometries and enhanced properties. More specifically, selective laser sintering (SLS) was intensively used in industry to fabricate polymer-based structure with high quality. Additionally, several research projects were initiated to study structures fabricated using the SLS process. One of these is the European funded MOAMMM (Multi-scale Optimisation for Additive Manufacturing of fatigue resistant shock-absorbing MetaMaterials) project. This project involve multiple academic and industrial partners across Europe which are the following :

- University of Liege
- Université Catholique de Louvain
- IMDEA Materials Institute
- Johannes Kepler Universität Linz
- cirp GmbH

This objective throughout this collaborative project is to produce and study lattice structures manufactured using SLS for applications such as shoe soles. Examples of lattices are depicted in figure 1.1. They consist of architectural structures constituted by one unit cell repeated periodically over its domain. Shoe soles are particular structures which are subjected to repeated loading along their lifetime. Their mechanical behavior does not encounter any alteration in the short term. However, beyond a certain number of repeated loading cycles, the mechanical properties start to change until reaching the total failure of the structures named "high cycle fatigue (HCF)". Experimental measurements were carried out in [6] to study the HCF of lattices. Those measurements are very time consuming and require special tools to be achieved. In this study, the objective is to propose an alternative efficient framework that allows to predict HCF of polymer structures fabricated using the SLS process. The methodology we developed is purely computational, permitting to to predict the fatigue life of thermoplastic polymers and surpass the limitation of intensive experimental measurements.

1.3.2 Objectives of the study

Several works in the literature studied the fatigue of structures, considering various materials and usage conditions. In [5, 7] a coupled viscoelastic-viscoplastic-damage (VE-VP-D) model was proposed to predict the HCF of homogeneous materials. [8] proposed a time homogenization approach to predict the HCF behavior of VE-VP homogeneous material without requiring the full discretization over the time scale. However, all the studies consider a fatigue criteria at macroscopic level. This is not adequate for lattice structure fabricated using the SLS process. In fact, [9] demonstrated the existence of pores at microscopic level within the

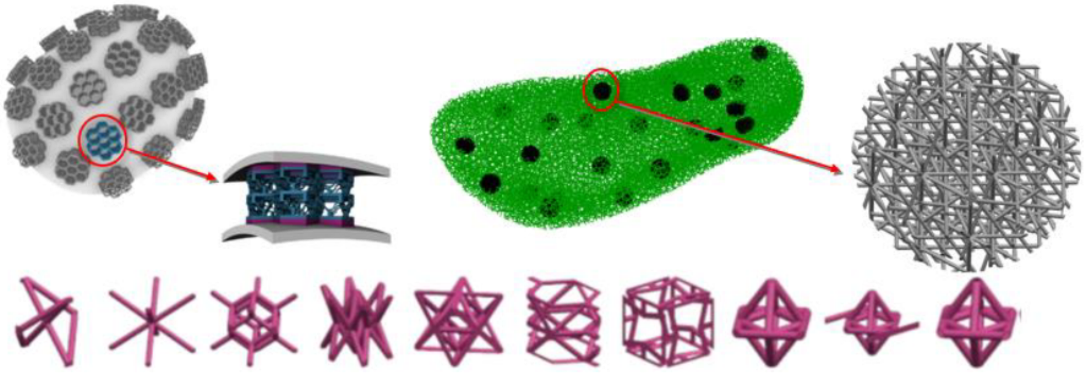

Figure 1.1: Lattice structures of MOAMM project.

fabricated structures. Those micro-pores considerably affect the overall behavior in short and long terms. Additionally, experimental observations revealed that the structures are not fully homogeneous. Certain regions exhibit some weaknesses compared to others, thereby constituting the zones where degradation mechanisms are initiated. The modeling of such aspects requires more tailored models based on local aspects and not global ones as in the existing models. This work aims to improve the accuracy and efficiency of fatigue predictions for materials produced through additive manufacturing. To overcome the limitations and weaknesses of existing models, the primary objectives of this study are:

1. Instead of working with a homogeneous material, develop a model that incorporates microstructural details.

2. Implement a local damage model at the level of the defects that are responsible for the failure, as opposed to a macroscopic damage model.

3. Couple time and space homogenization methods to decrease computational cost of fatigue simulations.

4. Validate the proposed model against experimental results.

1.3.3 Outline of the thesis

The present thesis is structured in the following way. Chapter 2 presents some general aspects that will later be used in the methodology. The constitutive VEVP model is presented along with the employed damage model. Laplace-Carson transform is presented that will be employed for the solution of the structural problem. Then, some of the key components of mean-field homogenization will be discussed. An overview of the time homogenization method follows and the chapter concludes with some basic terminology of fatigue tests.

Chapter 3 includes the main contribution of this work. First, the RVE modeling approach is motivated and the basic assumptions are listed. Then, the extensive details of the coupled time and space homogenization method are presented. Finally, the post-processing of the results using the damage criterion for calculating the lifetime is presented, along with the optimization problem for determining the optimal damage parameters.

Chapter 4 gathers the results obtained with the developed codes. First, the code is validated in the case of homogeneous and heterogeneous RVEs and the results are compared with the ones obtained from Haouala & Doghri [3] and Haouala [8]. Finally, the fatigue predictions of the proposed methodology and the comparison with experimental results are given.

Chapter 2

Generalities

The objective of this section is to present the prerequisites needed to develop a coupled time and space homogenization method. First, a VEVP constitutive model, which is able to capture the time-dependent reversible and irreversible parts of the deformation of the polymer material. Then, the key principles of MFH for two-phase linear thermo-elastic composites are presented. This step is the basis of the space homogenization method. Next, a short description of the key ideas of the time homogenization method are given. Then, the coupling between space and time homogenization is motivated. Finally, the basic terminology of fatigue tests is presented.

2.1 Viscoelastic-viscoplastic constitutive model

The constitutive model proposed in [10], which can capture rate and time-dependent responses of polymer materials, is adopted in the present study. The model is based on the classical assumption that strain can be subdivided into VE and VP parts:

$$\boldsymbol{\varepsilon} = \boldsymbol{\varepsilon}^{ve} + \boldsymbol{\varepsilon}^{vp} \tag{2.1}$$

2.1.1 Viscoelastic strain

The Cauchy stress is related to the time-history of VE strains via a linear model expressed by Boltzmann's integral:

$$\boldsymbol{\sigma}(t) = \int_{-\infty}^{t} \mathbb{C}^{ve}(t-\eta) : \frac{\partial \boldsymbol{\varepsilon}^{ve}}{\partial \eta} d\eta \tag{2.2}$$

For an isotropic material, the fourth rank relaxation tensor takes the following form:

$$\mathbb{C}^{ve}(t) = 2G(t)\mathbb{I}^{dev} + 3K(t)\mathbb{I}^{vol} \tag{2.3}$$

The shear $G(t)$ and bulk $K(t)$ relaxation moduli have the form of Prony series:

$$G(t) = G_\infty + \sum_{i=1}^{I} G_i \exp\left(-\frac{t}{g_i}\right) \tag{2.4a}$$

$$K(t) = K_\infty + \sum_{j=1}^{J} K_j \exp\left(-\frac{t}{k_j}\right) \tag{2.4b}$$

By substituting Equations (2.3)–(2.4) into Equation (2.2), a decomposition of the stress tensor into deviatoric $\mathbf{s}(t)$ and dilatational $\sigma_H(t)$ parts, and the strain tensor into deviatoric $\boldsymbol{\xi}(t)$ and dilatational $\varepsilon_H(t)$ parts is obtained:

$$\mathbf{s}(t) = 2G_\infty \boldsymbol{\xi}^{ve}(t) + \sum_{i=1}^{I} \mathbf{s}_i(t) \tag{2.5a}$$

$$\sigma_H(t) = 3K_\infty \varepsilon_H^{ve}(t) + \sum_{j=1}^{J} \sigma_{H_j}(t) \tag{2.5b}$$

where the viscous stresses are defined by:

$$\mathbf{s}_i(t) = 2G_i \exp\left(-\frac{t}{g_i}\right) \int_{-\infty}^{t} \exp\left(\frac{\eta}{g_i}\right) \frac{\partial \boldsymbol{\xi}^{ve}(\eta)}{\partial \eta} d\eta \tag{2.6a}$$

$$\sigma_{H_j}(t) = 3K_j \exp\left(-\frac{t}{k_j}\right) \int_{-\infty}^{t} \exp\left(\frac{\eta}{k_j}\right) \frac{\partial \varepsilon_H^{ve}(\eta)}{\partial \eta} d\eta \tag{2.6b}$$

Then, equation (2.5) leads to the following expression of the stress tensor:

$$\boldsymbol{\sigma}(t) = \mathbb{C}_\infty : \boldsymbol{\varepsilon}^{ve}(t) + \sum_{i=1}^{I} \mathbf{s}_i(t) + \sum_{j=1}^{J} \sigma_{H_j}(t)\mathbf{1} \tag{2.7}$$

where, $\mathbb{C}_\infty = 2G_\infty \mathbb{I}^{dev} + 3K_\infty \mathbb{I}^{vol}$, is the long-term elastic Hooke's operator.

2.1.2 Viscoplastic strain

For a J_2 VP model with isotropic hardening, the yield function is given as follows:

$$f(\boldsymbol{\sigma}, R(p)) = \sigma_{eq} - (\sigma_y + R(p)); \quad \sigma_{eq} = \sqrt{\frac{3}{2}\mathbf{s} : \mathbf{s}}, \tag{2.8}$$

where σ_{eq} is the von-Mises equivalent stress and $R(p)$ the hardening stress. There are two forms of the hardening function $R(p)$ considered in the subsequent simulations, which are defined as:

$$\text{Power-law:} \quad R(p) = k_1 p^n \tag{2.9a}$$

$$\text{Mixed linear-exponential law:} \quad R(p) = k_1 p + k_2(1 - e^{-np}) \tag{2.9b}$$

where the parameters k_1 $[Pa]$, k_2 $[Pa]$ and n represent the two hardening moduli and the hardening exponent, respectively. The number of the hardening moduli defined indicates which of the two models is used each time.

The accumulated plastic strain p is an internal variable which keeps track of the past history of the VP strain:

$$p(t) = \int_0^t \dot{p}(\eta) d\eta; \quad \dot{p} = \sqrt{\frac{2}{3} \dot{\boldsymbol{\varepsilon}}^{vp} : \dot{\boldsymbol{\varepsilon}}^{vp}} \tag{2.10}$$

The VP strain rate obeys an associated plastic flow rule:

$$\dot{\boldsymbol{\varepsilon}}^{vp} = \dot{p} \frac{\partial f}{\partial \boldsymbol{\sigma}} = \dot{p} \mathbf{N} \tag{2.11}$$

The normal to the yield surface is given by $\mathbf{N} = \frac{3}{2} \frac{\mathbf{s}}{\sigma_{eq}}$ in the case of J_2 plasticity. The plastic multiplier $\dot{p}$ is defined by a viscoplastic potential:

$$\dot{p} = C(\boldsymbol{\sigma}, p) = \begin{cases} g_v(\sigma_{eq}, p), & f > 0 \\ 0, & \text{otherwise} \end{cases} \tag{2.12}$$

In the present study, the modified Norton's power law is adopted for the VP function:

$$g_v(\sigma_{eq}, p) = \kappa \left(\frac{f}{\sigma_y + R(p)} \right)^m, \tag{2.13}$$

where κ $[s^{-1}]$ and m are the viscoplastic modulus and exponent, respectively.

2.2 Fatigue criterion - Damage model

Continuum Damage Mechanics (CDM), which represents a local approach to failure, is one of the most widely used tools to predict material failure and is adopted here. The ultimate phase of the damage evolution is detected by a local criterion and corresponds to a macro-crack initiation and material failure. The idea of this work is to use a damage model, which is based on physics, rather than an empirical formula to predict fatigue failure. However, it should be pointed out that,

although in the constitutive model presented in [5] the damage is coupled with the viscoelasticity and viscoplasticity, in the present work the damage is assumed completely decoupled. The necessity of this simplification will be clear later.
The CDM approach is based on the concept of damage variable $D(t)$ and effective stress $\hat{\boldsymbol{\sigma}}(t)$. The relation between the Cauchy stress $\boldsymbol{\sigma}(t)$ and the effective stress $\hat{\boldsymbol{\sigma}}(t)$ is:

$$\hat{\boldsymbol{\sigma}}(t) = \frac{\boldsymbol{\sigma}}{1 - D(t)} \tag{2.14}$$

The evolution of damage is driven by the damage thermodynamic force $Y(t)$ (or the strain energy density release rate, as known in CDM). It is associated with the damage variable D and it is defined as:

$$Y(t) = \frac{1}{2} \int_{-\infty}^{t} \int_{-\infty}^{t} \frac{\partial \boldsymbol{\varepsilon}^{ve}(\zeta)}{\partial \zeta} : \mathbb{C}^{ve}(2t - \zeta - \eta) : \frac{\partial \boldsymbol{\varepsilon}^{ve}(\eta)}{\partial \eta} \, d\zeta \, d\eta \tag{2.15}$$

Using Equations (2.4)–(2.7) along with the definition of effective stress (2.14), a remarkably simple expression of the damage thermodynamic force Y is found:

$$Y = \frac{\hat{\mathbf{s}}_\infty : \hat{\mathbf{s}}_\infty}{4G_\infty} + \frac{(\hat{\sigma}_{H_\infty})^2}{2K_\infty} + \sum_{i=1}^{I} \frac{\hat{\mathbf{s}}_i : \hat{\mathbf{s}}_i}{4G_i} + \sum_{j=1}^{J} \frac{(\hat{\sigma}_{H_j})^2}{2K_j}, \tag{2.16}$$

where the variables $\hat{\mathbf{s}}_\infty$, $\hat{\sigma}_{H_\infty}$, $\hat{\mathbf{s}}_i$ and $\hat{\sigma}_{H_j}$ are the corresponding effective counterparts of $\mathbf{s}_\infty$, σ_{H_∞}, $\mathbf{s}_i$ and σ_{H_j}, according to Equation (2.14).

The evolution of the damage variable obeys the Lemaitre-Chaboche damage evolution law:

$$\dot{D} = \begin{cases} \left(\frac{Y}{S}\right)^s \dot{p} \geq 0 & \text{if } p > p_D \\ D = D_c & \rightarrow \text{crack initiation} \end{cases} \tag{2.17}$$

Here, p_D is a damage threshold, D_c is a critical damage value, and s and S are material parameters.

2.3 Laplace-Carson Transform

2.3.1 General VE problem

Let's consider the mechanical structural problem under the assumption of a quasi-static loading conditions, without ageing, under small perturbations and in linear viscoelasticity. A VE solid body occupying a domain Ω with boundary $\Gamma = \Gamma_u \cup \Gamma_t$ is subjected to boundary displacements $\mathbf{u}_b$ on Γ_u and tractions $\mathbf{t}$ on Γ_t. The problem is expressed as follows:

VE problem in time domain

Boundary conditions:

$$\mathbf{u}(\mathbf{x},t) = \mathbf{u}_b(\mathbf{x},t), \quad \text{on } \Gamma_u \tag{2.18a}$$
$$^t\boldsymbol{\sigma}(\mathbf{x},t)\cdot\mathbf{n} = \mathbf{t}(\mathbf{x},t), \quad \text{on } \Gamma_t \tag{2.18b}$$

Equilibrium equation:

$$\nabla\cdot\boldsymbol{\sigma}(\mathbf{x},t) = \mathbf{0}, \quad \text{in } \Omega \tag{2.19}$$

Kinematic compatibility:

$$\boldsymbol{\varepsilon}(\mathbf{x},t) = \frac{1}{2}\left(\nabla\mathbf{u}(\mathbf{x},t) + {}^t\nabla\mathbf{u}(\mathbf{x},t)\right), \quad \text{in } \Omega \tag{2.20}$$

Constitutive equation:

$$\boldsymbol{\sigma}(\mathbf{x},t) = \int_{-\infty}^{t} \mathbb{C}^{ve}(\mathbf{x},t-\eta) : \frac{\partial\boldsymbol{\varepsilon}(\mathbf{x},\eta)}{\partial\eta}d\eta, \quad \text{in } \Omega \tag{2.21}$$

2.3.2 LCT computational method

In order to accelerate the computational time to access to the structural solution, Hun et al. in [1] propose a methodology to solve efficiently the VE problem under a large number of cycles. The key idea is to transform the mechanical time problem of Equations (2.18)–(2.21) into the Laplace-Carson domain p. The L-C transformation of a function f is defined as:

$$\mathcal{L}_p\{f(t)\} = f^*(p) = p\int_0^\infty f(t)e^{-pt}dt \tag{2.22}$$

Remarkably, the transformation of the convolution of two functions is simply the product of their transforms. This means that the nonlinear VE problem in time domain is transformed into a linear elastic problem in the L-C domain, as follows:

Elastic problem in L-C domain

Boundary conditions:

$$\mathbf{u}^\star(\mathbf{x},p) = \mathbf{u}_b^\star(\mathbf{x},p), \quad \text{on } \Gamma_u \tag{2.23a}$$
$$^t\boldsymbol{\sigma}^\star(\mathbf{x},p)\cdot\mathbf{n} = \mathbf{t}^\star(\mathbf{x},p), \quad \text{on } \Gamma_t \tag{2.23b}$$

Equilibrium equation:

$$\nabla \cdot \boldsymbol{\sigma}^{\star}(\mathbf{x}, p) = \mathbf{0}, \quad \text{in } \Omega \tag{2.24}$$

Kinematic compatibility:

$$\boldsymbol{\varepsilon}^{\star}(\mathbf{x}, p) = \frac{1}{2}\left(\nabla \mathbf{u}(\mathbf{x}, p) + {}^{t}\nabla \mathbf{u}^{\star}(\mathbf{x}, p)\right), \quad \text{in } \Omega \tag{2.25}$$

Constitutive equation:

$$\boldsymbol{\sigma}^{\star}(\mathbf{x}, p) = \mathbb{C}^{\star}(\mathbf{x}, p) : \boldsymbol{\varepsilon}^{\star}(\mathbf{x}, p), \quad \text{in } \Omega \tag{2.26}$$

The boundary conditions ($\mathbf{b} = \mathbf{u}_b$ or $\mathbf{b} = \mathbf{t}$) are split as follows :

$$\mathbf{b}(\mathbf{x}, t) = \breve{\mathbf{b}}(\mathbf{x}, t) + \widehat{\mathbf{b}}(\mathbf{x}, t), \quad \forall \mathbf{x} \text{ on } \Gamma \tag{2.27}$$

This decomposition of the loading signal is used to apply the superposition principle to cumulate the transient response due to the $\widehat{\mathbf{b}}$ function expressed as :

$$\widehat{b}_i(t) = \widehat{A}_i \left(1 - e^{-t/\widehat{\theta}_i}\right), \tag{2.28}$$

and the periodic response according to the sinus loading $\breve{\mathbf{b}}$ as :

$$\breve{b}_i(t) = \breve{A}_i \sin\left(\breve{\omega}_i t + \breve{\phi}_i\right) \tag{2.29}$$

where $\widehat{\theta} << \breve{\omega}$ (in mathematical sense), to approximate a Heaviside function by an exponential function in order to use a continuous function in L-C domain.

Each subproblem (associated to transient/periodic boundaries condition) needs a particular LCT inversion treatment to recover the solution in time :

- The transient subproblem will use the Schapery LCT inversion (see Section 2.3.3),
- The periodic subproblem will use the LCT inversion method based on the sinus basis decomposition (see Section 2.3.4).

The methodology is schematized in Figure 2.1. The numerical implementation details and the excellent accuracy of this method are reported in [1].

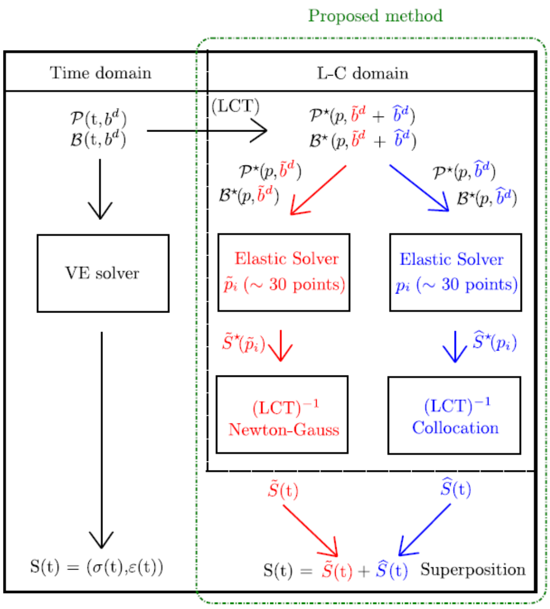

Figure 2.1: FE simulation strategy of VE structure under cyclic loading. Left : direct time domain computation to obtain reference solution. Right : procedure in L-C domain followed by split numerical inversion for LCT, adopted from [1].

2.3.3 Schapery's collocation method

The numerical inversion of the transient subproblem is accomplished with the collocation method of Schapery. In this framework the solution f of the problem in time t is defined as a series of exponentials such that :

$$f(t) = A + Bt + \sum_{k=1}^{N} C_k \left(1 - e^{-t/\theta_k}\right) \tag{2.30}$$

This decomposition is parameterized by the set $(\mathrm{A}, \mathrm{B}, C_k, \theta_k)$. This decomposition is adapted to represent both the classical phenomena of creep $(\theta_k < 0)$ and relaxation $(\theta_k > 0)$ related to a VE behavior. This decomposition in time of the f solution has its analogous form $f^\star$ in the L-C domain by successive transformation of each term such that :

$$f^\star(p) = A + \frac{B}{p} + \sum_{k=1}^{N} C_k \frac{1}{1 + p\theta_k} \tag{2.31}$$

The solution of this subproblem solved in LC domain is identified on the function basis described in Equation (2.31) and the set of parameters $(\mathrm{A}, \mathrm{B}, C_k, \theta_k)$.

2.3.4 LCT inversion method for sinusoidal functions

In LCT inversion method for sinusoidal functions proposed in [1], the authors defined the solution f of the problem in time t as a sine series such that :

$$f(t) = \sum_{k=1}^{N} a_k \sin(\omega_k t + \phi_k) \tag{2.32}$$

with the set $\mathbf{A_k} = (a_k, \omega_k, \phi_k)$ of parameters to be identified, which are respectively the amplitude, the pulsation and the shift of the approached function. The analogous form in L-C domain of this projection basis is defined as :

$$f^{\star}(p) = \sum_{k=1}^{N} \left\{ a_k \frac{p^2}{\omega_k^2 + p^2} \sin(\phi_k) + a_k \frac{\omega_k p}{\omega_k^2 + p^2} \cos(\phi_k) \right\} \tag{2.33}$$

The solution function $f^{\star}$ is then estimated on several discrete points p_i and an algorithm allows the identification of the set $\mathbf{A_k}$ and the reconstruction in the time domain.

2.4 Generalities of Mean-Field Homogenization

2.4.1 MFH in thermo-elasticity

Let's consider the homogenization of a two-phase composite whose constituents exhibit a linear thermoelastic behavior.

$$\boldsymbol{\sigma}(\mathbf{x}) = \mathbb{C}_r : \boldsymbol{\varepsilon}(\mathbf{x}) + \boldsymbol{\beta}_r(\mathbf{x}), \quad \forall \mathbf{x} \in \Omega_r \tag{2.34}$$

$\mathbb{C}_r$ is the elastic stiffness tensor in phase Ω_r and $\boldsymbol{\beta}_r$ is the eigenstress tensor due to thermal expansion. Subscripts 0 and 1 designate matrix and inclusion phases, respectively, Ω_0 and Ω_1 are the domains occupied by each phase and v_0 and v_1 their correspondent volume fractions.

In the multi-scale method depicted in Figure 2.2, the macro-point $\mathbf{X}$ is considered at the micro-scale as the center of a representative volume element (RVE) with domain Ω and boundary $\partial\Omega$. At this scale, the structure's heterogeneity is captured. The Hill-Mandel condition imposes energy equivalence between both scales, implying that, with appropriate boundary conditions, linking the macro stress $\bar{\boldsymbol{\sigma}}$ and strain $\bar{\boldsymbol{\varepsilon}}$ is equivalent to relating the volume-averaged over the RVE micro-stress $\langle \boldsymbol{\sigma} \rangle_{\Omega_r}$ and micro-strain $\langle \boldsymbol{\varepsilon} \rangle_{\Omega_r}$. This implies:

$$\bar{\boldsymbol{\sigma}}(\mathbf{X}) = v_0 \langle \boldsymbol{\sigma}(\mathbf{x}) \rangle_{\Omega_0} + v_1 \langle \boldsymbol{\sigma}(\mathbf{x}) \rangle_{\Omega_1} \tag{2.35a}$$

$$\bar{\boldsymbol{\varepsilon}}(\mathbf{X}) = v_0 \langle \boldsymbol{\varepsilon}(\mathbf{x}) \rangle_{\Omega_0} + v_1 \langle \boldsymbol{\varepsilon}(\mathbf{x}) \rangle_{\Omega_1} \tag{2.35b}$$

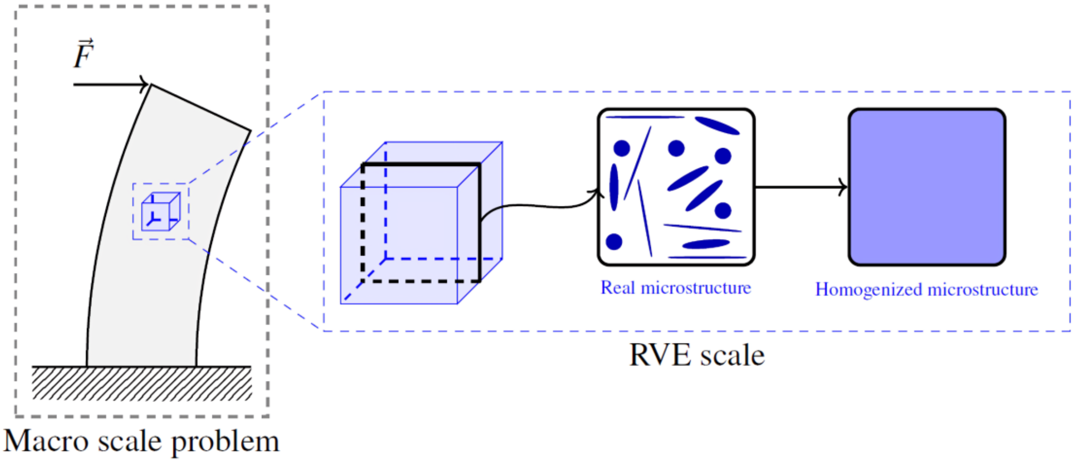

Figure 2.2: Change of scale in space, adopted from [2].

The main assumption of MFH in thermo-elasticity is that the average strains within phases are related using localization tensors $\mathbb{A}^{\varepsilon}$ and $\mathbf{a}^{\varepsilon}$ such that:

$$\langle \boldsymbol{\varepsilon}(\mathbf{x}) \rangle_{\Omega_1} = \mathbb{A}^{\varepsilon} : \bar{\boldsymbol{\varepsilon}} + \mathbf{a}^{\varepsilon} \tag{2.36}$$

Most of the definitions of localization tensors revolve around the extension of Eshelby's solution [11] for single inclusion to multiple inclusions interacting together in an average manner. The most widely used model is the Mori and Tanaka (M-T) scheme [12], which is accurate for thermo-elastic composites with moderate values of v_1. Consequently, it is adopted all along the present work. For identical and aligned inclusions, the M-T scheme leads to the partial strain concentration tensor $\mathbb{B}^{\varepsilon}$:

$$\mathbb{B}^{\varepsilon}(I, \mathbb{C}_0, \mathbb{C}_1) = \Big(\mathbb{I} + \boldsymbol{\Xi}(I, \mathbb{C}_0) : \mathbb{C}_0^{-1} : (\mathbb{C}_1 - \mathbb{C}_0)\Big)^{-1} \tag{2.37}$$

with $\boldsymbol{\Xi}(I, \mathbb{C}_0)$ representing Eshelby's tensor dependent on the matrix properties and the inclusions' shape designated by symbol I. Localization tensors from Equation (2.36) are defined as a function of $\mathbb{B}^{\varepsilon}$ such that:

$$\mathbb{A}^{\varepsilon} = \mathbb{B}^{\varepsilon} : [v_0\mathbb{I} + v_1\mathbb{B}^{\varepsilon}]^{-1} \tag{2.38a}$$

$$\mathbf{a}^{\varepsilon} = [\mathbb{A}^{\varepsilon} - \mathbb{I}] : [\mathbb{C}_1 - \mathbb{C}_0]^{-1} : [\boldsymbol{\beta}_1 - \boldsymbol{\beta}_0] \tag{2.38b}$$

The composite's macroscopic stiffness $\bar{\mathbb{C}}$ and eigenstress $\bar{\boldsymbol{\beta}}$ tensors are computed as follows:

$$\bar{\mathbb{C}} = [v_0\mathbb{C}_0 + v_1\mathbb{C}_1 : \mathbb{B}^{\varepsilon}] : [v_0\mathbb{I} + v_1\mathbb{B}^{\varepsilon}]^{-1} \tag{2.39a}$$

$$\bar{\boldsymbol{\beta}} = v_0\boldsymbol{\beta}_0 + v_1\boldsymbol{\beta}_1 + v_1\,[\mathbb{C}_1 - \mathbb{C}_0] : \mathbf{a}^{\varepsilon} \tag{2.39b}$$

2.4.2 Incremental secant method

The incremental-secant linearization method was pioneered by Wu et al. [13] for EP composites. It modifies the original secant formulation so that it is able to handle non-radial and non-monotonic loading histories. The method was extended to the case of VEVP phases by Haddad & Doghri [2].

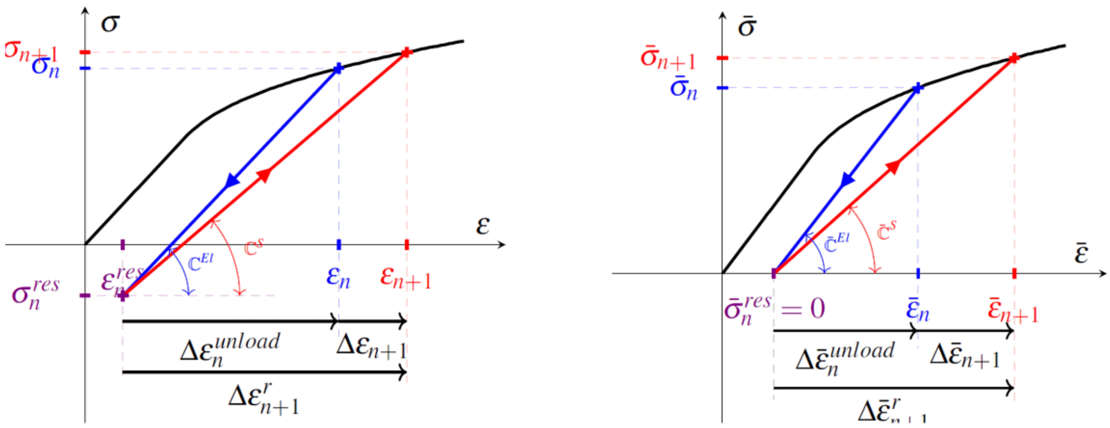

(a) In phases (b) Overall composite

Figure 2.3: Illustration of the incremental-secant linearization procedure (a) within the constitutive phases and (b) within the overall composite, adopted from [2].

Let's consider first a single material phase without homogenization. The solution is known until the beginning of the time step $[t_n, t_{n+1}]$ (state at time t_n, $St_n = (\boldsymbol{\sigma}_n, \boldsymbol{\varepsilon}_n, \boldsymbol{\varepsilon}_n^{vp}, p_n)$ is given). The material is subjected to strain increment $\Delta\boldsymbol{\varepsilon}_{n+1}$.
Following the incremental-secant procedure, the material is virtually unloaded at time t_n to an intermediate residual state $St_n^{res} = (\boldsymbol{\sigma}_n^{res}, \boldsymbol{\varepsilon}_n^{res}, \boldsymbol{\varepsilon}_n^{vp}, p_n)$ (see Figure 2.3). The unloaded state is defined such that:

$$\bar{\boldsymbol{\sigma}}_n^{res} = \mathbf{0} \tag{2.40}$$

The problem stated can be reformulated involving the newly created fictitious state as:

$$\boldsymbol{\varepsilon}_{n+1} = \boldsymbol{\varepsilon}_n + \Delta\boldsymbol{\varepsilon}_{n+1} \quad \longrightarrow \quad \boldsymbol{\varepsilon}_{n+1} = \boldsymbol{\varepsilon}_n^{res} + \Delta\boldsymbol{\varepsilon}_{n+1}^{r} \tag{2.41a}$$

$$\boldsymbol{\sigma}_{n+1} = \boldsymbol{\sigma}_n + \Delta\boldsymbol{\sigma}_{n+1} \quad \longrightarrow \quad \boldsymbol{\sigma}_{n+1} = \boldsymbol{\sigma}_n^{res} + \Delta\boldsymbol{\sigma}_{n+1}^{r} \tag{2.41b}$$

Consider now the overall composite material. Within the framework of the incremental-secant approach, the LCC is defined from the unloaded state such that the composite is subjected to homogenized strain increment $\Delta\varepsilon^r_{n+1}$ instead of $\Delta\varepsilon_{n+1}$ (see Figure 2.3). This implies:

$$\Delta\bar{\boldsymbol{\sigma}}^r_{n+1} = \bar{\mathbb{C}}^S : \Delta\bar{\boldsymbol{\varepsilon}}^r_{n+1}, \tag{2.42}$$

where $\bar{\mathbb{C}}^S$ is the RVE's secant operator.

2.5 Review of time homogenization method

Predicting the response of nonlinear materials under high frequency loadings requires significant computational resources, due to the very large number of required time integration increments. The time homogenization method, developed by Guennouni [14] for EVP homogeneous solids, enables to predict their response under a large number of cycles while simulating a much smaller number. The method was extended to the case of homogeneous VEVP material by Haouala & Doghri [3]. In this work, the time homogenization method is extended to the case of heterogeneous VEVP material.

2.5.1 Definition of two time scales

In Figure 2.4, a cyclic loading is plotted as a function of the physical time, t. If we look at the loading on a "macroscopic" time scale, t_M, we will see a smooth curve. Finally, if we "zoom" in we will see periodic fluctuations of period T. For instance, the macro-time t_M can be seen as a multiplier of T, and might correspond to the peaks of the imposed loads or displacements.

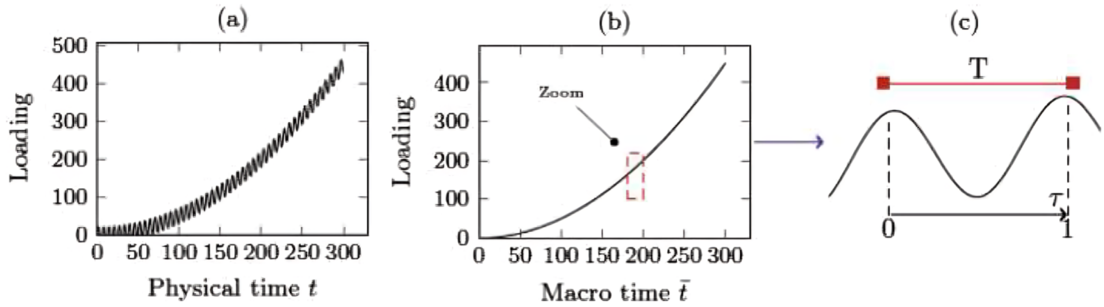

Figure 2.4: Macro and micro time coordinates (t: physical time, t_M: macro-time, T: load period, τ: micro-time $\tau \in [0, 1]$), adopted from [3].

We thus define two time scales. The first one corresponds to a natural time scale t_M that is characteristic of the long-term behaviour of the solution. The second one is a fine time-scale τ associated with the rapidly varying behaviour of the evolving variables resulting from the oscillating load.

The relation between the physical time t and the two time scales t_M and τ is defined as:

$$t = t_M + T\tau, \quad t_M \in [0, t_f] \quad \text{and} \quad \tau \in [0, 1] \tag{2.43}$$

Equation 2.43 is illustrated in Figure 2.5.

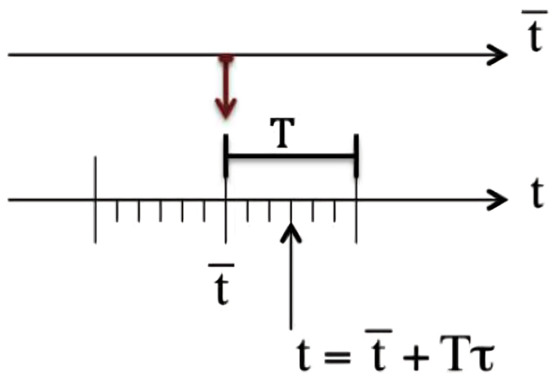

Figure 2.5: Relation between different time coordinates, adopted from [3].

All the response fields $\phi^T(\mathbf{x}, t)$ at a given spatial location $\mathbf{x}$ in a body Ω, subjected to cyclic loadings, are assumed to exhibit dependence on both time scales. They are then considered as a function of the two time variables t_M and τ, and are expressed as:

$$\phi^T(\mathbf{x}, t) = \phi(\mathbf{x}, t_M, \tau) \tag{2.44}$$

A superscript T associated with a variable denotes its association with the two time scales. Using Equation (35) and the chain rule, the time derivation in the two time scales is given as:

$$\dot{\phi}^T(\mathbf{x}, t) = \frac{\partial \phi(\mathbf{x}, t_M, \tau)}{\partial t_M} + \frac{1}{T}\frac{\partial \phi(\mathbf{x}, t_M, \tau)}{\partial \tau}, \tag{2.45}$$

where the superposed dot denotes the total derivative with respect to physical time t.

The average value $\phi_M(\mathbf{x}, t_M)$ of the function $\phi(\mathbf{x}, t_M, \tau)$ with respect to the fast time scale τ and at time t_M is defined as:

$$\phi_M(\mathbf{x}, t_M) = \int_0^1 \phi(\mathbf{x}, t_M, \tau) d\tau \equiv \langle \phi(\mathbf{x}, t_M, \tau) \rangle \tag{2.46}$$

A general decomposition of all variables ϕ into macroscopic ϕ_M and oscillatory $\tilde{\phi}$ portions is proposed in the form:

$$\phi(\mathbf{x}, t_M, \tau) = \phi_M(\mathbf{x}, t_M) + \tilde{\phi}(\mathbf{x}, t_M, \tau) \tag{2.47}$$

2.6 Basic terminology of fatigue tests

A fatigue test involves subjecting the material to repeated cyclic loading over many cycles until failure occurs. The cyclic loading is characterized by the stress amplitude σ_{amp}, the mean stress σ_{mean}, maximum and minimum stresses σ_{max} and σ_{min} and the loading ratio R. The relations between them are as follows:

$$\sigma_{amp} = \frac{\sigma_{max} - \sigma_{min}}{2}; \quad \sigma_{mean} = \frac{\sigma_{max} + \sigma_{min}}{2}; \quad R = \frac{\sigma_{min}}{\sigma_{max}}$$

Figure 2.6 shows the definitions of the terms that describe the cyclic loading of a standard stress controlled fatigue test. Instead of the stress σ, the displacement U can be used in a displacement controlled test to describe the loading level.

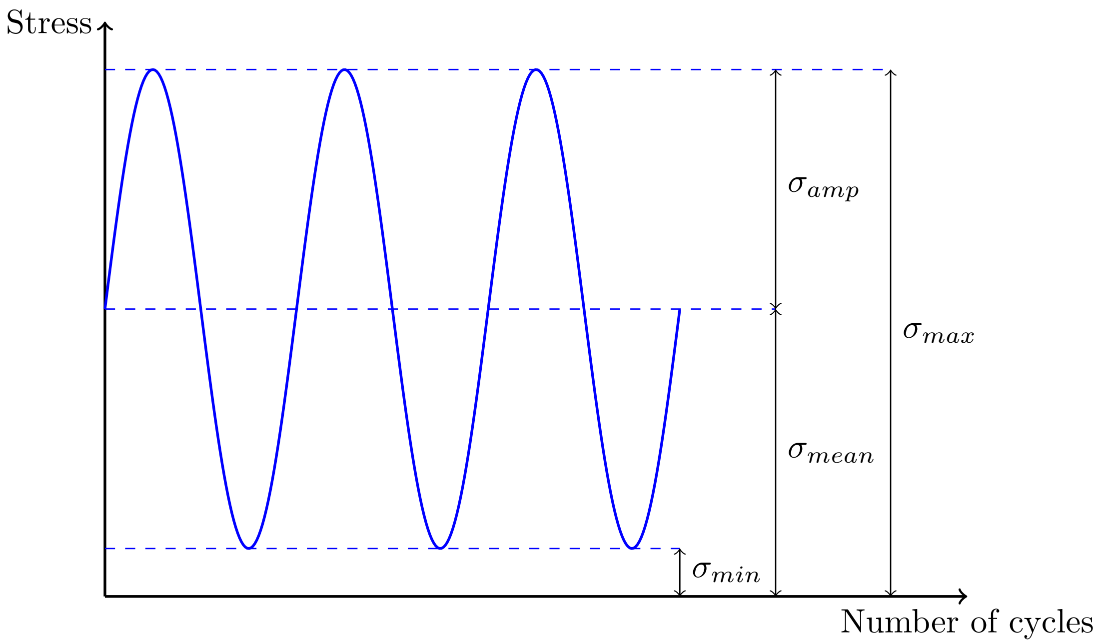

Figure 2.6: Cyclic loading terminology in a standard stress controlled fatigue test.

The fatigue tests are performed at various loading levels to capture the material's response to different amplitudes. The results are usually presented in the so-called S-N curve, which represents the relation between the loading level as a function of the number of cycles to failure N_f, in a logarithmic scale. Therefore, the S-N curve provides valuable insights into the material's fatigue life.

Chapter 3

Methodology

3.1 Multiscale modeling strategy

3.1.1 RVE description

To resolve the problem of High Cycle Fatigue (HCF) of thermoplastics, a multi-scale approach, within the framework of continuum damage mechanics (CDM), to predict the failure of the material was proposed in [7]. The damaged material is regarded as a matrix containing a small volume fraction (2%) of spherically shaped micro heterogenities, called also weakspots. These weakspots can be regarded as manufacturing defects in the material. A small (3%) porosity distribution is considered due to manufacturing process (e.g., selective laser sintering). Then, in order to compute the response inside the weakspots, the approach employs MFH homogenization techniques to predict the fracture of the material.

An illustration of the RVE description is given in Figure 3.1a. This modeling choice is supported experimentally, particularly in the case of SLS-printed polymers, which are the focus of the present work. This support is evident in micro-tomographic images (see Fig. 3.1b).

The main assumptions of the modeling approach, as listed in [7], are the following:

Assumption 1. *The matrix remains VE and the evolution of damage takes place only in the weakspots, which are VE-VP-D. The failure of the material happens when the damage within the weak spots reaches a critical value:* $D_{ws} = D_c$

Assumption 2. *Since the volume fraction of the weak-spots is low, their effect is assumed to be negligible at macroscale and macroscopically the material remains basically viscoelastic. However, the damage evolves at the scale of the weak spots.*

Assumption 3. *At the level of weak spots, the isotropic and kinematic hardening are neglected.*

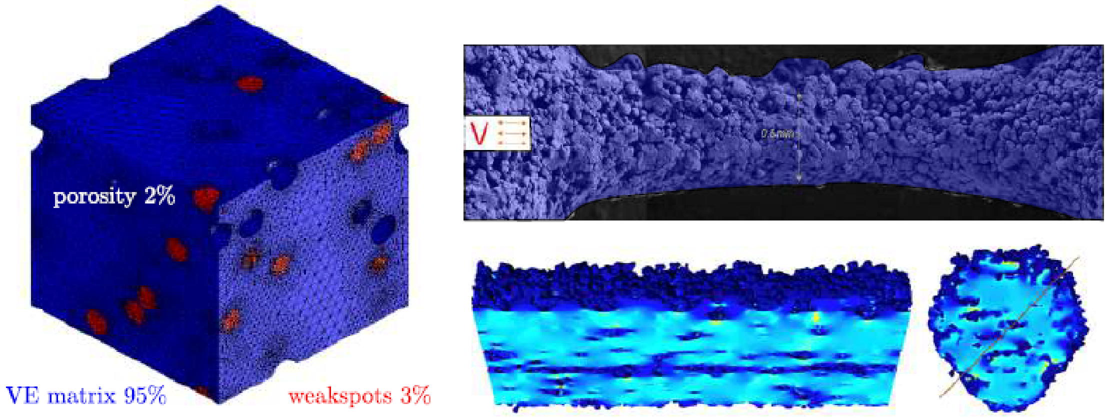

(a) RVE modeling (b) tomography cut of SLS material

Figure 3.1: RVE modeling motivation.

The necessity of the last assumption might not be clear, but it will be shown later that it is essential to avoid elastic shakedown, particularly for very small loading amplitudes.

3.1.2 Overview

This section gives a general description of the overall procedure and the details of each step will be given in the upcoming sections. An illustration of the modeling strategy is given in Figure 3.2. The steps of the proposed methodology are the following:

1. Structural level: Compute the macroscopic strain history at the critical points of the structure using the Laplace-Carson transform (details in Sections 3.1.3 and 2.3).

2. RVE level: Employ a coupled time and space homogenization method to compute the solution in the weakspots (details in Section 3.2). The applied loading is the one obtained from step 1.

3. Weakspots level: Compute the evolution of damage in the weakspots with a local damage model and calculate fatigue life (details in Section 3.3).

3.1.3 VE structural problem

It should be clear that the classical VEVP full-field simulation is not applicable from the computational point of view. Based on Assumption 2, the structure is

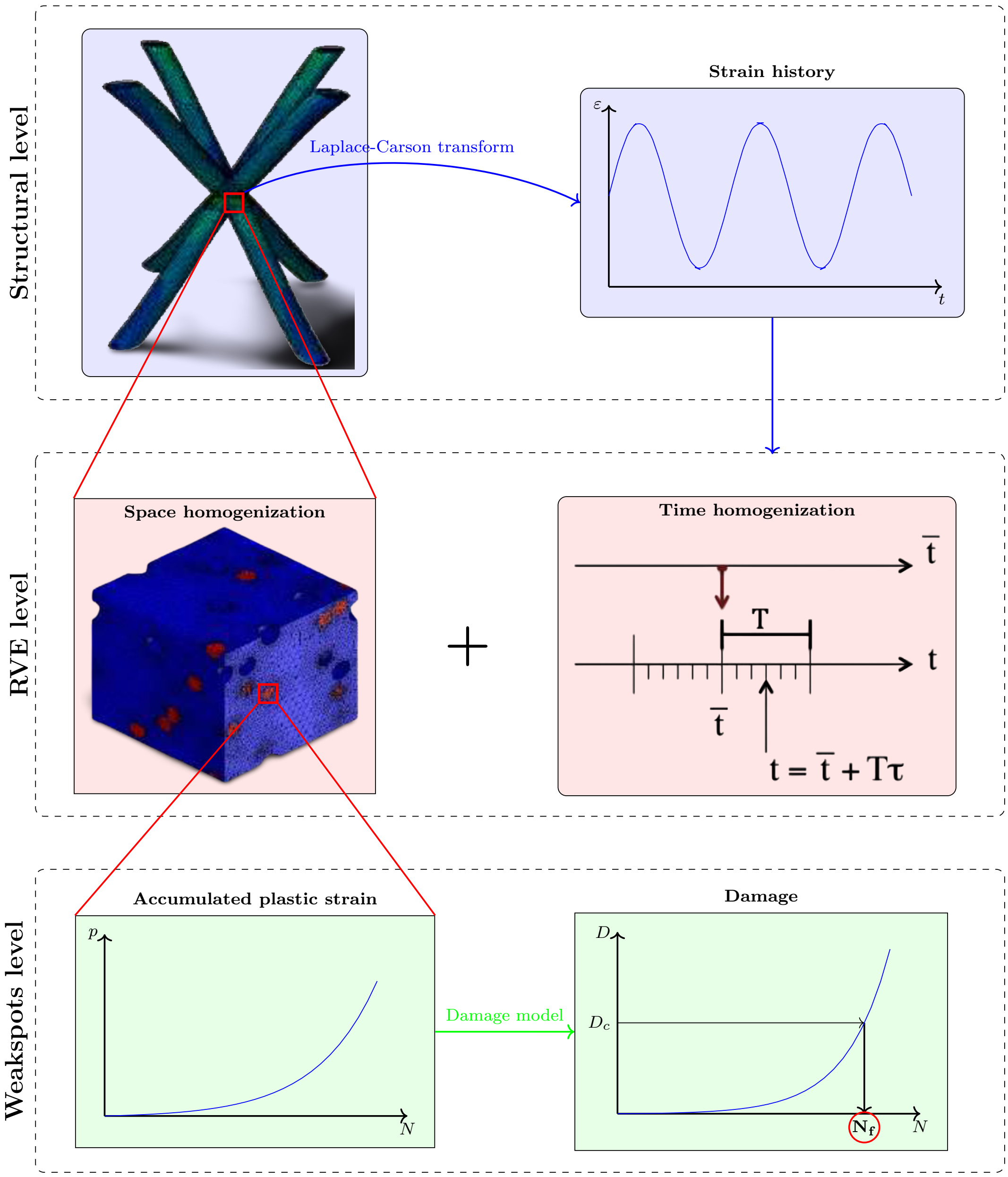

Figure 3.2: Overview of modeling strategy.

assumed to remain purely VE, throughout the cyclic loading. This assumption is valid only under large number of cycles and small strains, which is the case in the HCF regime. The main idea is to compute the solution only on these regions, sensitive to the plastification and generating finally cycle after cycle, the weakness of the entire structure.

It should be pointed out that the solution of the VE structural problem is not straightforward at all. The computational cost of VE full-field simulations for a high number of cycles (order of 10^6) is prohibitive. To overcome this issue, the LCT is employed to transform the VE problem into a purely elastic one in the L-C domain, as was described in Section 2.3.

After obtaining the macroscopic stress $\bar{\boldsymbol{\sigma}}^{VE}(\mathbf{x},t)$ and strain history $\bar{\boldsymbol{\varepsilon}}^{VE}(\mathbf{x},t)$ at the critical points of the VE structure, the next step is to employ the coupled time and space homogenization method as it will be presented in Section 3.2 to compute the solution inside the weakspots. However, The key question at hand to link these two steps is determining the macroscopic stress $\bar{\boldsymbol{\sigma}}^{VEVP}(\mathbf{x},t)$ and strain history $\bar{\boldsymbol{\varepsilon}}^{VEVP}(\mathbf{x},t)$ of the actual VEVP structure to be imposed on the RVE. In order to address this challenge, the following assumption is made:

Assumption 4. *The total strain histories for the VE and the VEVP problem are nearly the same, namely:*

$$\bar{\boldsymbol{\varepsilon}}^{VE}(\mathbf{x},t) = \bar{\boldsymbol{\varepsilon}}^{VEVP}(\mathbf{x},t) \tag{3.1}$$

This assumption might be a weak point of the overall procedure, but in the absence of a better solution, it is adopted in the present work. A more precise approach might be to assume an energy equivalence between the hypothetical VE and the actual VEVP solutions, inspired by the Neuber rule in metals. The problem is that this is only a scalar condition and further assumptions are required to fully determine the stress or strain tensor to be imposed on the RVE. However, such a study is outside the scope of the present work.

3.1.4 Two-level approach

The considered RVE consists of three phases (matrix, porosity & weakspots). However, the original Mori and Tanaka model is limited to a two-phase composite where all inclusions share the same shape, aspect ratio, material and orientation. For this reason, a two-level homogenization strategy is employed. In this approach, the matrix phase is first homogenized with the porosity. This is followed by embedding the weak spots in the previously homogenized porous matrix. The process is illustrated in Figure 3.3.

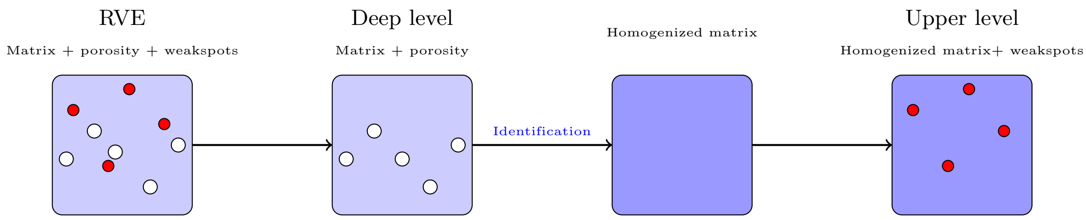

Figure 3.3: Two-level approach.

Lower Level

At the lower level, the actual matrix phase is homogenized with the cavities to create an intermediate homogenized material. The volume fractions at this level are given by:

$$v_p^{(L)} = \frac{v_p}{1 - v_{ws}}, \quad v_m^{(L)} = 1 - v_p^{(L)} \tag{3.2}$$

Upper Level

At the upper level, weak spots are embedded in the homogenized porous matrix obtained from the lower level. The volume fractions at this level are:

$$v_{ws}^{(U)} = v_{ws}, \quad v_m^{(U)} = 1 - v_{ws} \tag{3.3}$$

This hierarchical approach ensures that the total volume of each phase remains consistent throughout the homogenization process.

3.2 Coupling between time and space homogenization

3.2.1 Initial-boundary VEVP problem

A typical initial-boundary value problem is considered of a VEVP solid occupying spatial domain Ω and subjected to cyclic boundary displacements $\mathbf{u}_b$ and tractions $\mathbf{t}$ of the following forms:

$$\mathbf{t}(\mathbf{x}, t) = \mathbf{t}^*(\mathbf{x})\lambda(t) \quad \text{and} \quad \mathbf{u}_b(\mathbf{x}, t) = \mathbf{u}_b^*(\mathbf{x})\beta(t) \tag{3.4}$$

where $\lambda(t)$ and $\beta(t)$ represent the time variation of the cyclic loading. They are composed of a slow loading and a rapid harmonic oscillation with a very small load period T compared to the observation time t_f and they are of the following general form:

$$a(t) + b(t)\left(\sin\left(\frac{2\pi t}{T}\right) + c\right)$$

It is implicit that all variables are functions of position $\mathbf{x}$, so from now on and without loss of generality, the dependence of all variables on $\mathbf{x}$ is omitted for simplicity.

A VEVP solid body occupying a domain Ω with boundary $\Gamma = \Gamma_u \cup \Gamma_t$ is subjected to boundary displacements $\mathbf{u}_b$ on Γ_u and tractions $\mathbf{t}$ on Γ_t. The problem is expressed as follows:

Initial conditions:

$$\mathbf{u}(\mathbf{x}, t = 0) = \mathbf{u}^I(\mathbf{x}), \quad \text{in } \Omega \tag{3.5a}$$

$$\boldsymbol{\sigma}(\mathbf{x}, t = 0) = \boldsymbol{\sigma}^I(\mathbf{x}), \quad \text{in } \Omega \tag{3.5b}$$

Boundary conditions:

$$\mathbf{u} = \mathbf{u}_b, \quad \text{on } \Gamma_u \times [0, t_f] \tag{3.6a}$$

$$^t\boldsymbol{\sigma} \cdot \mathbf{n} = \mathbf{t}, \quad \text{on } \Gamma_t \times [0, t_f] \tag{3.6b}$$

Equilibrium equations:

$$\nabla \cdot \boldsymbol{\sigma} = \mathbf{0}, \quad \text{in } \Omega \times [0, t_f] \tag{3.7}$$

Kinematic compatibility:

$$\boldsymbol{\varepsilon}(\mathbf{u}) = \frac{1}{2}\left(\nabla \mathbf{u} + {}^t\nabla \mathbf{u}\right), \quad \text{in } \Omega \times [0, t_f] \tag{3.8}$$

Constitutive equations:

$$\boldsymbol{\varepsilon}(\boldsymbol{u}) = \boldsymbol{\varepsilon}^{ve} + \boldsymbol{\varepsilon}^{vp}, \quad \text{in } \Omega \times [0, t_f] \tag{3.9a}$$

$$\boldsymbol{\sigma}(t) = \mathbf{C}_\infty : \boldsymbol{\varepsilon}^{ve}(t) + \sum_{i=1}^{I} \mathbf{s}_i(t) + \sum_{j=1}^{J} \sigma_{H_j}(t)\mathbf{1}, \quad \text{in } \Omega \times [0, t_f] \tag{3.9b}$$

$$f(\boldsymbol{\sigma}, R(p)) = \sigma_{eq} - (\sigma_y + R(p)), \quad \text{in } \Omega \times [0, t_f] \tag{3.9c}$$

$$\dot{\boldsymbol{\varepsilon}}^{vp} = \dot{p}\mathbf{N}, \quad \text{in } \Omega \times [0, t_f] \tag{3.9d}$$

$$\dot{p} = C(\boldsymbol{\sigma}, p), \quad \text{in } \Omega \times [0, t_f] \tag{3.9e}$$

3.2.2 Asymptotic expansion of the initial-boundary VEVP problem

Each mechanical field variable $\phi(t_M, \tau)$ is expanded into an asymptotic series of powers of T, [15]:

$$\phi(t_M, \tau) = \sum_{i=0}^{\infty} T^i \phi_i(t_M, \tau), \tag{3.10}$$

which means that each variable $\phi(t_M, \tau)$ can be regarded as consisting of a leading term $\phi_0(t_M, \tau)$, plus a series of terms of rapidly decreasing amplitude. There are two basic assumptions at this point:

- The solution is regular enough
- The two time scales are completely decoupled ($\frac{T}{t_f} << 1$)

By replacing each variable by its asymptotic expansion into Equations (3.5)–(3.9) and gathering terms of equal order (i.e. equal powers of T), the initial-boundary value problem can be rewritten at the orders (-1) and (0) as follows:

- **Order -1 problem**

$$\frac{\partial}{\partial \tau} \boldsymbol{\varepsilon}_0^{vp}(t_M, \tau) = \mathbf{0}, \quad \text{in } \Omega \times [0, t_f] \times [0, 1] \tag{3.11a}$$

$$\frac{\partial}{\partial \tau} p_0(t_M, \tau) = 0, \quad \text{in } \Omega \times [0, t_f] \times [0, 1] \tag{3.11b}$$

- **Order 0 problem**

  Initial conditions:

$$\mathbf{u}_0(\mathbf{x}, t_M = 0, \tau = 0) = \mathbf{u}^I(\mathbf{x}), \quad \text{in } \Omega \tag{3.12a}$$

$$\boldsymbol{\sigma}_0(\mathbf{x}, t_M = 0, \tau = 0) = \boldsymbol{\sigma}^I(\mathbf{x}), \quad \text{in } \Omega \tag{3.12b}$$

  Boundary conditions:

$$\mathbf{u}_0 = \mathbf{u}_b, \quad \text{on } \Gamma_u \times [0, t_f] \times [0, 1] \tag{3.13a}$$

$${}^t\boldsymbol{\sigma}_0 \cdot \mathbf{n} = \mathbf{t}, \quad \text{on } \Gamma_t \times [0, t_f] \times [0, 1] \tag{3.13b}$$

  Equilibrium equations:

$$\nabla \cdot \boldsymbol{\sigma}_0 = \mathbf{0}, \quad \text{in } \Omega \times [0, t_f] \times [0, 1] \tag{3.14}$$

Kinematic compatibility:

$$\boldsymbol{\varepsilon}_0(\mathbf{u}_0) = \frac{1}{2}\left(\nabla\mathbf{u}_0 + {}^t\nabla\mathbf{u}_0\right), \quad \text{in } \Omega\times[0,t_f]\times[0,1] \tag{3.15}$$

Constitutive equations:

$$\boldsymbol{\varepsilon}_0(\boldsymbol{u}_0) = \boldsymbol{\varepsilon}_0^{ve} + \boldsymbol{\varepsilon}_0^{vp}, \quad \text{in } \Omega\times[0,t_f]\times[0,1] \tag{3.16a}$$

$$\begin{aligned}\boldsymbol{\sigma}_0(t_M,\tau) &= \mathbf{C}_\infty : \boldsymbol{\varepsilon}_0^{ve}(t_M,\tau)\\ &\quad + \sum_{i=1}^{I}\mathbf{s}_{i_0}(t_M,\tau) + \sum_{j=1}^{J}\sigma_{H_{j_0}}(t_M,\tau)\mathbf{1}, \quad \text{in } \Omega\times[0,t_f]\times[0,1]\end{aligned} \tag{3.16b}$$

$$f(\boldsymbol{\sigma}_0, R(p_0)) = \sigma_{eq_0} - (\sigma_y + R(p_0)), \quad \text{in } \Omega\times[0,t_f]\times[0,1] \tag{3.16c}$$

$$\frac{\partial}{\partial t_M}\boldsymbol{\varepsilon}_0^{vp}(t_M,\tau) + \frac{\partial}{\partial\tau}\boldsymbol{\varepsilon}_1^{vp}(t_M,\tau) = \dot{p}_0\mathbf{N}_0, \quad \text{in } \Omega\times[0,t_f]\times[0,1] \tag{3.16d}$$

$$\frac{\partial}{\partial t_M}p_0(t_M,\tau) + \frac{\partial}{\partial\tau}p_1(t_M,\tau) = C(\sigma_{eq_0}, p_0), \quad \text{in } \Omega\times[0,t_f]\times[0,1] \tag{3.16e}$$

Equations (3.11) show that at order $0, \boldsymbol{\varepsilon}_0^{vp}$ and p_0 are function of the slow time variable t_M only:

$$\boldsymbol{\varepsilon}_0^{vp}(t_M,\tau) = \boldsymbol{\varepsilon}_0^{vp}(t_M) \tag{3.17a}$$

$$p_0(t_M,\tau) = p_0(t_M) \tag{3.17b}$$

This is a fundamental result of time homogenization theory. Using Equations (3.11a) and (3.16a), we have:

$$\frac{\partial}{\partial\tau}\boldsymbol{\varepsilon}_0(t_M,\tau) = \frac{\partial}{\partial\tau}\boldsymbol{\varepsilon}_0^{ve}(t_M,\tau), \quad \text{in } \Omega\times[0,t_f]\times[0,1] \tag{3.18}$$

Equation (3.18) shows that at the zero-order the rapid evolution of total deformation is equal to that of its VE part.

3.2.3 Macro and micro chronological problems

In order to solve the zero-order problem of Equations (3.12)–(3.16), we follow the additive decomposition into mean and fluctuation parts defined in Equation 2.47. Taking the micro-time average as defined by Equation 2.46 of Equations (3.12)–(3.16) we obtain a decomposition of the original problem into macro- and micro-chronological problems:

- **Macro-chronological problem**

  Boundary conditions:

$$\mathbf{u}_{0_M} = \mathbf{u}_{b_M}, \quad \text{on } \Gamma_u \times [0, t_f] \tag{3.19a}$$
$${}^t\boldsymbol{\sigma}_{0_M} \cdot \mathbf{n} = \mathbf{t}_M, \quad \text{on } \Gamma_t \times [0, t_f] \tag{3.19b}$$

  Equilibrium equations:

$$\nabla \cdot \boldsymbol{\sigma}_{0_M} = \mathbf{0}, \quad \text{in } \Omega \times [0, t_f] \tag{3.20}$$

  Kinematic compatibility:

$$\boldsymbol{\varepsilon}_{0_M}(\mathbf{u}_{0_M}) = \frac{1}{2}\left(\nabla \mathbf{u}_{0_M} + {}^t\nabla \mathbf{u}_{0_M}\right), \quad \text{in } \Omega \times [0, t_f] \tag{3.21}$$

  Constitutive equations:

$$\boldsymbol{\varepsilon}_{0_M}(\boldsymbol{u}_{0_M}) = \boldsymbol{\varepsilon}^{ve}_{0_M}(t_M) + \boldsymbol{\varepsilon}^{vp}_0(t_M), \quad \text{in } \Omega \times [0, t_f] \tag{3.22a}$$
$$\boldsymbol{\sigma}_{0_M}(t_M) = \mathbf{C}_\infty : \boldsymbol{\varepsilon}^{ve}_{0_M}(t_M) + \sum_{i=1}^{I} \mathbf{s}_{i0_M}(t_M) + \sum_{j=1}^{J} \sigma_{H_{j0_M}}(t_M)\mathbf{1}, \quad \text{in } \Omega \times [0, t_f] \tag{3.22b}$$
$$f(\boldsymbol{\sigma}_{0_M} + \tilde{\boldsymbol{\sigma}}_0, R(p_0)) = \sigma_{eq}(\boldsymbol{\sigma}_{0_M} + \tilde{\boldsymbol{\sigma}}_0) - (\sigma_y + R(p_0)), \quad \text{in } \Omega \times [0, t_f] \tag{3.22c}$$
$$\frac{d}{dt_M}\boldsymbol{\varepsilon}^{vp}_{0_M} = \langle \dot{p}_0 \mathbf{N}(\boldsymbol{\sigma}_{0_M} + \tilde{\boldsymbol{\sigma}}_0)\rangle, \quad \text{in } \Omega \times [0, t_f] \tag{3.22d}$$
$$\frac{d}{dt_M} p_0 = \langle C(\sigma_{eq}(\boldsymbol{\sigma}_{0_M} + \tilde{\boldsymbol{\sigma}}_0), p_0)\rangle, \quad \text{in } \Omega \times [0, t_f] \tag{3.22e}$$

- **Micro-chronological problem**

  Boundary conditions:

$$\tilde{\mathbf{u}}_0 = \tilde{\mathbf{u}}_b, \quad \text{on } \Gamma_u \times [0, t_f] \times [0, 1] \tag{3.23a}$$
$${}^t\tilde{\boldsymbol{\sigma}}_0 \cdot \mathbf{n} = \tilde{\mathbf{t}}, \quad \text{on } \Gamma_t \times [0, t_f] \times [0, 1] \tag{3.23b}$$

  Equilibrium equations:

$$\nabla \cdot \tilde{\boldsymbol{\sigma}}_0 = \mathbf{0}, \quad \text{in } \Omega \times [0, t_f] \times [0, 1] \tag{3.24}$$

Kinematic compatibility:

$$\tilde{\boldsymbol{\varepsilon}}_0(\tilde{\mathbf{u}}_0) = \frac{1}{2}\left(\nabla\tilde{\mathbf{u}}_0 + {}^t\nabla\tilde{\mathbf{u}}_0\right), \quad \text{in } \Omega \times [0, t_f] \times [0, 1] \tag{3.25}$$

Constitutive equations:

$$\tilde{\boldsymbol{\varepsilon}}_0(\tilde{\boldsymbol{u}}_0) = \tilde{\boldsymbol{\varepsilon}}_0^{ve}(t_M, \tau), \quad \text{in } \Omega \times [0, t_f] \times [0, 1] \tag{3.26a}$$

$$\tilde{\boldsymbol{\sigma}}_0(t_M, \tau) = \mathbf{C}_\infty : \tilde{\boldsymbol{\varepsilon}}_0^{ve}(t_M, \tau) + \sum_{i=1}^{I} \tilde{\mathbf{s}}_{i0}(t_M, \tau) + \sum_{j=1}^{J} \tilde{\sigma}_{H_{j0}}(t_M, \tau)\mathbf{1}, \quad \text{in } \Omega \times [0, t_f] \times [0, 1] \tag{3.26b}$$

Equations (3.23)–(3.26) correspond to the resolution of a VE problem only, since the VP flow rule does not depend on the fast time variable explicitly.

The structure of the two problems shows that in practice, for each t_M, one solves the micro-time problem (3.23)–(3.26). Next the macro-chronological problem (3.19)–(3.22) completed by the following initial conditions can be solved:

$$\mathbf{u}_{0_M}(\mathbf{x}, t_M = 0) + \tilde{\mathbf{u}}_0(\mathbf{x}, t_M = 0, \tau = 0) = \mathbf{u}^I(\mathbf{x}), \quad \text{in } \Omega \tag{3.27a}$$

$$\boldsymbol{\sigma}_{0_M}(\mathbf{x}, t_M = 0) + \tilde{\boldsymbol{\sigma}}_0(\mathbf{x}, t_M = 0, \tau = 0) = \boldsymbol{\sigma}^I(\mathbf{x}), \quad \text{in } \Omega \tag{3.27b}$$

3.2.4 Time discretization

A numerical time discretization algorithm is employed as proposed in [3]. The algorithm is a combination of techniques used separately for VE-VP materials [10] and the method of time homogenization.

Time discrete form of the stress update

First, the constitutive Equations (2.5)–(2.7) are written in a time discrete form. Using a mid-point time integration rule, the discrete form of 2.6 over a time interval $[t_n, t_{n+1}]$ is:

$$\mathbf{s}_i\left(t_{n+1}\right) = \exp\left(-\frac{\Delta t}{g_i}\right)\mathbf{s}_i\left(t_n\right) + 2\widehat{G}_i(\Delta t)\Delta\boldsymbol{\xi}^{ve} \tag{3.28a}$$

$$\sigma_{H_j}\left(t_{n+1}\right) = \exp\left(-\frac{\Delta t}{k_j}\right)\sigma_{H_j}\left(t_n\right) + 3\widehat{K}_j(\Delta t)\Delta\varepsilon_H^{ve} \tag{3.28b}$$

The increments are designated by, $\Delta t = t_{n+1} - t_n$, $\Delta\boldsymbol{\xi}^{ve} = \boldsymbol{\xi}^{ve}\left(t_{n+1}\right) - \boldsymbol{\xi}^{ve}\left(t_n\right)$ and $\Delta\varepsilon_H^{ve} = \varepsilon_H^{ve}\left(t_{n+1}\right) - \varepsilon_H^{ve}\left(t_n\right)$. The expressions of $\widehat{G}_i(\Delta t)$ and $\widehat{K}_j(\Delta t)$ are given by:

$$\widehat{G}_i(\Delta t) = G_i \exp\left(-\frac{\Delta t}{2g_i}\right) \tag{3.29a}$$

$$\widehat{K}_j(\Delta t) = K_j \exp\left(-\frac{\Delta t}{2k_j}\right) \tag{3.29b}$$

For convenience, the following incremental relaxation moduli are defined:

$$\widehat{G}(\Delta t) = G_\infty + \sum_{i=1}^{I} \widehat{G}_i(\Delta t);\ \widehat{K}(\Delta t) = K_\infty + \sum_{j=1}^{J} \widehat{K}_j(\Delta t);\ \widehat{\mathbb{C}} = 2\widehat{G}\mathbb{I}^{dev} + 3\widehat{K}\mathbb{I}^{vol} \tag{3.30}$$

The time discrete form of Equation 2.7 is then:

$$\begin{aligned}\boldsymbol{\sigma}\left(t_{n+1}\right) =& \mathbb{C}_\infty : \boldsymbol{\varepsilon}^{ve}\left(t_n\right) + \widehat{\mathbb{C}}(\Delta t) : \Delta\boldsymbol{\varepsilon}^{ve} + \\ & \sum_{i=1}^{I} \exp\left(-\frac{\Delta t}{g_i}\right) \mathbf{s}_i\left(t_n\right) + \sum_{j=1}^{J} \exp\left(-\frac{\Delta t}{k_j}\right) \sigma_{H_j}\left(t_n\right) \mathbf{1}\end{aligned} \tag{3.31}$$

Variables $\mathbf{s}_i, \sigma_{Hj}, \boldsymbol{\xi}^{ve}$ and ε_H^{ve} depend on both time scales t_M and τ. Their asymptotic expansions are injected in Equation 3.31. Calculating all the terms at the same micro-time τ we have, $\Delta t = \Delta t_M$. Consequently, the zeroth order stress update is now given by the following discrete form of Equation 3.16b.

$$\begin{aligned}&\boldsymbol{\sigma}_0\left(t_{M_n+1}, \tau\right) = \mathbb{C}_\infty : \boldsymbol{\varepsilon}_0^{ve}\left(t_{Mn}, \tau\right) + \widehat{\mathbb{C}}(\Delta t_M) : \Delta\boldsymbol{\varepsilon}_0^{ve} + \\ &\sum_{i=1}^{I} \exp\left(-\frac{\Delta t_M}{g_i}\right) \mathbf{s}_{i_0}\left(t_{Mn}, \tau\right) + \sum_{j=1}^{J} \exp\left(-\frac{\Delta t_M}{k_j}\right) \sigma_{H_{j0}}\left(t_{Mn}, \tau\right) \mathbf{1},\end{aligned} \tag{3.32}$$

with the zero-order terms of these viscous stresses over $[t_{Mn}, t_{M_n+1}]$:

$$\mathbf{s}_{i_0}\left(t_{Mn+1}, \tau\right) = \exp\left(\frac{-\Delta t_M}{g_i}\right) \mathbf{s}_{i_0}\left(t_{Mn}, \tau\right) + 2\widehat{G}_i(\Delta t_M)\Delta\boldsymbol{\xi}_0^{ve} \tag{3.33a}$$

$$\sigma_{H_{j0}}\left(t_{M_n+1}, \tau\right) = \exp\left(\frac{-\Delta t_M}{k_j}\right) \sigma_{H_{j0}}\left(t_{Mn}, \tau\right) + 3\widehat{K}_j(\Delta t_M)\Delta\varepsilon_{H_0}^{ve} \tag{3.33b}$$

Time discrete form of the VP strain update

The macro zeroth-order VP strain and accumulated plastic strain increments are computed according to the backward Euler scheme applied to Equations (3.22d) and (3.22e):

$$\Delta\boldsymbol{\varepsilon}_0^{vp} \approx \left.\frac{d\boldsymbol{\varepsilon}_0^{vp}}{dt_M}\right|_{\left(t_{Mn+1}\right)} \Delta t_M = \langle \mathbf{N}(\boldsymbol{\sigma}_0)|_{\left(t_{Mn+1}\right)}\rangle \Delta p_0 \tag{3.34a}$$

$$\Delta p_0 \approx \left.\frac{dp_0}{dt_M}\right|_{\left(t_{Mn+1}\right)} \Delta t_M = \langle C(\boldsymbol{\sigma}_0, p_0)|_{\left(t_{Mn+1}\right)}\rangle \Delta t_M \tag{3.34b}$$

Following the decomposition into mean and fluctuation terms defined in Equation (2.47), and taking the time average as defined by Equation (2.46) of Equations (3.32)–(3.34), the macro and micro-chronological decomposition of discretized problem are obtained and presented in the following subsections.

Time discrete form of the micro-chronological problem

The micro-chronological problem of Equations (3.23)–(3.26) is purely VE. For each macro-time interval $[t_{Mn}, t_{M_n+1}]$, the fluctuation part of the stress is updated explicitly (no iterations required). The time discrete form of Equations of Equations (3.23)–(3.26) is written as follows:

Boundary conditions:

$$\tilde{\mathbf{u}}_0 = \tilde{\mathbf{u}}_b, \quad \text{on } \Gamma_u \times [0, t_f] \times [0, 1] \tag{3.35a}$$

$$^t\tilde{\boldsymbol{\sigma}}_0 \cdot \mathbf{n} = \tilde{\mathbf{t}}, \quad \text{on } \Gamma_t \times [0, t_f] \times [0, 1] \tag{3.35b}$$

Equilibrium equations:

$$\nabla \cdot \tilde{\boldsymbol{\sigma}}_0 = \mathbf{0}, \quad \text{in } \Omega \times [0, t_f] \times [0, 1] \tag{3.36}$$

Kinematic compatibility:

$$\tilde{\boldsymbol{\varepsilon}}_0(\tilde{\mathbf{u}}_0) = \frac{1}{2}\left(\nabla\tilde{\mathbf{u}}_0 + {}^t\nabla\tilde{\mathbf{u}}_0\right), \quad \text{in } \Omega \times [0, t_f] \times [0, 1] \tag{3.37}$$

Constitutive equations:

$$\Delta\tilde{\boldsymbol{\varepsilon}}_0(\Delta\tilde{\boldsymbol{u}}_0) = \Delta\tilde{\boldsymbol{\varepsilon}}_0^{ve}, \text{ in } \Omega \times [0, t_f] \times [0, 1] \tag{3.38a}$$

$$\tilde{\boldsymbol{\sigma}}_0\left(t_{M_n+1}, \tau\right) = \mathbb{C}_\infty : \tilde{\boldsymbol{\varepsilon}}_0^{ve}\left(t_{Mn}, \tau\right) + \widehat{\mathbb{C}}(\Delta t_M) : \Delta\tilde{\boldsymbol{\varepsilon}}_0^{ve} + \sum_{i=1}^{I} \exp\left(-\frac{\Delta t_M}{g_i}\right) \tilde{\mathbf{s}}_{i_0}\left(t_{Mn}, \tau\right) + \sum_{j=1}^{J} \exp\left(-\frac{\Delta t_M}{k_j}\right) \tilde{\sigma}_{H_{j0}}\left(t_{Mn}, \tau\right) \mathbf{1}, \quad \text{in } \Omega \times [0, t_f] \times [0, 1] \tag{3.38b}$$

Equation (3.38b) constitutes the time discrete form of Equation (3.26b). The viscous stresses are updated according to:

$$\tilde{\mathbf{s}}_{i_0}\left(t_{Mn+1}, \tau\right) = \exp\left(\frac{-\Delta t_M}{g_i}\right)\tilde{\mathbf{s}}_{i_0}\left(t_{Mn}, \tau\right) + 2\widehat{G}_i(\Delta t_M)\Delta\tilde{\boldsymbol{\xi}}_0^{ve} \tag{3.39a}$$

$$\tilde{\sigma}_{H_{j0}}\left(t_{M_n+1}, \tau\right) = \exp\left(\frac{-\Delta t_M}{k_j}\right)\tilde{\sigma}_{H_{j0}}\left(t_{Mn}, \tau\right) + 3\widehat{K}_j(\Delta t_M)\Delta\tilde{\varepsilon}_{H_0}^{ve} \tag{3.39b}$$

Remark 1. *The micro-chronological problem* (3.35)–(3.38) *can be solved with the classical formulation of the incremental secant MFH method as was presented in [2].*

Time discrete form of the macro-chronological problem

The macro-chronological problem of Equations (3.19)–(3.22) has to be solved at each macro-time t_{Mn}. The discrete form of Equations (3.19)–(3.22) read:

Boundary conditions:

$$\mathbf{u}_{0_M} = \mathbf{u}_{b_M}, \qquad \text{on } \Gamma_u \times [0, t_f] \tag{3.40a}$$

$$^{t}\boldsymbol{\sigma}_{0_M} \cdot \mathbf{n} = \mathbf{t}_M, \qquad \text{on } \Gamma_t \times [0, t_f] \tag{3.40b}$$

Equilibrium equations:

$$\nabla \cdot \boldsymbol{\sigma}_{0_M} = \mathbf{0}, \qquad \text{in } \Omega \times [0, t_f] \tag{3.41}$$

Kinematic compatibility:

$$\boldsymbol{\varepsilon}_{0_M}(\mathbf{u}_{0_M}) = \frac{1}{2}\left(\nabla\mathbf{u}_{0_M} + {}^{t}\nabla\mathbf{u}_{0_M}\right), \qquad \text{in } \Omega \times [0, t_f] \tag{3.42}$$

Constitutive equations:

$$\Delta\boldsymbol{\varepsilon}_{0_M}(\Delta\boldsymbol{u}_{0_M}) = \Delta\boldsymbol{\varepsilon}_{0_M}^{ve} + \Delta\boldsymbol{\varepsilon}_0^{vp}, \qquad \text{in } \Omega \times [0, t_f] \tag{3.43a}$$

$$\begin{aligned}\boldsymbol{\sigma}_{0_M}\left(t_{M_n+1}\right) = {} & \mathbb{C}_\infty : \boldsymbol{\varepsilon}_{0_M}^{ve}\left(t_{M_n}\right) + \widehat{\mathbb{C}}(\Delta t_M) : \Delta\boldsymbol{\varepsilon}_{0_M}^{ve} \\ & + \sum_{i=1}^{I}\exp\left(-\frac{\Delta t_M}{g_i}\right)\mathbf{s}_{i_{0_M}}\left(t_{M_n}\right), \\ & + \sum_{j=1}^{J}\exp\left(-\frac{\Delta t_M}{k_j}\right)\sigma_{H_{j0_M}}\left(t_{M_n}\right)\mathbf{1},\end{aligned} \qquad \text{in } \Omega \times [0, t_f] \tag{3.43b}$$

$$\begin{aligned}f(\boldsymbol{\sigma}_{0_M} + \tilde{\boldsymbol{\sigma}}_0, R(p_0)) = {} & \sigma_{eq}(\boldsymbol{\sigma}_{0_M} + \tilde{\boldsymbol{\sigma}}_0)\big|_{\left(t_{Mn+1}, \tau\right)} \\ & - \left(\sigma_y + R(p_0\left(t_{Mn+1}\right))\right),\end{aligned} \qquad \text{in } \Omega \times [0, t_f] \times [0, 1] \tag{3.43c}$$

$$\Delta\boldsymbol{\varepsilon}_0^{vp} = \langle \mathbf{N}(\boldsymbol{\sigma}_{0_M} + \tilde{\boldsymbol{\sigma}}_0)\big|_{\left(t_{Mn+1}\right)}\rangle\Delta p_0, \qquad \text{in } \Omega \times [0, t_f] \tag{3.43d}$$

$$\Delta p_0 = \langle C(\boldsymbol{\sigma}_{0_M} + \tilde{\boldsymbol{\sigma}}_0, p_0)\big|_{\left(t_{Mn+1}\right)}\rangle\Delta t_M, \qquad \text{in } \Omega \times [0, t_f] \tag{3.43e}$$

Remark 2. *The macro-chronological problem* (3.40)–(3.43) *is nonlinear and solved iteratively at each macro time step.*

Remark 3. *The reason why the macro-chronological problem* (3.40)–(3.43) *can not be solved with the classical incremental secant formulation as presented in [2] is that the yield function* (3.43c) *is defined with the total stress, rather than just the time-averaged part. This is the key point that couples the micro- and macro-chronological problems and necessitates the development of a coupled time and space homogenization method.*

Summary of time homogenization algorithm

In this Section, a short illustration of the time homogenization algorithm is given. Consider a macro time interval $[t_{Mn}, t_{Mn+1}]$. All the global and per phase zeroth-order micro- and macro-chronological history variables $\langle\tilde{\phi}_0\rangle_\Omega$, $\langle\tilde{\phi}_0\rangle_{\Omega_i}$, $\langle\phi_{0M}\rangle_\Omega$, $\langle\phi_{0M}\rangle_{\Omega_i}$ at (t_{Mn}, τ) are known. Moreover, the imposed global micro- and macro-chronological strain increments $\langle\Delta\tilde{\boldsymbol{\varepsilon}}\rangle_\Omega$, $\langle\Delta\boldsymbol{\varepsilon}_M\rangle_\Omega$ are given. The problem is to obtain the solution at (t_{Mn+1}, τ). The algorithm is illustrated in Figure 3.4. The space homogenization procedure to solve the micro- and macro-chronological problems is explained in the following Section.

3.2.5 Incremental secant formulation

The objective of this Section is to develop a MFH method to solve the time-discrete form of the macro-chronological problem (3.40)–(3.43). It should be pointed out that the micro-chronological problem can be solved without any modification of the original algorithm (Remark 1). For this reason only the details for the solution of the macro-chronological problem will be presented here.

Without loss of generality the subscript 0, which indicates the zeroth-order term of the asymptotic expansion, is dropped and from now on all the field variables in the equations constitute their zeroth-order counterparts unless otherwise stated.

Application to J_2 visoplasticity

In this paragraph, each constitutive phase follows the constitutive law presented in Section 2.1. The first step of the incremental secant method is the unloading of the composite from the current state at time (t_{Mn}, τ) to a virtual state at time $(t_{M_n^{res}}, \tau)$. The unloading is VE driven by the unloading time increment $\Delta t_M^{unload} = t_{M_n^{res}} - t_{Mn}$. Consider the unloading strain increment $\Delta\boldsymbol{\varepsilon}^{unload} = \boldsymbol{\varepsilon}(t_{Mn}, \tau) - \boldsymbol{\varepsilon}(t_{M_n^{res}}, \tau)$. The predicted stress resulting from the VE predictor is given in Equation (3.32). Following the decomposition of the residual stress

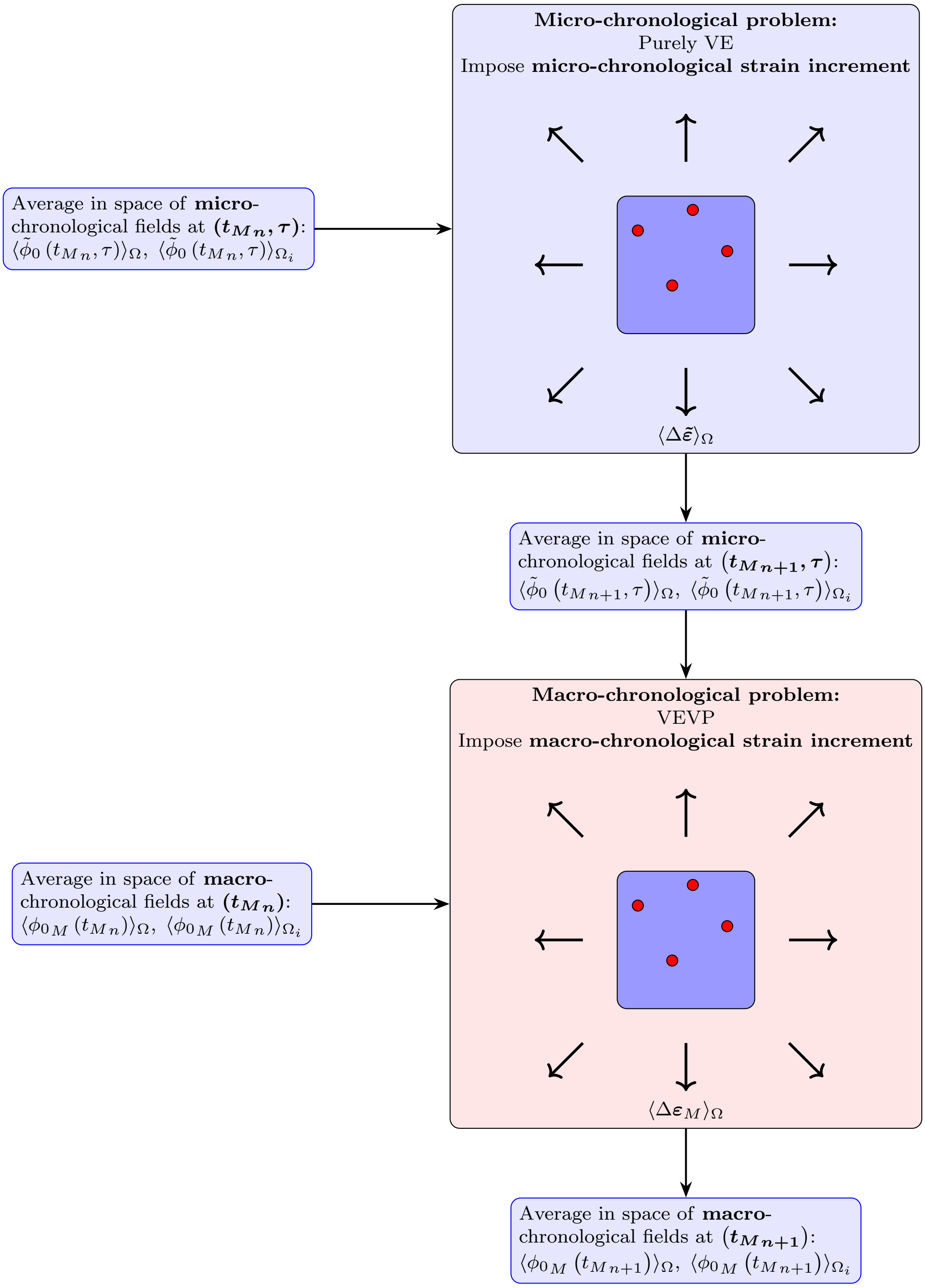

Figure 3.4: Summary of the coupled space and time-homogenization method for VE-VP composites. Time stepping is performed with respect to macro time t_M.

into mean and fluctuation parts, according to Equation (2.47), and using the VE predictor Equation (3.32) for each one of them:

$$
\begin{aligned}
\boldsymbol{\sigma}\left(t_{M_n}^{res}, \tau\right) &= \overbrace{\tilde{\boldsymbol{\sigma}}\left(t_{M_n}^{res}, \tau\right)}^{\text{Coupling term}} + \boldsymbol{\sigma}_M\left(t_{M_n}^{res}\right) \\
&= \tilde{\boldsymbol{\sigma}}\left(t_{M_n}^{res}, \tau\right) + \mathbb{C}_\infty : \boldsymbol{\varepsilon}_M^{ve}\left(t_{Mn}\right) + \widehat{\mathbb{C}}\left(\Delta t_M^{unload}\right) : \Delta \boldsymbol{\varepsilon}_M{}^{unload} \\
&\quad + \sum_{i=1}^{I} \exp\left(-\frac{\Delta t_M^{unload}}{g_i}\right) \mathbf{s}_{iM}\left(t_{Mn}\right) \\
&\quad + \sum_{j=1}^{J} \exp\left(-\frac{\Delta t}{k_j}\right) \sigma_{H_j M}\left(t_{Mn}\right) \mathbf{1} \quad \forall \omega_i
\end{aligned}
\tag{3.44}
$$

Knowing that $\Delta \boldsymbol{\varepsilon}^r = \Delta \boldsymbol{\varepsilon} + \Delta \boldsymbol{\varepsilon}^{unload}$ (see Fig. 2.3), combination of Equations (3.32) and (3.44) leads to :

$$
\begin{aligned}
\boldsymbol{\sigma}^{pred}\left(t_{Mn+1}, \tau\right) &= \overbrace{\tilde{\boldsymbol{\sigma}}\left(t_{Mn+1}, \tau\right)}^{\text{Coupling term}} + \boldsymbol{\sigma}_M\left(t_{Mn+1}\right) \\
&= \tilde{\boldsymbol{\sigma}}\left(t_{Mn+1}, \tau\right) + \boldsymbol{\sigma}_M\left(t_{M_n}^{res}\right) + \widehat{\mathbb{C}}\left(\Delta t_M\right) : \Delta \boldsymbol{\varepsilon}_M^r \\
&\quad + \left[\widehat{\mathbb{C}}\left(\Delta t_M^{unload}\right) - \widehat{\mathbb{C}}(\Delta t_M)\right] : \Delta \boldsymbol{\varepsilon}_M^{unload} \\
&\quad + \sum_{i=1}^{I} \left[\exp\left(\frac{-\Delta t_M}{g_i}\right) - \exp\left(\frac{-\Delta t_M^{unload}}{g_i}\right)\right] \boldsymbol{s}_{iM}\left(t_{Mn}\right) \\
&\quad + \sum_{j=1}^{J} \left[\exp\left(\frac{-\Delta t_M}{k_j}\right) - \exp\left(\frac{-\Delta t_M^{unload}}{k_j}\right)\right] \sigma_{Hj_M}\left(t_{Mn}\right) \mathbf{1} \quad \forall \omega_i
\end{aligned}
\tag{3.45}
$$

The VE predictor requires the assessment of the yield function $f^{pred}\left(t_{Mn+1}, \tau\right)$ (Equation (2.8)) based on either the first or the second moment estimates of the equivalent predicted stress, as given in [2].

If the trial state satisfies the yield criterion:

$$
f^{pred}\left(t_{Mn+1}, \tau\right) = \sigma_{eq}^{pred}\left(t_{Mn+1}, \tau\right) - \left[\sigma_y + R\left(p\left(t_{Mn}\right)\right)\right] \leq 0 \tag{3.46}
$$

Then, the VE predictor is indeed the solution at time $\left(t_{Mn+1}, \tau\right)$ and there was no evolution of VP strain:

$$
\boldsymbol{\sigma}\left(t_{Mn+1}, \tau\right) = \boldsymbol{\sigma}^{pred}\left(t_{Mn+1}, \tau\right) \tag{3.47}
$$

$$
\boldsymbol{\varepsilon}^{vp}\left(t_{Mn+1}\right) = \boldsymbol{\varepsilon}^{vp}\left(t_{Mn}\right), \quad p\left(t_{Mn+1}\right) = p\left(t_{Mn}\right) \tag{3.48}
$$

However, if $f^{pred}(t_{Mn+1}, \tau) > 0$, VP strains have evolved and VP corrector is needed in order to update the solution. Consequently, the system of non-linear equations needs to be solved.

$$\begin{cases} \boldsymbol{\sigma}(t_{Mn+1}, \tau) = \boldsymbol{\sigma}^{pred}(t_{Mn+1}, \tau) - \widehat{\mathbb{C}}(\Delta t_M) : \Delta\boldsymbol{\varepsilon}^{vp} \\ \Delta\boldsymbol{\varepsilon}^{vp} = \langle \mathbf{N}(t_{Mn+1}, \tau)\rangle \Delta p & \forall \omega_i \\ \Delta p = \langle g_v(\boldsymbol{\sigma}_{eq}(t_{Mn+1}, \tau), p(t_{Mn}))\rangle \Delta t_M \end{cases} \tag{3.49}$$

Substituting the second equation to the first of the system (3.49) and taking into account that $\mathbf{N}$ is deviatoric and $\widehat{\mathbb{C}}(\Delta t_M)$ is isotropic, the system of equations simplifies to:

$$\begin{cases} \boldsymbol{\sigma}(t_{Mn+1}, \tau) = \boldsymbol{\sigma}^{pred}(t_{Mn+1}, \tau) - 2\widehat{G}(\Delta t_M)\langle \mathbf{N}(t_{Mn+1}, \tau)\rangle \Delta p \\ \Delta p = \langle g_v(\boldsymbol{\sigma}_{eq}(t_{Mn+1}, \tau), p(t_{Mn}))\rangle \Delta t_M & \forall \omega_i \end{cases} \tag{3.50}$$

$\mathbf{N}$ is the plastic flow direction. In the incremental-secant method, it is approximated as follows:

$$\begin{aligned} \mathbf{N}(t_{Mn+1}, \tau) &= \frac{3}{2} \frac{\mathbb{I}^{dev} : (\boldsymbol{\sigma}(t_{Mn+1}, \tau) - \boldsymbol{\sigma}(t_{M_n^{res}}, \tau))}{(\boldsymbol{\sigma}(t_{Mn+1}, \tau) - \boldsymbol{\sigma}(t_{M_n^{res}}, \tau))^{eq}} \\ &= \frac{3}{2} \frac{\mathbb{I}^{dev} : \Delta\boldsymbol{\sigma}^{r}(t_{Mn+1}, \tau)}{(\Delta\boldsymbol{\sigma}^{r}(t_{Mn+1}, \tau))^{eq}} \end{aligned} \tag{3.51}$$

It satisfies $\mathbf{N}(t_{Mn+1}, \tau) : \mathbf{N}(t_{Mn+1}, \tau) = \frac{3}{2}$. Equation (3.51) shows that the direction of viscoplastic flow is collinear to the deviatoric part of $\Delta\boldsymbol{\sigma}^{r}(t_{Mn+1}, \tau)$. In a similar way, one defines $\mathbf{N}^{pred}(t_{Mn+1}, \tau)$ as:

$$\begin{aligned} \mathbf{N}^{pred}(t_{Mn+1}, \tau) &= \frac{3}{2} \frac{\mathbb{I}^{dev} : \left(\boldsymbol{\sigma}^{pred}(t_{Mn+1}, \tau) - \boldsymbol{\sigma}(t_{M_n^{res}}, \tau)\right)}{(\boldsymbol{\sigma}^{pred}(t_{Mn+1}, \tau) - \boldsymbol{\sigma}(t_{M_n^{res}}, \tau))^{eq}} \\ &= \frac{3}{2} \frac{\mathbb{I}^{dev} : \Delta\boldsymbol{\sigma}^{rpred}(t_{Mn+1}, \tau)}{(\Delta\boldsymbol{\sigma}^{rpred}(t_{Mn+1}, \tau))^{eq}} \end{aligned} \tag{3.52}$$

One-point time integration

The System (3.50) must be solved for the unknowns: $\boldsymbol{\sigma}(t_{Mn+1}, \tau)$ and $p(t_{Mn+1})$. The main difficulty arises from the numerical evaluation of the averages $\langle \bullet \rangle$. Although a multi-point integration scheme would approximate quite accurately the micro-time averages of the plastic flow direction and the VP function in the System (3.50), it adds a lot of complexity both from the formulation and implementation point of view. For this reason, a simple one-point time integration is implemented here.

Assumption 5. *It is assumed that the averages of the plastic flow direction and the VP function can be approximated by their value at the midpoint of the integration interval, which corresponds to* $\tau = \frac{1}{2}$. *In other words:*

$$\langle \phi(t_M, \tau) \rangle = \int_0^1 \phi(t_M, \tau)\, d\tau \approx \phi\left(t_M, \frac{1}{2}\right) \tag{3.53}$$

From now on, all the functions are evaluated in the middle of the time interval at $\tau = \frac{1}{2}$, unless otherwise stated. Given Assumption 5, the System (3.50) becomes:

$$\begin{cases} \boldsymbol{\sigma}\left(t_{Mn+1}, \frac{1}{2}\right) = \boldsymbol{\sigma}^{pred}\left(t_{Mn+1}, \frac{1}{2}\right) - 2\widehat{G}(\Delta t_M)\mathbf{N}\left(t_{Mn+1}, \frac{1}{2}\right)\Delta p \\ \Delta p = g_v\left(\boldsymbol{\sigma}_{eq}\left(t_{Mn+1}, \frac{1}{2}\right), p\left(t_{Mn}\right)\right)\Delta t_M \qquad \forall \omega_i \end{cases} \tag{3.54}$$

Using Equations (3.51)–(3.52) and the first equation of the System (3.54), the following result is obtained:

$$\mathbf{N}\left(t_{Mn+1}, \frac{1}{2}\right) = \mathbf{N}^{pred}\left(t_{Mn+1}, \frac{1}{2}\right) \tag{3.55}$$

Equations (3.52) and (3.55) are substituted in the System (3.54), leading to :

$$\begin{cases} F_\sigma = \overbrace{\left(\boldsymbol{\sigma}\left(t_{Mn+1}, \frac{1}{2}\right) - \boldsymbol{\sigma}\left(t_{Mn}^{res}, \frac{1}{2}\right)\right)^{eq}}^{(\Delta\boldsymbol{\sigma}^r)^{eq}} + 3\widehat{G}(\Delta t_M)\Delta p \\ \qquad - \underbrace{\left(\boldsymbol{\sigma}^{pred}\left(t_{Mn+1}, \frac{1}{2}\right) - \boldsymbol{\sigma}\left(t_{Mn}^{res}, \frac{1}{2}\right)\right)^{eq}}_{\left(\Delta\boldsymbol{\sigma}^{r\,pred}\right)^{eq}} = 0 \\ F_p = \Delta p - g_v\left(\boldsymbol{\sigma}_{eq}\left(t_{Mn+1}, \frac{1}{2}\right), p\left(t_{Mn}\right)\right)\Delta t_M = 0 \end{cases} \tag{3.56}$$

The system (3.56) is solved for $(\Delta\boldsymbol{\sigma}^r)^{eq}$ and (t_{Mn+1}), iteratively, using Newton-Raphson method until satisfying the convergence criteria on $F_\sigma = 0$ and $F_p = 0$.

It is important to notice here that, the solution $(\Delta\boldsymbol{\sigma}^r)^{eq}$ retrieved after convergence represents either the first or the second order evaluation of the equivalent stress increment depending on the moment's order used to estimate the equivalent predicted stress $\left(\boldsymbol{\sigma}^{pred}\left(t_{Mn+1}, \frac{1}{2}\right)\right)^{eq}$. It follows that the new material state at $\left(t_{Mn+1}, \frac{1}{2}\right)$ is constructed by pursuing the steps hereafter:

$$
\begin{aligned}
&\text{a.} \quad (\Delta\boldsymbol{\sigma}^r)^{dev} = \frac{2}{3}(\Delta\boldsymbol{\sigma}^r)^{eq}\,\mathbf{N}^{pred}\left(t_{M\,n+1}, \frac{1}{2}\right)\\
&\text{b.} \quad \Delta\boldsymbol{\sigma}^r = (\Delta\boldsymbol{\sigma}^r)^{dev} + \frac{1}{3}\,\mathrm{tr}\left(\Delta\boldsymbol{\sigma}^{rpred}\right)\mathbf{1}\\
&\text{c.} \quad \boldsymbol{\sigma}\left(t_{M\,n+1}, \frac{1}{2}\right) = \boldsymbol{\sigma}\left(t_{M\,n}^{res}, \frac{1}{2}\right) + \Delta\boldsymbol{\sigma}^r\\
&\text{d.} \quad \boldsymbol{\varepsilon}^{vp}(t_{M\,n+1}) = \boldsymbol{\varepsilon}^{vp}(t_{M\,n}) + \Delta p\mathbf{N}^{pred}\left(t_{M\,n+1}, \frac{1}{2}\right)
\end{aligned}
$$

Incremental-secant operator and eigenstress tensor

The incremental-secant approach in VE-VP implies that the constitutive equations of each phase of the composite are linearized such that:

$$
\Delta\boldsymbol{\sigma}^r = \mathbb{C}_i^S\left(t_{M\,n+1}, \frac{1}{2}\right) : \Delta\boldsymbol{\varepsilon}^r + \boldsymbol{\beta}_i^S\left(t_{M\,n+1}, \frac{1}{2}\right) \quad \forall\omega_i \tag{3.57}
$$

It can be seen from Equation (3.57) that this approach leads to a linearized format similar to thermoelasticity, which was presented in Section 2.4.1. Expressions of the secant operator $\mathbb{C}^S$ and the eigenstress tensor $\boldsymbol{\beta}^S$ of each averaged material phase material are determined from Equations (3.45) and (3.54), as follows:

$$
\mathbb{C}_i^S\left(t_{M\,n+1}, \frac{1}{2}\right) = \widehat{\mathbb{C}}(\Delta t_M) - 3\widehat{G}(\Delta t_M)\Delta p\frac{\mathbb{I}^{dev} : \widehat{\mathbb{C}}(\Delta t_M)}{(\Delta\boldsymbol{\sigma}^{rpred})^{eq}} \tag{3.58}
$$

$$
\begin{aligned}
\boldsymbol{\beta}_i^S\left(t_{M\,n+1}, \frac{1}{2}\right) = {}& \left[\mathbb{I} - \frac{3\widehat{G}(\Delta t_M)\Delta p}{(\Delta\boldsymbol{\sigma}^{rpred})^{eq}}\mathbb{I}^{dev}\right] : \Bigg[\overbrace{\tilde{\boldsymbol{\sigma}}\left(t_{M\,n+1}, \frac{1}{2}\right) - \tilde{\boldsymbol{\sigma}}\left(t_{M\,n}^{res}, \frac{1}{2}\right)}^{\text{Coupling term}}\\
&+ \left[\widehat{\mathbb{C}}\left(\Delta t_M^{unload}\right) - \widehat{\mathbb{C}}(\Delta t_M)\right] : \Delta\boldsymbol{\varepsilon}_M^{unload}\\
&+ \sum_{i=1}^{I}\left(\exp\left(\frac{-\Delta t_M}{g_i}\right) - \exp\left(\frac{-\Delta t_M^{unload}}{g_i}\right)\right)\boldsymbol{s}_{iM}(t_{M\,n})\\
&+ \sum_{j=1}^{J}\left(\exp\left(\frac{-\Delta t_M}{k_j}\right) - \exp\left(\frac{-\Delta t_M^{unload}}{k_j}\right)\right)\sigma_{Hj\,M}(t_{M\,n})\,\mathbf{1}\Bigg]
\end{aligned} \tag{3.59}
$$

Remark 4. *In the absence of visco-plastic flow $\Delta p = 0$, the expression of $\mathbb{C}_i^S\left(t_{M\,n+1}, \frac{1}{2}\right)$ is simplified to $\mathbb{C}_i^S\left(t_{M\,n+1}, \frac{1}{2}\right) = \widehat{\mathbb{C}}(\Delta t_M)$ and $\boldsymbol{\beta}_i^S\left(t_{M\,n+1}, \frac{1}{2}\right)$ is equal to zero, so homogenization is done as in linear elasticity and not in thermo-elastic manner.*

Remark 5. $\mathbb{C}_i^S\left(t_{M\,n+1}, \frac{1}{2}\right)$ *is naturally isotropic.*

Remark 5 is the main idea behind the incremental secant MFH method and the main reason of its accuracy in comparison with other linearization methods, which result in anisotropic stiffness tensors in phases that require isotropization in order to use the Eshelby solution. Since the secant operator is isotropi, it can be rewritten as a decomposition of deviatoric and dilatational parts:

$$\mathbb{C}_i^S\left(t_{Mn+1},\frac{1}{2}\right) = 3K_i^S\left(t_{Mn+1},\frac{1}{2}\right)\mathbb{I}^{vol} + 2G_i^S\left(t_{Mn+1},\frac{1}{2}\right)\mathbb{I}^{dev} \quad \forall\omega_i, \tag{3.60}$$

with

$$\begin{cases} K_i^S\left(t_{Mn+1},\frac{1}{2}\right) = \widehat{K}(\Delta t_M) \\ G_i^S\left(t_{Mn+1},\frac{1}{2}\right) = \widehat{G}(\Delta t_M) - \frac{3\left(\widehat{G}(\Delta t_M)\right)^2\Delta p}{\left(\Delta\boldsymbol{\sigma}^{rpred}\right)^{eq}} \end{cases} \tag{3.61}$$

Equation (3.59) reveals that the eigenstress tensor $\boldsymbol{\beta}_i^S\left(t_{Mn+1},\frac{1}{2}\right)$ depends on the unloading scheme controlled by Δt_M^{unload}. In this work, the unloading increment Δt_M^{unload} will be kept equal to the loading increment Δt_M, unless otherwise stated. However, this is not obligatory and different values could be explored.

MFH algorithm for macro-chronological problem

In this Section, the different steps of MFH based on the incremental-secant linearization procedure for the solution of the macro-chronological problem are summarized. For this, assuming that the problem is solved until the beginning of time interval $[t_{Mn}, t_{Mn+1}]$, which means that all state variables at time t_{Mn} are supposed to be determined, the composite RVE is subjected to macro strain $\Delta\overline{\boldsymbol{\varepsilon}_M}$. Moreover, the micro-chronological problem is assumed to be already solved and all the state variables to be known, at time $\left(t_{Mn+1},\frac{1}{2}\right)$. The main steps are highlighted in Figure 3.5.

Residual states

The residual box $\mathcal{R}^{res}$ used in the first step of the MFH process can be summarized as follows. Notice that the expressions of $\boldsymbol{\sigma}\left(t_n\right)$ and $\boldsymbol{\sigma}\left(t_n^{res}\right)$ result from Equation (3.31) for $\Delta t = 0$ and $\Delta t = \Delta t^{unload}$, respectively:

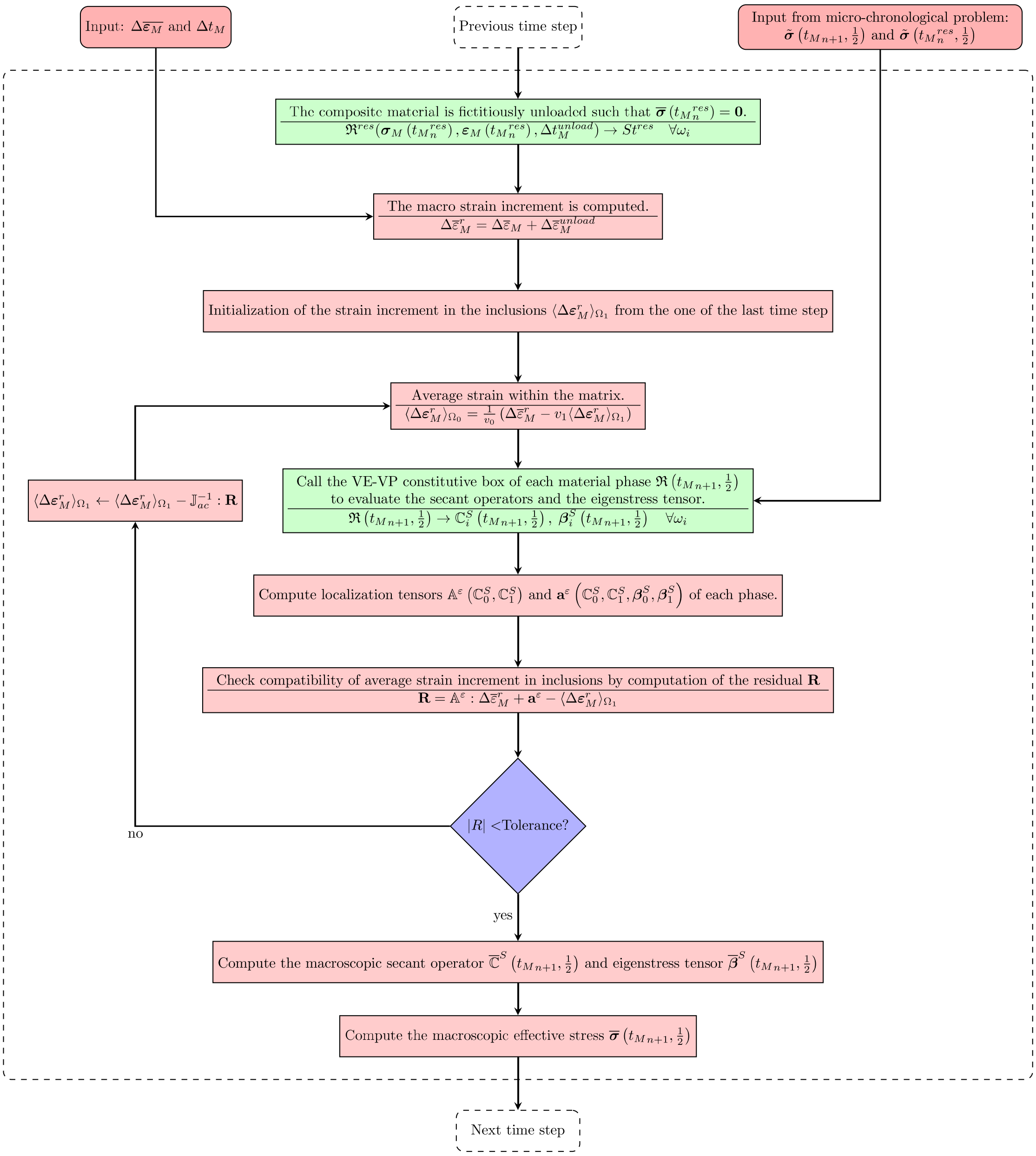

Figure 3.5: Algorithm of the homogenization model for the macro-chronological problem.

$$
\begin{aligned}
\boldsymbol{\sigma}\left(t_n\right) =&\mathbb{C}_{\infty} : \boldsymbol{\varepsilon}^{ve}\left(tn\right) + \sum_{i=1}^{I} \mathbf{s}_i\left(t_n\right) + \sum_{j=1}^{J} \sigma_{H_j}\left(t_n\right)\mathbf{1} && \text{(3.62a)}\\
\boldsymbol{\sigma}\left(t_n^{res}\right) =&\mathbb{C}_{\infty} : \boldsymbol{\varepsilon}^{ve}\left(tn\right) - \widehat{\mathbb{C}}(\Delta t^{unload}) : \Delta\boldsymbol{\varepsilon}^{unload} + \\
&\sum_{i=1}^{I} \exp\left(-\frac{\Delta t^{unload}}{g_i}\right)\mathbf{s}_i\left(t_n\right) + \sum_{j=1}^{J} \exp\left(-\frac{\Delta t^{unload}}{k_j}\right)\sigma_{H_j}\left(t_n\right)\mathbf{1} && \text{(3.62b)}
\end{aligned}
$$

Combination of the latter two equations leads to:

$$
\begin{aligned}
&\underbrace{\boldsymbol{\sigma}\left(t_n\right) - \boldsymbol{\sigma}\left(t_n^{unload}\right)}_{\Delta\boldsymbol{\sigma}^{unload}} = \underbrace{\widehat{\mathbb{C}}(\Delta t^{unload}) : \Delta\boldsymbol{\varepsilon}^{unload}}_{\mathbb{C}_{res}^{S}} + \\
&\underbrace{\sum_{i=1}^{I}\left(1 - \exp\left(\frac{-\Delta t^{unload}}{g_i}\right)\right)\mathbf{s}_i\left(t_n\right) + \sum_{j=1}^{J}\left(1 - \exp\left(\frac{-\Delta t^{unload}}{k_j}\right)\right)\boldsymbol{\sigma}_{Hj}\left(t_n\right)\mathbf{1}}_{\boldsymbol{\beta}_{res}^{S}}
\end{aligned}
\tag{3.63}
$$

In Equation (3.63), the bulk and shear moduli of $\mathbb{C}_{res}^{S}$ are given by Equation (3.30) after replacing Δt with Δt^{unload}. This implies that the relaxation weights G_i and K_j and times g_i and k_j are used for any values of Δt^{unload}. This is a consequence of the linear VE model adopted in subsection 2.1 which is based on the Prony series (Equation (2.4)).

Since the unloading step is fictitious, the macroscopic residual stress $\overline{\boldsymbol{\sigma}}\left(t_n^{res}\right)$ should satisfy:

$$
\overline{\boldsymbol{\sigma}}\left(t_n^{res}\right) = \left\langle \boldsymbol{\sigma}\left(t_n^{res}\right)\right\rangle_{\Omega} = 0 \tag{3.64}
$$

The problem stated in Equation (3.63) is equivalent to thermo-elastic MFH described in subsection (2.4.1) with the following substitutions:

$$
\boldsymbol{\sigma} \to \Delta\boldsymbol{\sigma}^{unload},\ \boldsymbol{\varepsilon} \to \Delta\boldsymbol{\varepsilon}^{unload},\ \mathbb{C} \to \mathbb{C}_{res}^{S},\ \boldsymbol{\beta} \to \boldsymbol{\beta}_{res}^{S} \tag{3.65}
$$

Therefore, the residual states are determined following the steps presented in Figure 3.6.

It should be noted that in the residual box algorithm of Figure 3.6, it is not specified if each variable ϕ refers to the time-average part ϕ_M or the fluctuation part $\tilde{\phi}$. This is because the same algorithm is used in both the micro- and macro-chronological problems.

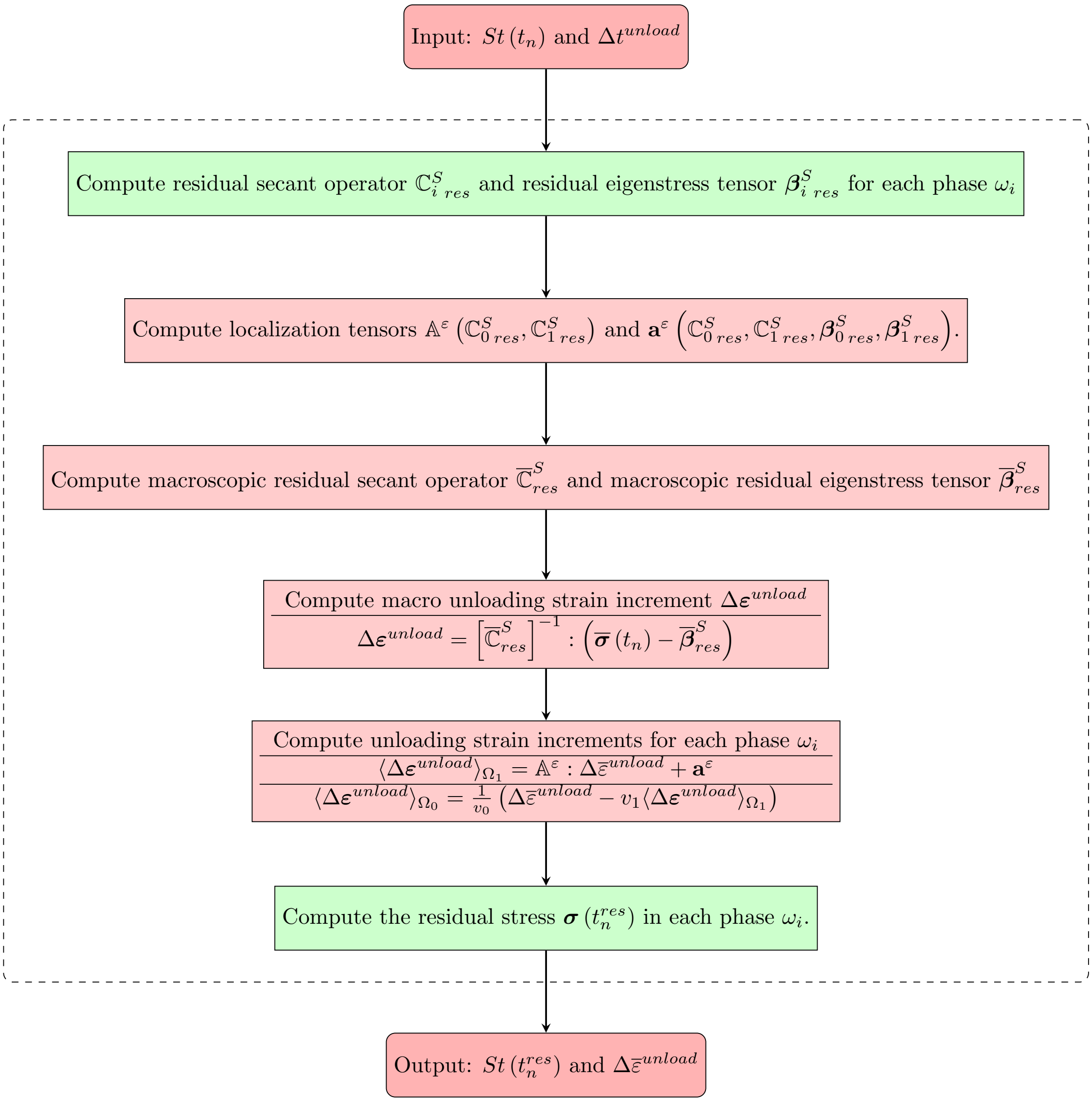

Figure 3.6: Residual box algorithm.

3.3 Post processing: Damage calculation and fatigue prediction

The damage calculation tool adopted here was first tested and implemented by a previous Master student. The main assumption of the damage calculation is:

Assumption 6. *The VEVP constitutive model and the damage model are assumed completely decoupled, so that there is no degradation of the stiffness of the material with damage evolution.*

Although assumption 6 is a major simplification, it is necessary to have a reasonable computational cost of the damage calculation. The main problem here is that in Equation (2.17), the material constants are unknown. They are calculated by optimization as it will be explained in Section 3.3.2, where the goal is to minimize the error between fatigue predictions and experimental observations. If a completely coupled VEVPD model was implemented in the time & space homogenization model, the cost for the evaluation of the objective function for one set of material constants would be prohibitive for optimization. The goal here is to develop a post-processing tool for damage calculation with minimal computational cost without sacrificing accuracy.

3.3.1 Numerical algorithm for damage calculation

Similarly with the VP strain and the accumulated plastic strain updates ((3.34)), the time-discrete form of Equation (2.17) is obtained using a backward Euler scheme:

$$\Delta D \approx \left.\frac{dD}{dt}\right|_{(t_{n+1})} \Delta t = \left(\frac{Y\left(t_{n+1}\right)}{S}\right)^{s} \Delta p, \tag{3.66}$$

where the strain energy release rate is given by Equation 2.16. After the calculation of the damage history $D(t)$, the estimation of the fatigue life corresponds to the moment when damage reaches the critical value D_c. In other words:

$$D(N) = D_c \rightarrow N_f^{sim} \tag{3.67}$$

3.3.2 Optimization problem

In order to get accurate fatigue predictions, it is necessary to compute the material constants of the damage law, which in general can be expressed as:

$$\boldsymbol{\theta} \in (S, s, D_c, p_D) \tag{3.68}$$

Let's consider fatigue experimental results. The tests are performed at different loading amplitudes $X_i,\ i = 1, ..., n$ with a cyclic history until failure and the number of cycles to failure $N_f^{exp}(X_i)$ is recorded. The macroscopic loading parameter X used could correspond to a macroscopic stress component Σ or global displacement U or any other measure of loading amplitude. In the present work, the simulations correspond to displacement-controlled experiments.
The definition of an error function is crucial for the optimization process. There are many ways to define the error between experimental and simulation results. Some of them could be:

- Mean absolute error :

$$\frac{1}{n}\sum_{i=1}^{n}\left|N_f^{sim}(X_i) - N_f^{exp}(X_i)\right|$$

- Mean absolute percentage error :

$$\frac{1}{n}\sum_{i=1}^{n}\left|\frac{N_f^{sim}(X_i) - N_f^{exp}(X_i)}{N_f^{exp}(X_i)}\right|$$

- Root mean square error :

$$\sqrt{\frac{1}{n}\sum_{i=1}^{n}\left(N_f^{sim}(X_i) - N_f^{exp}(X_i)\right)^2}$$

In the present work, a root mean square error (RMSE) metric is favored, because it penalizes larger errors more severely. However, it is modified by calculating the RMSE of the logarithms to accommodate the significant differences in magnitude among the data points. It should be noted that such an error function is implicitly used when an empirical formula is fitted in the S-N curves (e.g. Basquin's law). The formulation is as follows:

Optimization problem

$$\begin{aligned} &\min_{\boldsymbol{\theta}} \sqrt{\frac{1}{n}\sum_{i=1}^{n}\left[\log\left(N_f^{sim}(X_i, \boldsymbol{\theta})\right) - \log\left(N_f^{exp}(X_i)\right)\right]^2} \qquad (3.69)\\ &\text{s.t.:}\quad \theta_{min} \leq \theta_j \leq \theta_{max}, \quad \forall j = 1, 2, \ldots, m \end{aligned}$$

Chapter 4

Results

The coupled time & space homogenization method was implemented using one-point integration for the micro-chronological averages in the C programming language. In Section **??**, the code is validated for the case of a homogeneous material. The results are compared with the ones presented from Haouala [3] and also with the ones obtained with a fine time step. In Section 4.2, the code is validated for the case of a heterogeneous RVE. Section 4.3 presents the fatigue predictions and the comparison with the experimental results.
All the simulations are performed using a PC with an Intel Core i7 processor (4.6GHz) and 16 GB of RAM.

4.1 Method validation for homogeneous material

In this Section, the homogeneous case is studied. Since the code was developed for the case of two-phase composites, the homogeneous case is retrieved by assigning the same material properties to both phases. The response in the phases and the macroscopic response are exactly the same, so in this section there is no need for distinction and the notation is simplified $\bar{\phi} = \langle\phi\rangle_0 = \langle\phi\rangle_1 = \phi$.
All the parameters of this example are exactly the same as in [3] and the goal is to compare the results. The applied strain history is linear at first and then sinusoidal with period $T = 0.1$ s and maximum value $\varepsilon_{\max} = 0.05$:

$$\begin{cases} \varepsilon_{11}(t) = \varepsilon_{\max} \frac{1+R}{2} \frac{t}{T}, & \text{if } t \leq T \\ \varepsilon_{11}(t) = \varepsilon_{\max} \left(\frac{1-R}{2} \sin\left(2\pi \frac{t}{T}\right) + \frac{1+R}{2} \right), & \text{otherwise} \end{cases} \tag{4.1}$$

The identified VE-VP material parameters are listed in Table 1. The loading ratio R, corresponds to the ratio between the minimum and the maximum of the loading: $R = \varepsilon_{\min}/\varepsilon_{\max}$. Two cases are studied with $R = 0.1$ and $R = -1$ and $3 \cdot 10^4$ cycles are applied.

Viscoelastic parameters			
Initial shear modulus	$G_0 = 1074$MPa		
Initial bulk modulus	$K_0 = 3222$MPa		
G_i[MPa]	g_i[s]	K_j[MPa]	k_j[s]
158	0.021	472	0.007
80	0.378	242	0.126
37	0.648	111	0.216
Viscoplastic parameters			
Hardening function	$k_1 = 79$MPa	$n = 0.15$	
Viscoplastic function	$\kappa = 0.131\text{s}^{-1}$	$m = 4.02$	
Yield stress	$\sigma_y = 40$MPa		

Table 4.1: Constitutive model parameters for polyamide (PA) at 40°C, adopted from [3].

Comparisons between the reference non-homogenized (full-time) calculation and the two-scale computation are given in Figures (4.1)–(4.4). The reference numerical solution is obtained using a very fine time step $\Delta t = T/20$, whereas the time-homogenized computation starts with a full calculation until time $t = 7/4T$ and then continues with $\Delta t_M = T$.

4.1.1 Loading ratio R = 0.1

Figure 4.1 displays the stress-strain hysteresis loops for selected cycles. The solid lines indicate the reference results, while the black dots represent the time homogenization predictions. Notably, due to the repeated application of relatively small strain, the stress level significantly decreases from a maximum of 118 MPa in the first cycle to approximately 93 MPa in the subsequent cycles. Additionally, the stress-strain hysteresis loop quickly shrinks as the number of cycles increases.

Figure 4.2 presents the comparison of time-homogenized results from the present work with ones obtained in [3] as well as the reference solution for the first and last 20 cycles. The agreement between the time-homogenized results of the present study with the ones from [3] is remarkable and validates the code developed for the case of a homogeneous material. Observing Figures 4.2a (first 20 cycles) and 4.2b (last 20 cycles), it should be noted that the accuracy of the method improves and the time-homogenized solution practically converges to the reference for high number of cycles. There are two reasons for the discrepancy in the first cycles. First, only the zero-order in the asymptotic expansion is considered. Second, for the first twenty cycles the load period is not sufficiently small compared to the observation time (in this case to 20 T), which is a major assumption of the asymptotic expansion.

Figure 4.3 shows the comparison for the accumulated plastic strain p. It is noted that p tends to saturate and after a large number of cycles it becomes constant, which means that the material reaches an asymptotic state called "elastic shakedown", where there is no more induced plasticity after an initial transient phase. This conclusion is reinforced by the tendency of the hysteresis loop to become constant in Figure 4.1, as well as the stabilization of the stress amplitude in Figure 4.2b. The main reason behind this is that the material is assumed to obey an isotropic hardening law and as p increases the stress threshold increases too according to Equation (2.8) and eventually becomes large enough, so that no more plasticity is induced.

Observing Figure 4.3, the accuracy of the time-homogenized solution for the accumulated plastic strain is significantly worse than for the stress. This leads to the following remark:

Remark 6. *The error on the the stress is amplified on the accumulated plastic strain p.*

There are two main reasons behind this:

1. The rate of p depends on the stress through the plastic potential. Therefore, even a small discrepancy in the stress prediction is amplified and becomes much worse in the case of p.

2. Most importantly, p is an accumulated quantity over the entire time history. As a result, although the large error in the first cycles of the simulation did not affect the stress convergence at a high number of cycles, this is not the case for p, which accumulates errors throughout the entire history.

4.1.2 Loading ratio R = -1

In this section, the case of a purely sinusoidal loading with zero mean is studied. This case corresponds to loading ratio $R = -1$ and is particularly interesting, since it is the most challenging one for the time homogenization method. The reason behind this is that the material is in yield over a larger amount of the period due to the full reversal of the loading, which means that one-point integration might not be sufficient. That was the reason that a multi-point integration rule was developed in [3] to improve the predictions in this case. However, one-point integration was

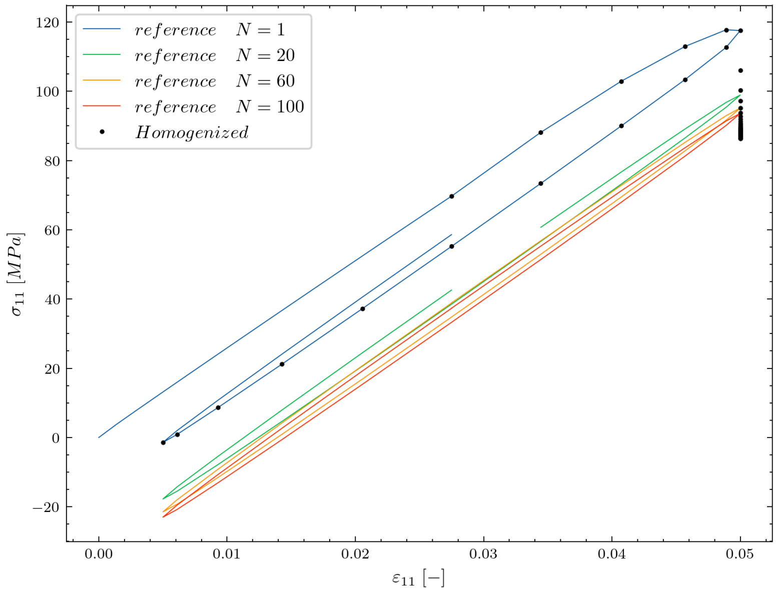

Figure 4.1: Hysteresis loops: First hundred cycles, loading period: T = 0.1 s, loading ratio: R = 0.1.

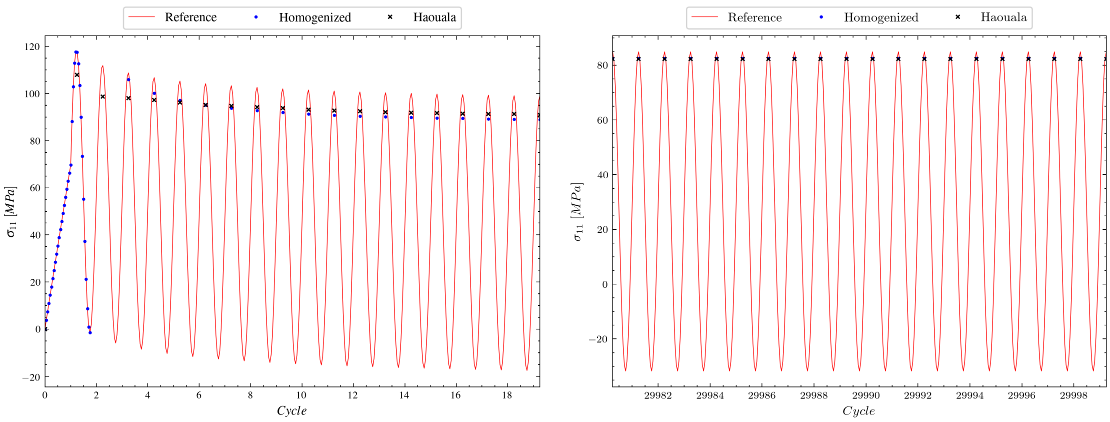

(a) The first 20 cycles

(b) The last 20 cycles

Figure 4.2: Evolution of the stress: homogenized solution in comparison with reference results with fine time step and results from [3], loading period: T = 0.1 s, loading ratio: R = 0.1.

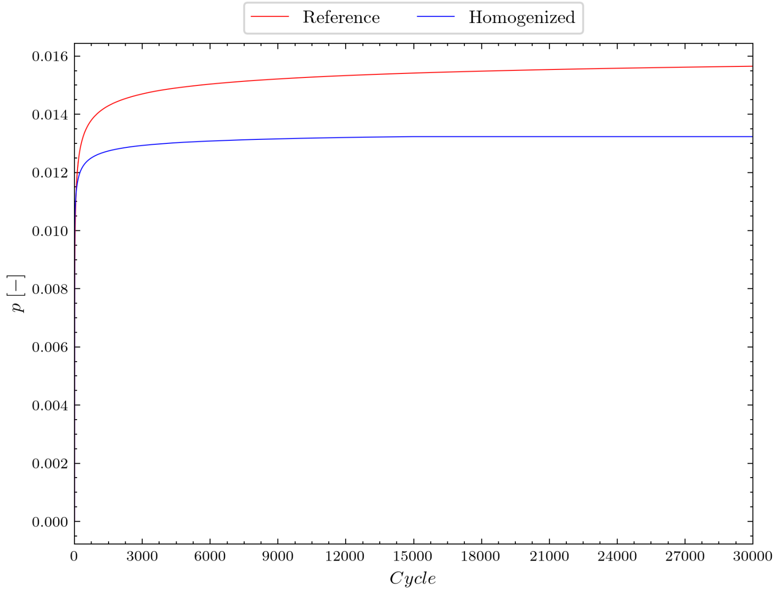

Figure 4.3: Evolution of the accumulated plastic strain: homogenized solution in comparison with reference results, loading period: T = 0.1 s, loading ratio: R = 0.1.

used throughout the present work and an alternative way was found to improve the accuracy as it will be explained in Section **??**.

Figure 4.4 shows the comparison between the time-homogenized results obtained in the present work and the ones obtained in [3] with one-point and multi-point integration, as well as with reference ones, for the stress in the last 20 cycles. Again, the agreement between the present results and the ones from [3] with one-point integration is excellent. However, in this case where $R = -1$ the stress prediction is much worse than the one in the case of $R = 0.1$. On the other hand, the multi-point integration method developed in [3] gives much better predictions.

It should be mentioned that the prediction of accumulated plastic strain is very bad, as expected from Remark 6. Since, the evolution of damage, which is the ultimate goal of this work, depends on the evolution of p, it is absolutely necessary to improve the prediction of the accumulated plastic strain and this will be the goal of Section **??**.

4.1.3 Study of the macro time increment

The accuracy of the results obtained for homogeneous material are not satisfactory enough, so the objective of this section is to improve the predictions, before moving to the case of a heterogeneous RVE. There are two main sources of error:

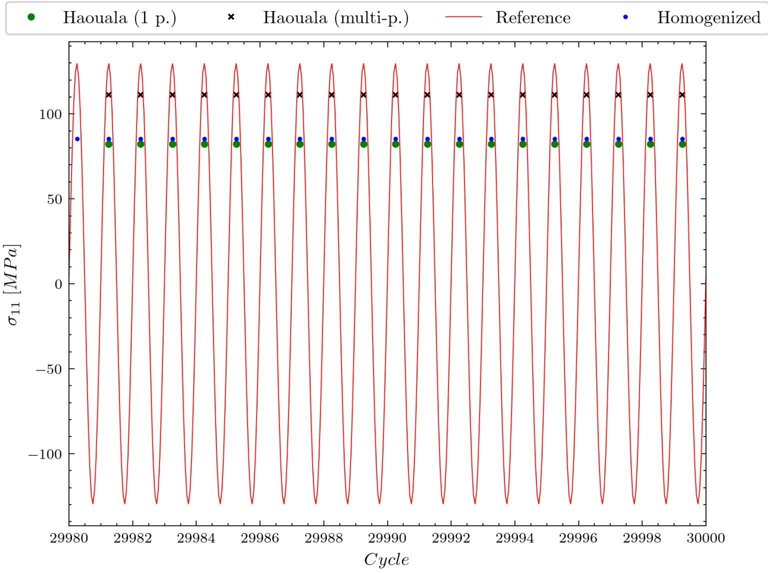

Figure 4.4: Evolution of the stress: homogenized solution in comparison with reference results with fine time step and results from [3] with one-point and multi-point integration, loading period: T = 0.1 s, loading ratio: R = -1.

Remark 7. *The micro-time averaging of the viscoplastic strain rate equations with one-point per cycle is not a good approximation as illustrated in Figure 4.5. The figure shows that the viscoplastic function is zero for a large part of the cycle, when the stress is below the yield, so a calculation exactly at the middle of the cycle, where g_v is maximum, vastly overestimates the exact value.*

Remark 8.

The update of the viscous stresses is not accurate enough if a multiple of the period is used, since then the strain increment vanishes and there is only the relaxation term in Equations (3.39)*. That is the reason behind the drop in the stress prediction in the beginning of the simulation in Figure 4.2a.*

To address the first issue, a multi-point integration was proposed in [8], but was implemented only in the uniaxial case. Although a multi-point integration would significantly improve the results, it is avoided here due to the complexity both in the formulation and implementation and a different solution is proposed.

The solution proposed is to use a macro-time step Δt_M, such that the calculation is done at a different point of each successive cycle, and this way the average increase of accumulated plastic strain p approaches the exact value. The inspiration for this idea is that sampling a periodic function at various points approximately replicates the effect of micro-time averaging. Although this idea is not entirely rigorous, it

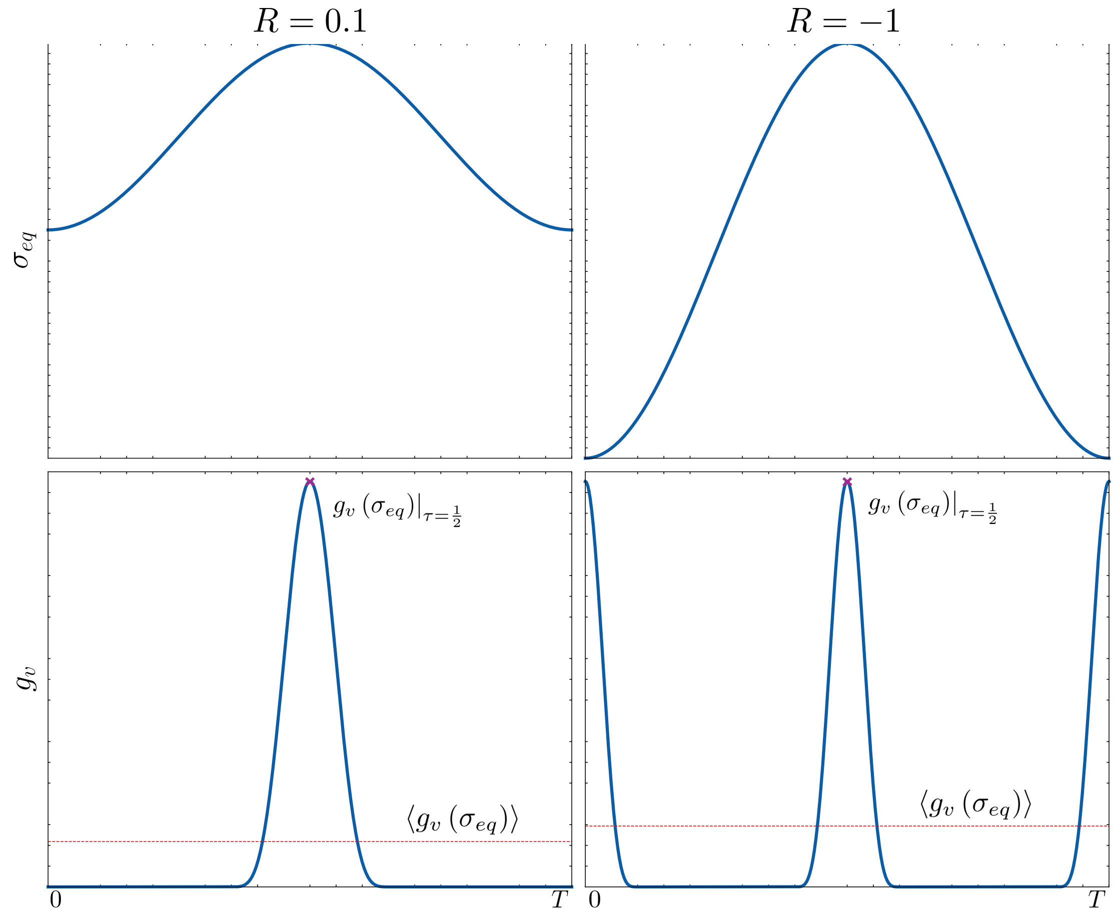

Figure 4.5: Illustration of micro-time averaging error with one-point integration for the cases of R=0.1 and R=-1.

will massively improve the results, providing that Δt_M is chosen appropriately. The right choice of the macro-time increment is exactly the objective of this section.

A non-integer Δt_M forces the calculation at different points from cycle to cycle. This procedure will also address the second issue mentioned previously. The reason for this is that the strain increment is not zero from cycle to cycle and as a result the update of the viscous stresses is more accurate.

Figure 4.6 shows the evolution of the stress and strain for different values of macro-time increment Δt_M for the case with loading ratio $R = -1$. Figures 4.6a and 4.6b present the applied strain history for the first and last 20 cycles, respectively. Figures 4.6c and 4.6d show the corresponding stress for the first and last 20 cycles. The points where the time-homogenized solution is calculated are plotted with different markers, whereas the reference solution, which was obtained with a fine time-step $\Delta T = T/20$ is plotted with a solid line.

On the other hand, the evolution of the accumulated plastic strain is given in Figure 4.7. A careful observation of Figures 4.6 and 4.7 leads to the following conclusions:

- The points of the cycle where the time-homogenized solution is calculated significantly affect the accuracy of the results.

- An integer macro-time increment, such as $\Delta t_M = T$ leads to a fast relaxation in the beginning of the loading history (Remark 8), which results in a bad prediction of the stress history and even worse prediction of the accumulated plastic strain p.

- The best prediction of the stress is obtained with $\Delta t_M = 1.5T$, where the calculation is done at the extreme points of the cyclic loading (maximum and minimum). This was expected as the viscoplastic function g_v is maximum at these points, which leads to an overestimation of each micro-time average (Remark 7, as can be seen in Figure 4.7.

- The optimal prediction of the accumulated plastic strain is obtained with $\Delta t_M = 1.625T$. The reason behind this is that instead of this is that the calculation of the time-homogenized solution is done at different points inside the cycle (and not only the extreme points), mimicking multi-point micro-time averaging (Remark 7). On the other hand, it is quite close to the optimal value of $\Delta t_M = 1.5T$ for the accurate update of viscous stresses.

Finally, the predictions of the stress peaks for the first and last 100 cycles for different values of the macro-time increment are presented in Figure 4.8. The figure clearly illustrates the advantages of using a non-integer Δt_M. Moreover, the

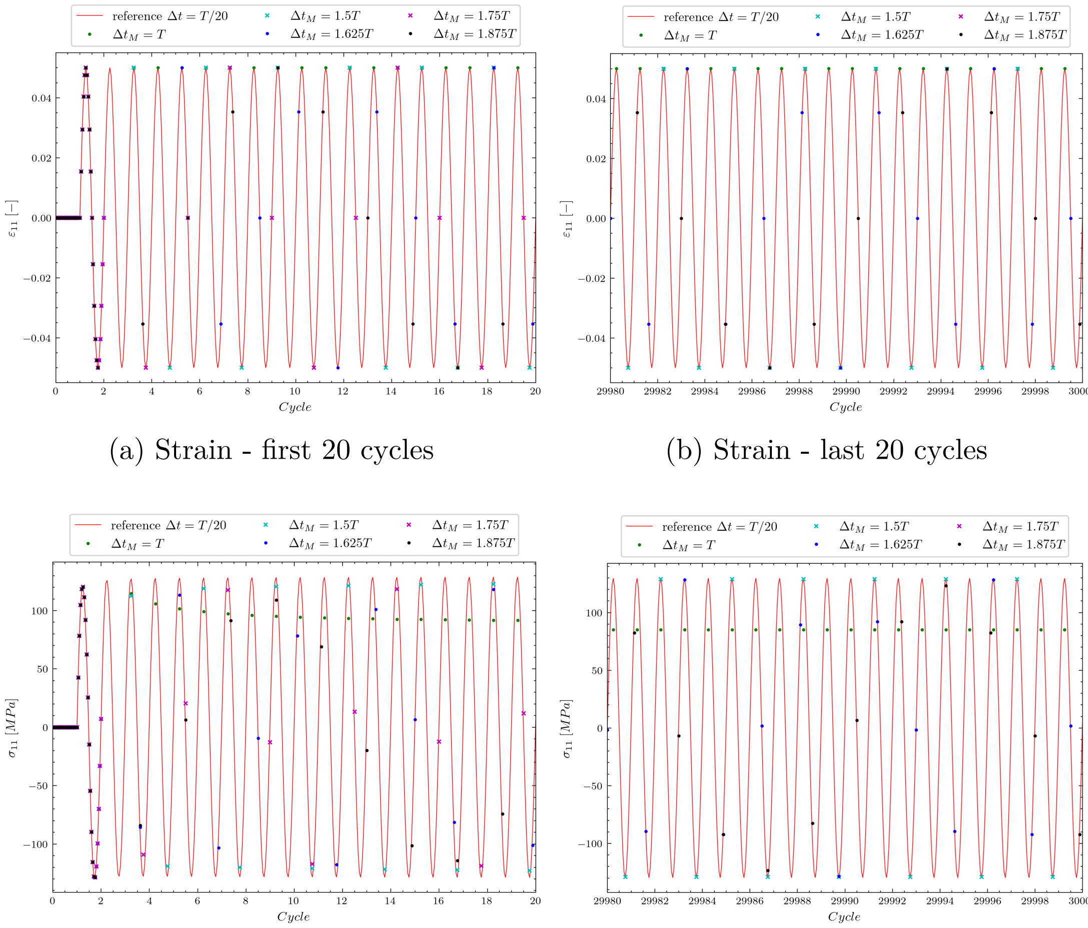

(a) Strain - first 20 cycles

(b) Strain - last 20 cycles

(c) Stress - first 20 cycles

(d) Stress - last 20 cycles

Figure 4.6: Evolution of stress and strain for different values of macro-time increment Δt_M, loading period: T = 0.1 s, loading ratio: R = -1.

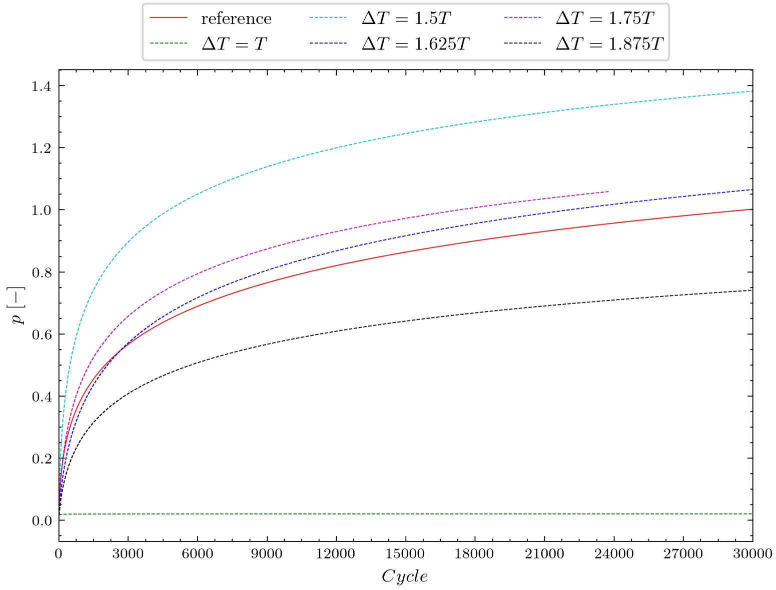

Figure 4.7: Evolution of the accumulated plastic strain for different values of macro-time increment Δt_M, loading period: T = 0.1 s, loading ratio: R = -1.

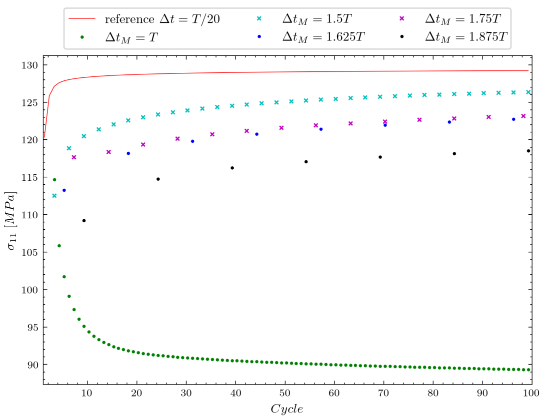

(a) The first 100 cycles

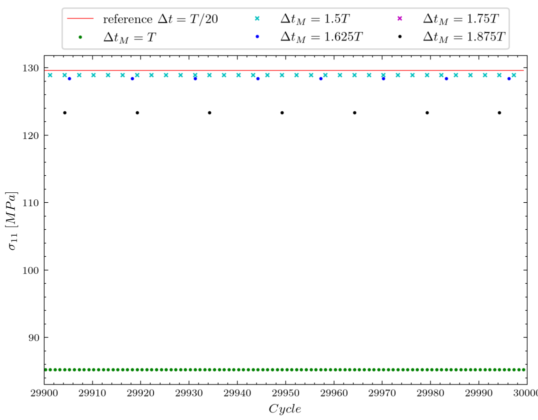

(b) The last 100 cycles

Figure 4.8: Evolution of the stress peaks for different values of macro-time increment Δt_M, loading period: T = 0.1 s, loading ratio: R = -1.

proposed value $\Delta t_M = 1.625T$ gives excellent predictions and the homogenized solution converges to the reference one for a high number of cycles.

The previous discussion leads to the adoption of a macro-time increment $\Delta t_M = 1.625T$ for the subsequent analyses, where this choice will be further validated. It is worth mentioning that the impressive accuracy demonstrated here is achieved with a relatively large time-step, which accelerates the computational time by approximately 30 times compared to the reference solution.

4.2 Method validation for heterogeneous material

The results presented in the previous section for a homogeneous material were quite satisfactory, so the next step is to validate the proposed coupled time and space homogenization method for the case of a heterogeneous RVE. The assessment of the accuracy of the method is crucial before moving to the prediction of fatigue tests.

In this section, a two-phase composite is considered consisting of a polyamide matrix reinforced with 30% volume fraction of aligned glass fibers. These fibers are oriented at a 45° angle relative to the injection flow direction (IFD) and have an aspect ratio of 23. The viscoelastic-viscoplastic (VE-VP) material parameters for the matrix were detailed in Table 4.1, whereas the elastic properties, the shape and orientation of the short glass fibers are given in Table 4.2. This configuration was studied by Haouala [8], so it is investigated here for validation purposes.

Young modulus	$E = 76GPa$
Poisson ratio	$\nu = 0.22$
Fiber orientation	$\theta = 45°$
Aspect ratio	$A = 23$
Volume fraction	$v_f = 30\%$

Table 4.2: Material and geometry parameters for elastic short glass fibers, adopted from [8].

The applied loading is given by Equation (4.1) and is the same imposed on the matrix material in Section 4.1. Here, only the case of $R = 0.1$ is studied and 10^5 cycles are applied.

Comparisons between the reference non-homogenized (full-time) calculation and the time-homogenized one are given in Figures 4.9–4.12. The predictions from [8] are also provided, in the cases that are available, for further validation.

The reference numerical solution is obtained using a very fine time step $\Delta t = \frac{T}{20}$, whereas the time-homogenized computation is started by a full calculation until time $t = \frac{7}{4}T$ and then the calculations are continued using Δt_M. The values of macro-time increment studied here are $\Delta t_M = T$ as in [8] and $\Delta t_M = 1.625T$, which was the optimal one according to the study of Section 4.1.3.

Figure 4.9 presents the evolution of the effective stress of the RVE and the stress in the matrix for the first and last 20 cycles. A careful examination leads to the following conclusions:

- There is a small discrepancy between the time-homogenized solution obtained here and the one from [8], despite using the same $\Delta t_M = T$. This slight difference, which was not observed in the homogeneous case, can be attributed to the difference in the formulation of space homogenization betwen the present method (incremental secant) and the one employed in [8] (integral affine).
- The time-homogenized predictions with the proposed $\Delta t_M = 1.625T$ are in good agreement with the reference solution even for a few cycles, which is remarkable.
- The stress prediction of time-homogenization is very good for a large number of cycles and the asymptotic expansion almost converges to the reference solution.
- As it was observed in the homogeneous case, time-homogenization with $\Delta t_M = T$ leads to a fast relaxation of the stress in the beginning of the time history (Remark 8).

Figure 4.10 shows the comparison of the evolution of accumulated plastic strain p in the VEVP matrix between the reference solution and the time-homogenized one with $\Delta t_M = T$ and $\Delta t_M = 1.625T$.After an initial sharp increase, corresponding to the application of the average part of the cyclic loading, p accumulates slowly cycle by cycle until it reaches a plateau value, indicating elastic shakedown. As p increases, the material hardens, raising the threshold for plasticity $(\sigma_y + R(p))$. Eventually, this threshold becomes equal to the amplitude of the applied loading, and further loading is purely viscoelastic.

Observing Figure 4.10 the agreement between the time-homogenized solution for $\Delta t_M = 1.625T$ and the reference one is at least remarkable. Although the increase is sharp and staircase-like during the first few cycles, it gradually approaches the reference solution as the number of cycles increases. This observation is in agreement with Remark 7 and validates once again the choice of this macro-time increment. On the other hand, the case of $\Delta t_M = T$ fails to capture accurately the shape of the evolution of p and gives poor predictions.

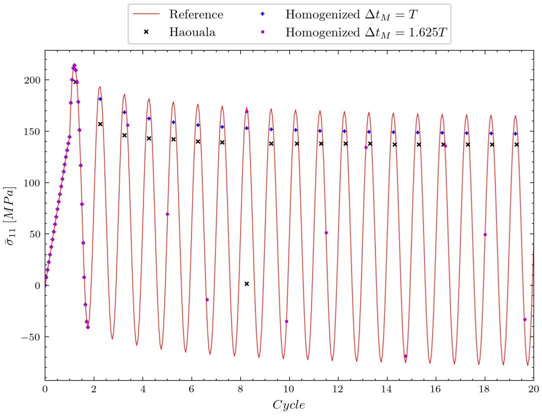

(a) Macro - first 20 cycles

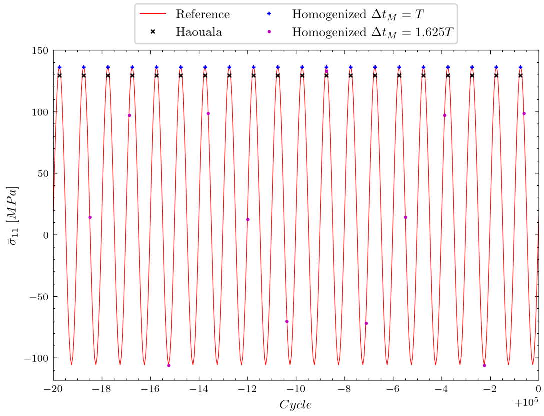

(b) Macro - last 20 cycles

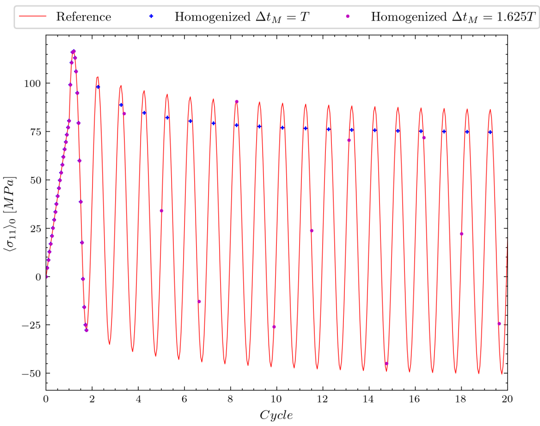

(c) Matrix - first 20 cycles

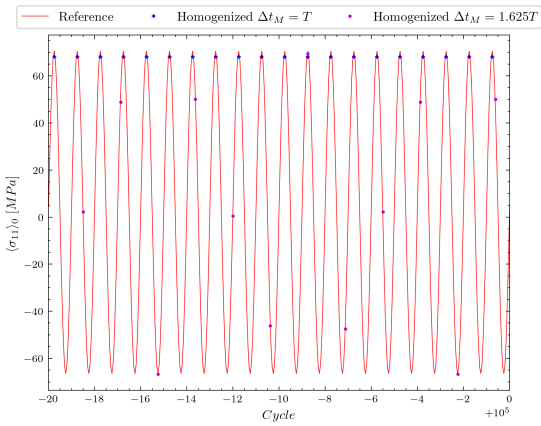

(d) Matrix - last 20 cycles

Figure 4.9: Evolution of the macroscopic stress and stress in the matrix: homogenized solution for two different values of macro-time increment Δt_M in comparison with reference results and results from [3], loading period: T = 0.1 s, loading ratio: R = 0.1.

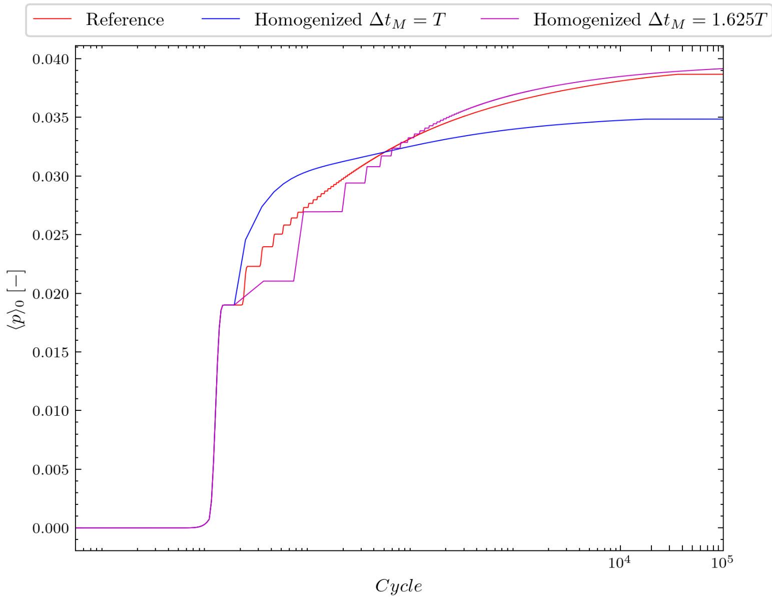

Figure 4.10: Evolution of the accumulated plastic strain: homogenized solution for two different values of macro-time increment Δt_M in comparison with reference results, loading period: T = 0.1 s, loading ratio: R = 0.1.

Figure 4.11 compares the predictions of the peaks of the macroscopic stress and the stress in the matrix for the first 100 cycles. Once again, the time-homogenized results with $\Delta t_M = 1.625T$ are in good agreement with the reference solution. Especially, the stress prediction in the VEVP matrix almost perfectly matches the reference. It is important to highlight why the points for $\Delta t_M = 1.625T$ are much sparser compared to those for $\Delta t_M = T$. This is because the stress peaks occur with a periodicity of 1 cycle for $\Delta t_M = T$, whereas they appear with a periodicity of 13 cycles for $\Delta t_M = 1.625T$.

In Figure 4.12, the effective stress-strain hysteresis loops for selected cycles are presented. The solid lines represent the reference results, while the black dots indicate the time homogenization predictions obtained with $\Delta t_M = 1.625T$. It is observed that, due to the repeated action of the relatively small applied strain, the stress level significantly decreases from a maximum of 200 MPa in the first cycle to around 150 MPa in subsequent cycles. Additionally, the stress-strain hysteresis loop rapidly "shrinks" with the number of cycles. It is worth noting once again that the time-homogenized results closely follow the reference solution almost from the beginning of the simulation.

In conclusion, the combined spatial and temporal homogenization formulation for VE-VP composites provides highly satisfactory predictions with a relative computational gain of approximately 97%. This result paves the way for fatigue

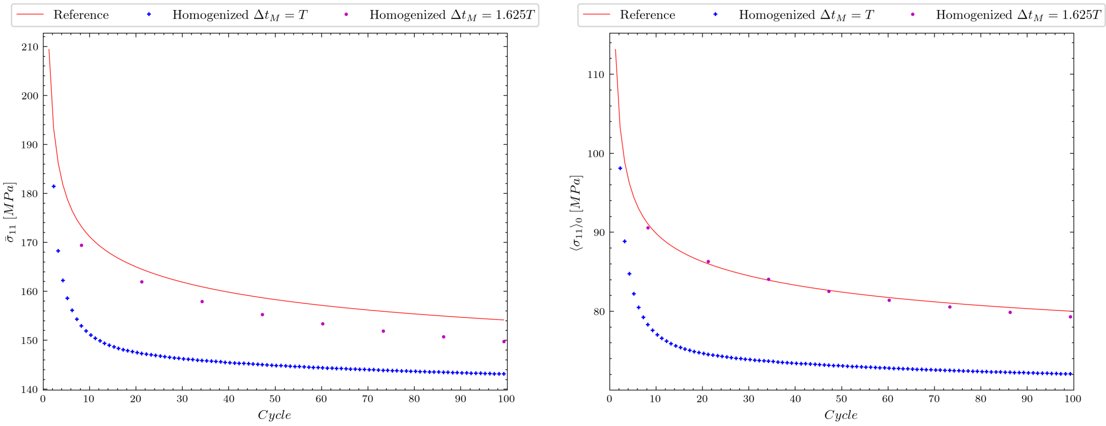

(a) Macro

(b) Matrix

Figure 4.11: Evolution of the stress peaks for two different values of macro-time increment Δt_M in comparison with reference results, loading period: T = 0.1 s, loading ratio: R = 0.1.

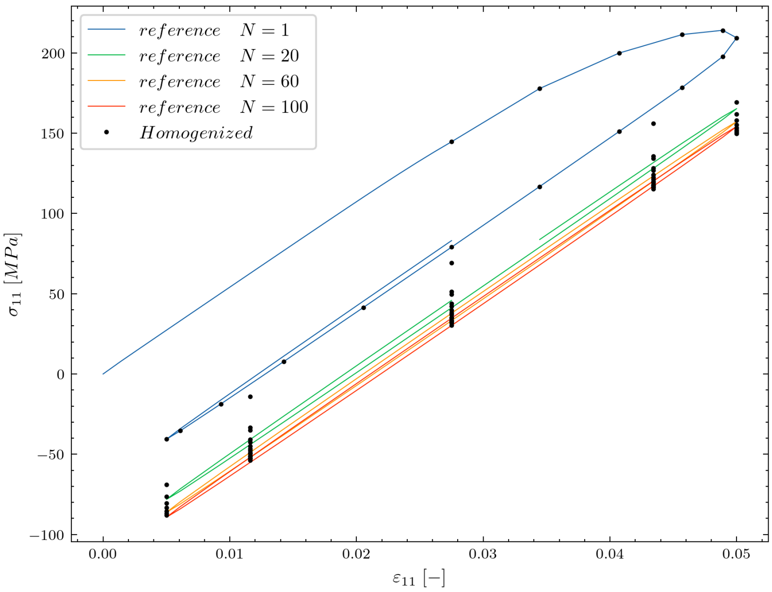

Figure 4.12: Hysteresis loops for macro response: First hundred cycles, loading period: T = 0.1 s, loading ratio: R = 0.1.

predictions in the high cycle fatigue (HCF) regime, which will be the focus of the next section.

4.3 Comparison of fatigue predictions with experimental results

4.3.1 Experimental results from fatigue tests and material properties

After the validation of the coupled time and space homogenization method, the methodology presented in Section 3 will be employed to predict the fatigue lifetime of experimental specimens. The tests were carried in JKU, which is a partner of the MOAMM project. The specimens tested consisted of two types: a notched specimen and a hollow specimen. The loading was uniaxial with period $T = 0.2sec$ and two loading ratios were examined: $R = -1$, which corresponds to a purely sinusoidal load with zero mean stress alternating between tension and compression, and $R = 0.1$, which involves a non-zero mean stress and is purely tensile. The tests, which were displacement-controlled, were carried out at different maximum amplitudes and each time the number of cycles to failure was recorded. The material is TPU printed using the SLS process, following the vertical direction (90°) at 20°C. The geometry of the specimens used and the experimental S-N curves are given in Figure 4.13.

4.3.2 TPU material model parameters

The identification of the material parameters of the VE matrix and the VEVP weak spots of TPU material, printed using the SLS process, following the vertical direction (90°) at 20°C was done as follows. Initially, polymer matrix properties without porosity were identified through Dynamic Mechanical Analysis (DMA) and uniaxial tensile tests at different strain rates. The identification of the VP parameters was done using the Digimat MX module, coupled with a VE-VP mean field homogenization (MFH) code, to minimize discrepancies between experimental results and model predictions, with VE properties the ones from DMA experiments.

Lacking experimental data at the weakspot level and following the suggestions given in [5], the following assumptions are made:

- The VE properties of both the matrix and weak spots are the same.
- The weak spots have a low yield stress and no hardening.
- The VP properties of the weakspots are the ones of the homogenized material.

(a) Notched specimen

(b) Hollow specimen

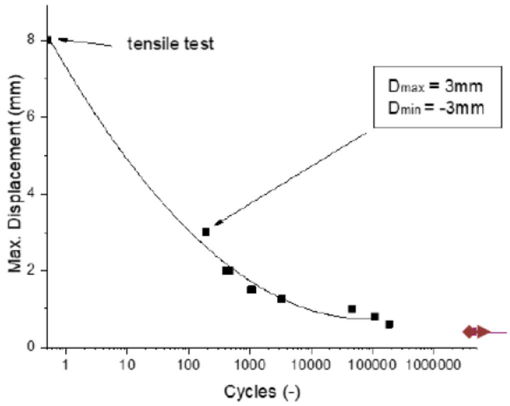

(c) Notched - $R = -1$

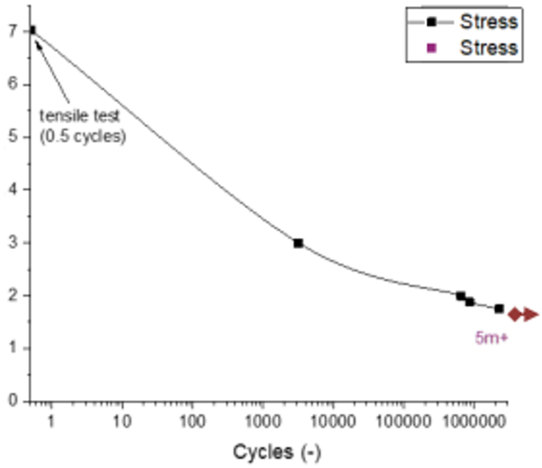

(d) Hollow - $R = -1$

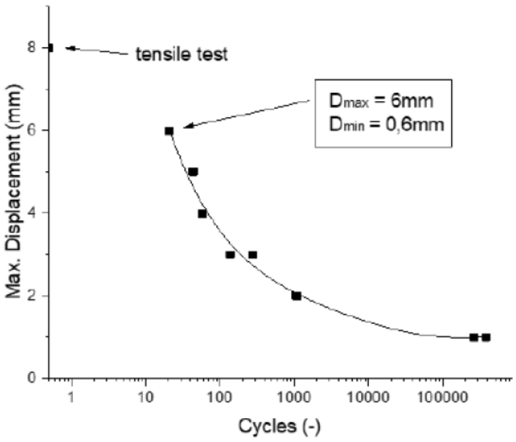

(e) Notched - $R = 0.1$

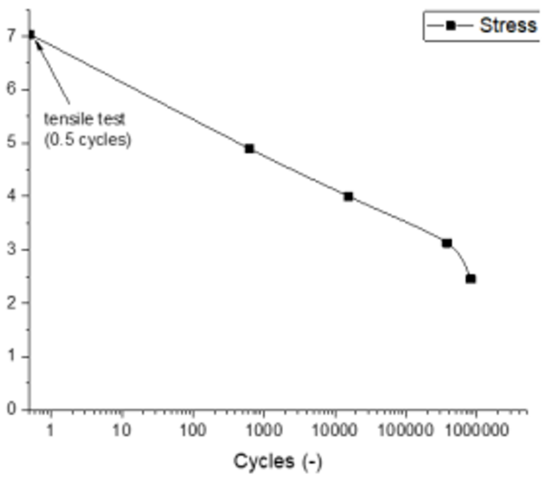

(f) Hollow - $R = 0.1$

Figure 4.13: S-N curves for notched and hollow specimens under uniaxial loading with loading ratios $R = 0.1$ and $R = -1$. The material is TPU printed using the SLS process, following the vertical direction (90°) at 20°C.

The identified material properties of the VE matrix and the VEVP weakspots are given in Table 4.4.

Matrix and weakspots			
Viscoelastic parameters			
Initial shear modulus	$G_0 = 34.1$MPa		
Initial bulk modulus	$K_0 = 73.9$MPa		
Poisson ratio	$nu = 0.3$		
G_i[MPa]	g_i[s]	K_j[MPa]	k_j[s]
3.42	$1.55{\cdot}10^{-2}$	472	$7.14{\cdot}10^{-3}$
3.08	$1.59{\cdot}10^{-3}$	242	$7.35{\cdot}10^{-4}$
4.26	$1.64{\cdot}10^{-4}$	111	$7.56{\cdot}10^{-5}$
Weakspots only			
Viscoplastic parameters			
Viscoplastic function	$\kappa = 2.01{\cdot}10^{-4}\text{s}^{-1}$	$m = 11.97$	
Yield stress	$\sigma_y = 1$MPa		

Table 4.3: Constitutive model parameters of VE matrix and VEVP weak spots of TPU material printed using the SLS process, following the vertical direction (90°) at 20°C.

4.3.3 Structural VE results

In the first step of the proposed methodology the structure is assumed purely VE with material properties given in Table 4.4 and the macroscopic strain history at the critical point of the structure is obtained using the Laplace-Carson transform. As critical point is chosen the integration point, which reaches the maximum value of equivalent strain at the steady state. Figures 4.14 and 4.15 compare the results obtained with the Laplace-Carson transform with direct full-field VE simulations with Abaqus for the first 4 cycles. The comparison is presented for the component of strain along the loading direction at the critical point of the structure. It is worth mentioning that the response reaches after only a few cycles the steady state.

With the exception of the first cycle, where the Abaqus simulation faces numerical problems during the first application of the loading, the agreement between the two methods is excellent. However, it should be pointed out that the direct VE simulations where the computational time scales linearly with the number of cycles simulated making this approach impractical for HCF. On the the other hand, the cost of the L-C method is independent of the number of cycles as the coefficients after the L-C inversion are computed only once and then the solution for any number of cycles can be retrieved rapidly.

4.3.4 Simulation of the notched specimen for loading ratio $R = 0.1$ and amplitude $U_{max} = 1mm$

The next step is the application of the macroscopic loading history to the RVE described in Section 3.1.1. The material properties of the VE matrix and the VEVP weakspots are the ones given in Table 4.4. Only one representative case is presented here, which corresponds to the notched specimen with a loading ratio of $R = 0.1$ and a maximum amplitude of $U_{max} = 1\,\text{mm}$.

The time-homogenized computation is started by a full calculation until time $t = \frac{7}{4}T$ and then the calculations are continued using $\Delta t_M = 1.625T$. The comparison of the evolution of the average stress in the weakspots for the first and last 20 cycles of the simulation between the time-homogenized solution with $\Delta t_M = 1.625T$ and the reference one obtained with a fine time-step $\Delta t = \frac{T}{20}$ is given in Figure 4.16. Once again, the excellent accuracy of the coupled time and space homogenization method is demonstrated.

Figure 4.17 presents the comparison of the evolution of the accumulated plastic strain p in the weakspots between the time-homogenized solution with $\Delta t_M = 1.625T$ and the reference one. The agreement is perfect and the two curves practically superpose. It is worth mentioning that time-homogenization results in an approximate 97% reduction in computational cost without compromising accuracy. It is also important to remark that a good prediction of the evolution of the accumulated plastic strain p is crucial for the accurate prediction of the fatigue life as the rate of damage directly depends on the rate of p in the damage model employed (Equation (2.17)).

4.3.5 Calculation of damage parameters with reverse-engineering

The last step of the methodology is the post-processing of the results of the coupled time and space homogenization for the calculation of the damage variable D in the weakspots as explained in Section 3.3. Figure 4.18 presents the evolution of the accumulated plastic strain p and damage variable D in the weakspots for the notched specimen with loading ratio $R = -1$ and maximum loading $U_{max} = 1mm$. The fatigue life N_f is defined as the moment when the damage D in the weakspots reaches its critical value D_c.

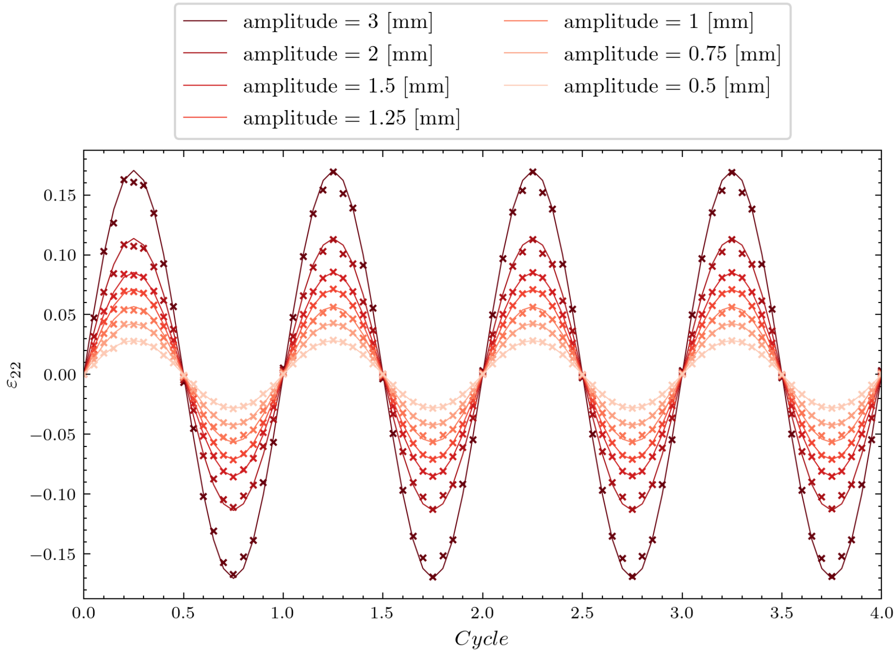

(a) Notched specimen - Loading ratio R = -1

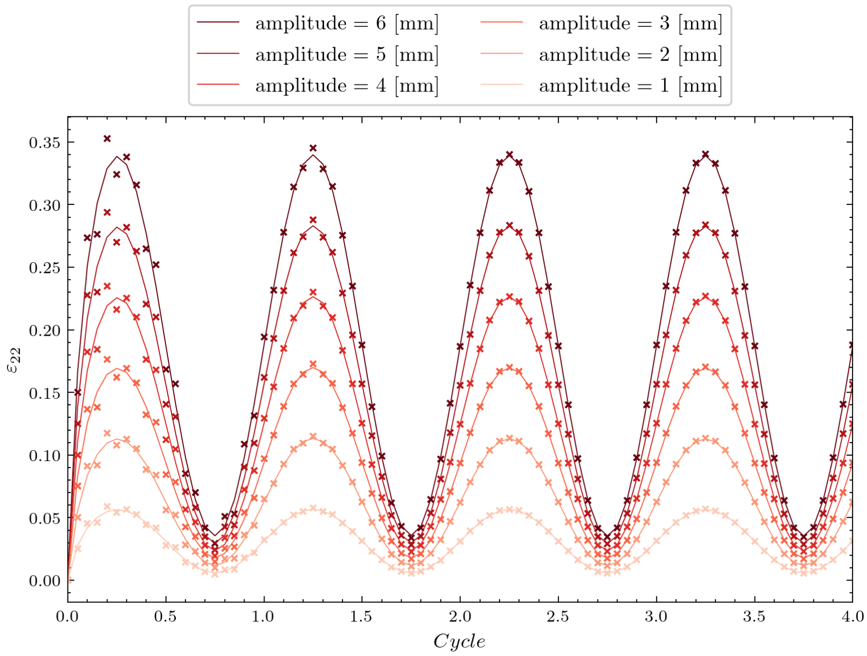

(b) Notched specimen - Loading ratio R = 0.1

Figure 4.14: Macroscopic strain $\overline{\varepsilon}_{22}$ at the critical point of the notched specimen for different loading amplitudes: Comparison of Laplace-Carson results (solid lines) with reference results from direct VE simulations with Abaqus (marked with x).

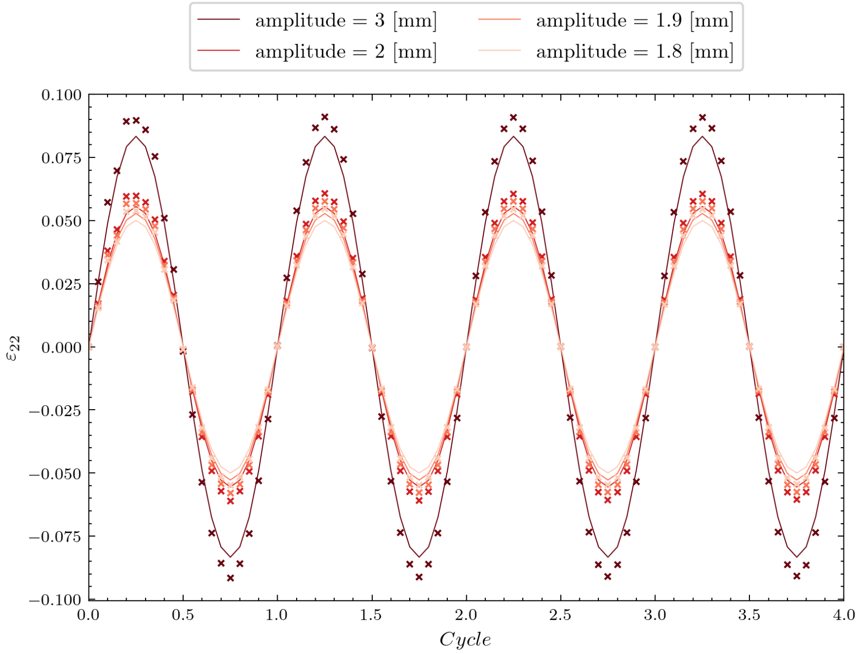

(a) Hollow specimen - Loading ratio R = -1

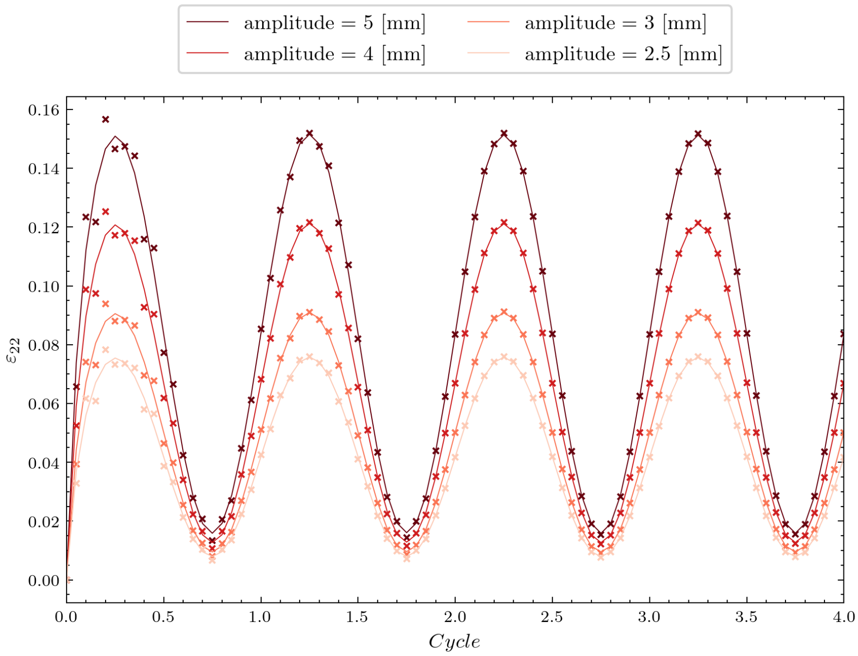

(b) Hollow specimen - Loading ratio R = 0.1

Figure 4.15: Macroscopic strain $\bar{\varepsilon}_{22}$ at the critical point of the hollow specimen for different loading amplitudes: Comparison of Laplace-Carson results (solid lines) with reference results from direct VE simulations with Abaqus (marked with x).

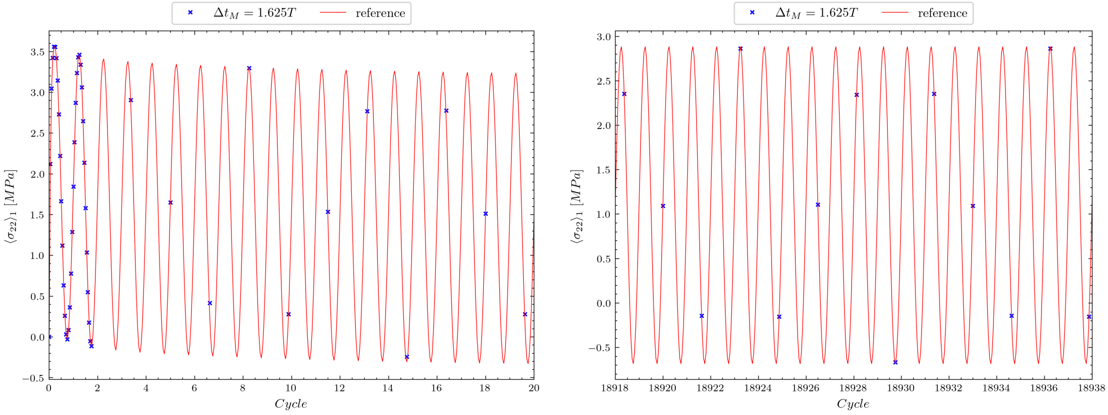

(a) The first 20 cycles

(b) The last 20 cycles

Figure 4.16: Evolution of the average stress in the weakspots for the notched specimen with loading ratio $R = 0.1$ and maximum loading $U_{max} = 1mm$: Comparison of reference with time-homogenized solution obtained with $\Delta t_M = 1.625T$.

The main problem here is that the damage parameters of the weakspots are not available. To overcome this issue, these parameters are going to be calculated from the experimental S-N curves by reverse engineering. The optimization problem is solved with a derivative-free simplex search optimization method (function fminsearch in Matlab). The objective function is the one RMSE of the logarithmic differences between numerical and experimental lifetime predictions, as it was described in Section 3.3. The damage variables chosen in the optimization are only S_d and s_d, because they had significant impact on the results, whereas D_c and p_d did not have an important influence and were given typical values (Table 4.4) to simplify the optimization problem. Another problem faced here was that in order the optimization to converge to an accurate solution, a relatively good initial guess was required. As a result, some "manual" searches of the optimization space were necessary to find a "promising neighborhood", before employing the optimization algorithm to calculate the optimal solution.

The identified values of the damage parameters of the weakspots as they were identified from the fatigue results of the notched specimen for loading ratio $R = -1$ and for amplitudes U_{max} 1.25, 1 and 0.75 mm.

After the identification of the optimal damage parameters in the weakspots, the final step is the evaluation lifetime predictions for the specimens that were not used in the optimization. The comparison between numerical and experimental S-N curves for the notched specimen with loading ratio $R = -1$ is presented in Figure 4.19. The agreement is quite satisfactory and the shape of the numerical curve seems to follow the experimental trend. It is remarkable that the numerical

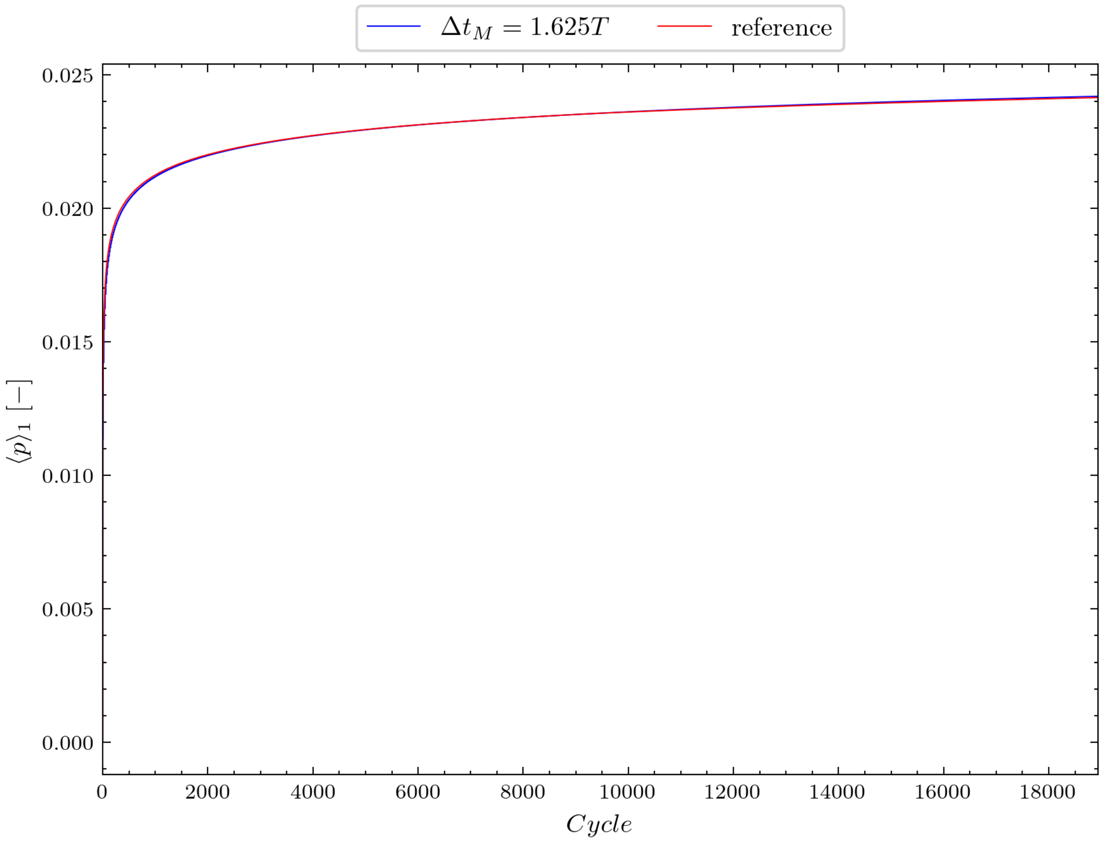

Figure 4.17: Evolution of accumulated plastic strain in weakspots for the notched specimen with loading ratio $R = 0.1$ and maximum loading $U_{max} = 1mm$: Comparison of reference with time-homogenized solution obtained with $\Delta t_M = 1.625T$.

S_d	s_d	D_c	p_d
173 MPa	0.718	0.25	0.0

Table 4.4: Damage parameters of weak spots identified from the fatigue results of the notched specimen for loading ratio $R = -1$ and for amplitudes U_{max} 1.25, 1 and 0.75 mm.

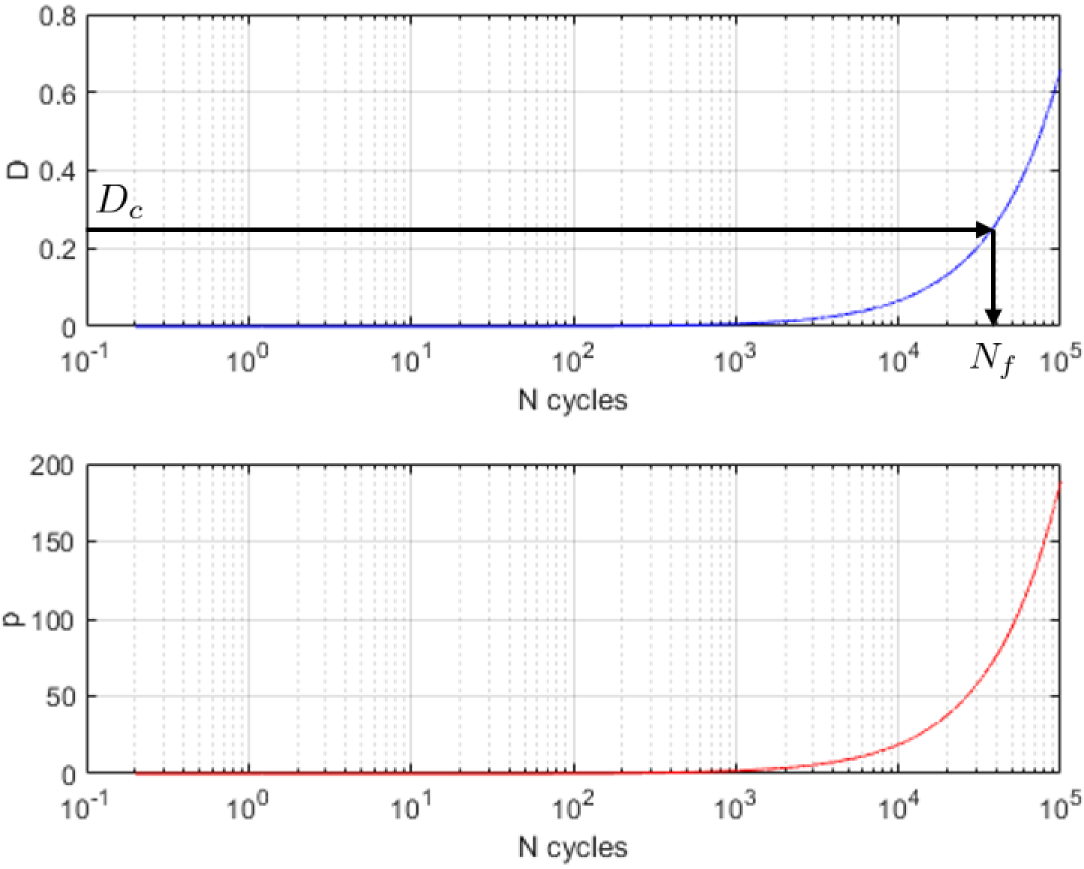

Figure 4.18: Evolution of accumulated plastic strain p and damage variable D in weakspots and calculation of the lifetime prediction for the notched specimen with loading ratio $R = -1$ and maximum loading $U_{max} = 1mm$.

method can provide good predictions of the lifetime of the specimens that were not included in the identification of the damage parameters.

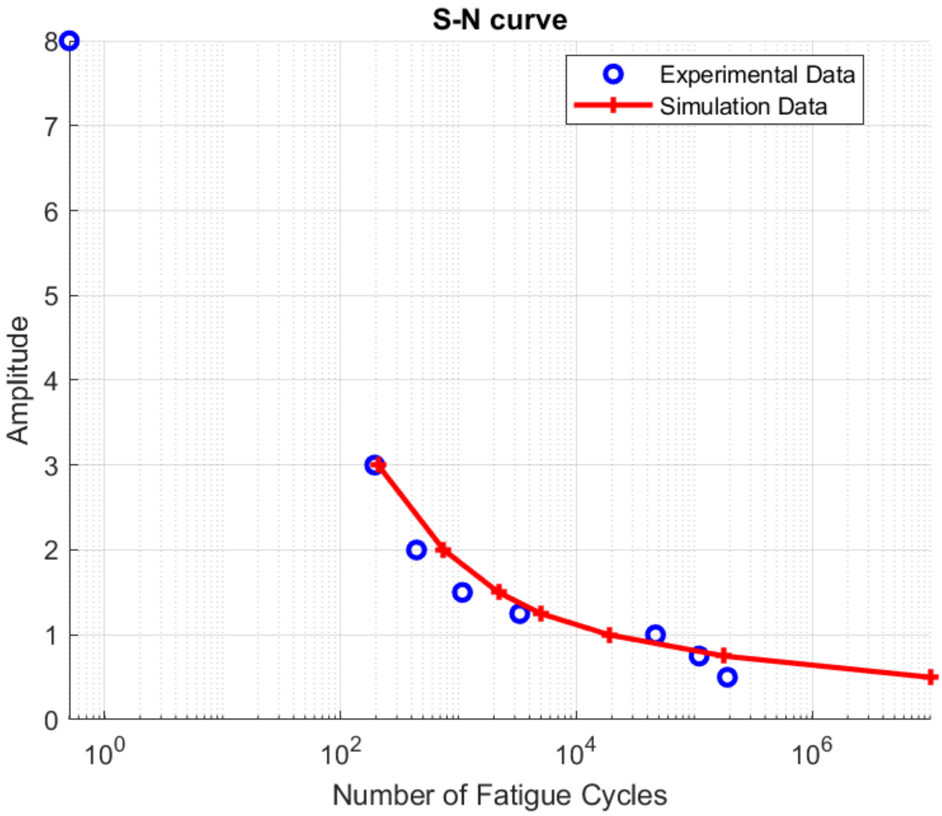

Figure 4.19: Numerical and experimental S-N curve for the notched specimen under uniaxial loading with loading ratio $R = -1$. The material is TPU printed using the SLS process, following the vertical direction (90°) at 20°C.

4.3.6 Fatigue predictions

In this Section, further fatigue lifetime predictions will be given for the other experimental cases. First, the evolution of the accumulated plastic strain p for the notched and hollow specimens for loading ratios $R = 0.1$ and $R = -1$ is given in Figures 4.20 and 4.21. Careful observation of these Figures leads to the following important remark:

Remark 9. *After a transient initial phase with a sharp increase, the accumulated plastic strain p reaches a steady state of almost linear increase with the number of cycles.*

The reason behind Remark 9 is that it was assumed that the weakspots do not have hardening, which means that the threshold for VP deformation is constant and equal to σ_y. On the other hand, the amplitude of the average stress stabilizes after a few cycles and obtains a roughly constant value as it was demonstrated in Figure 4.16. As a result, the rate of p is approximately constant according to Equation (2.13), which leads to a linear increase with the number of cycles.

Finally, the fatigue experiments not used in identifying the damage parameters have been predicted. The comparison between numerical and experimental S-N curves is given in Figure 4.22. Careful observation of Figure 4.22 leads to the following remarks:

- It is immediately evident that the accuracy of the predictions deteriorates when a different loading mode or geometry from that used in the identification of the damage parameters is examined. This could be because a set of damage parameters that provided good predictions for one specific case may not be effective for different geometries and loading conditions. In order to calculate more accurately the damage parameters of the weakspots, more points should be included in the optimization process. Moreover, some critical material parameters, such as the yield stress and the VP parameters of the weakspots, were assigned the values of the homogenized properties of the material. However, including these parameters in the optimization process and identifying them from the S-N curves through reverse engineering, as proposed in [5], would yield more accurate results. The computational cost would increase dramatically though, since these parameters affect the results of homogenization.

- Let us consider the case of same specimen geometry, but different applied loading ratio R. Comparison of Figures 4.22c and 4.22e shows that the predictions in the case of $R = 0.1$ (purely tensile loading) consistently overestimate the fatigue lifetime, when the damage parameters were identified based on the case of $R = -1$ (alternating tension-compression). This could be attributed to the fact that the damage model used here predicts does not distinguish between tension and compression loading (Equation (2.17)). This is a significant drawback, as compressive loading is far less damaging to the material compared to tensile loading.

- There are instances of good predictions even with different loading ratio R and specimen geometry (see Figures 4.22d and 4.22f). These promising results suggest that, with further refinement, the proposed modeling methodology could be applied to a wider range of cases.

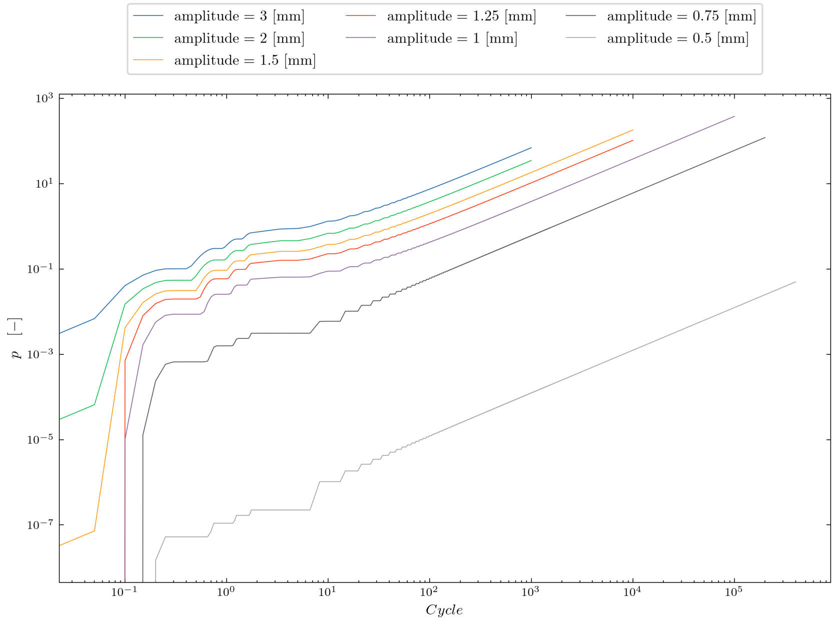

(a) Notched - $R = -1$

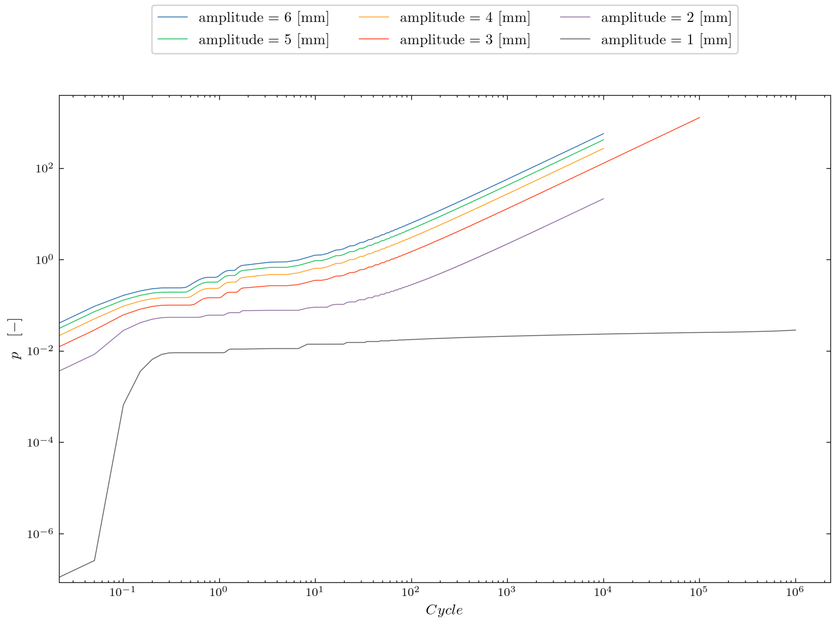

(b) Notched - $R = 0.1$

Figure 4.20: Evolution of accumulated plastic strain p for the notched specimen for loading ratios $R = 0.1$ and $R = -1$ and different values of U_{max}.

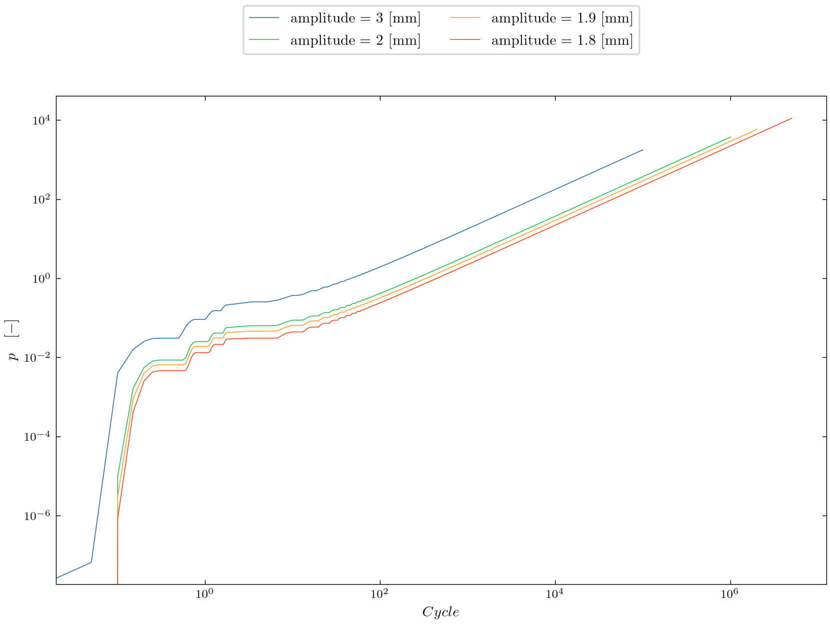

(a) Hollow - $R = -1$

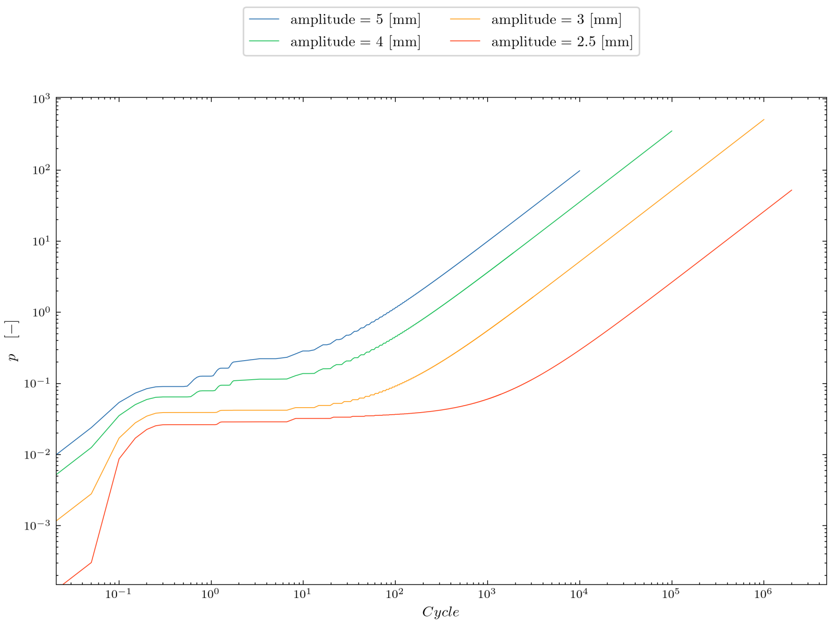

(b) Hollow - $R = 0.1$

Figure 4.21: Evolution of accumulated plastic strain p for the hollow specimen for loading ratios $R = 0.1$ and $R = -1$ and different values of U_{max}.

(a) Notched specimen

(b) Hollow specimen

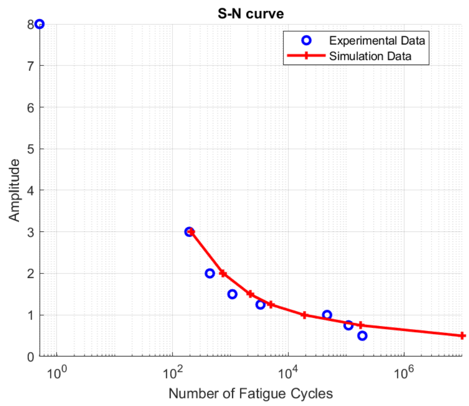

(c) Notched - $R = -1$

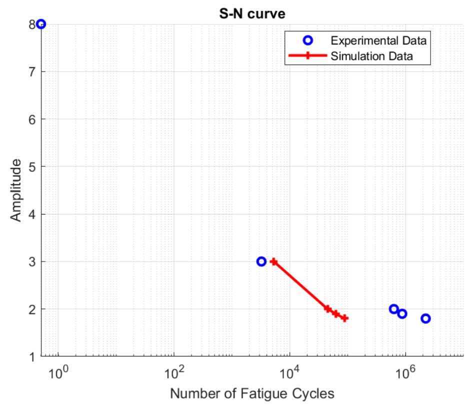

(d) Hollow - $R = -1$

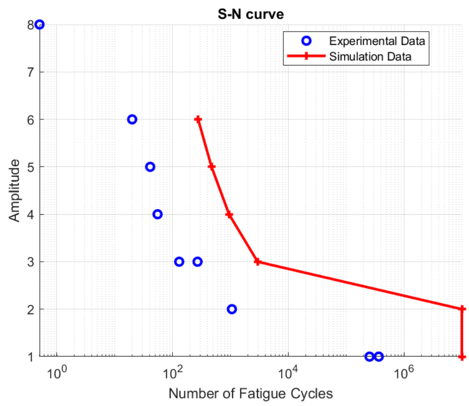

(e) Notched - $R = 0.1$

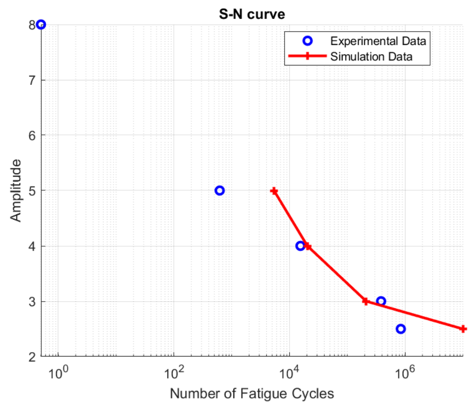

(f) Hollow - $R = 0.1$

Figure 4.22: Summary of numerical and experimental S-N curves for notched and hollow specimens under uniaxial loading with loading ratios $R = 0.1$ and $R = -1$. The material is TPU printed using the SLS process, following the vertical direction (90°) at 20°C.

Chapter 5

Conclusions

5.1 Summary of the key findings

In the present work, a novel methodology for the prediction of fatigue failure in thermoplastic polymer solids was presented. The key points can be summarized as follows:

- The main contribution was the formulation and implementation of a coupled time and space homogenization method for VEVP composites under cyclic loading. The proposed method presented remarkable accuracy in predicting the response inside the phases with a low computational cost even for a high number of applied cycles, paving the way for predictions in the HCF regime.

- The implementation of a non-integer macro-time increment addressed previous shortcomings of the time homogenization method. The study demonstrated that calculations at different points in subsequent cycles mimic micro-time averaging with multiple points, leading to significant improvements in the results. This approach was validated for various loading conditions and RVEs.

- The RVE modeling approach employed here was based on the assumption that in HCF the majority of the volume of the material remains viscoelastic and the viscoplastic deformation accumulates at the weakspots, which represent preexisting defects and inhomogeneities within the material. The developed coupled time and space homogenization scheme was utilized to predict the interaction between these weak spots, assumed to be VEVP, and the matrix. The proposed model demonstrated a strong capability to predict the response, while keeping the computational burden low.

- The overall procedure was implemented to predict the fatigue lifetime of specimens. The damage parameters of the weak spots were identified based on a few experimental results, and then the model was employed to make further predictions. The model accurately captured the dependence on loading amplitude. Additionally, there were instances of accurate predictions with different loading modes and specimen geometries. These promising results suggest that, with further refinement, the proposed modeling methodology could be applied to a broader range of cases.

5.2 Analysis of the limitations and potential improvements

Predicting fatigue life is a significant scientific challenge. Although the various proposed modeling approaches appear to effectively address the current issues, several recommendations are provided in the text to further enhance and broaden their validity domains. These recommendations are summarized below:

- One weak point of the proposed methodology is the assumption at the structural level that the macroscopic strain history obtained with a purely VE simulation is equivalent to the one of the actual VEVP material. A better approach would be to assume an energy equivalence between the VE and VEVP solutions, inspired from the Neuber rule for metals. However, additional conditions are needed to fully define all the components of the tensor.

- Another weakness of the proposed methodology is that the damage model is decoupled and is utilized in a post-processing manner. A more accurate approach would be to employ a fully coupled VEVPD model for the weak spots as presented in [10]. However, this would require overcoming two problems. First, it would be necessary to extend the developed coupled time and space homogenization method to the case of VEVPD composites. Second, and most importantly, the computational cost for one evaluation of the objective function would increase dramatically, since each trial set of damage parameters would require a new solution with the MFH algorithm. As a result, the reverse engineering process would be much more time-consuming.

- A limitation of the damage model used here is the lack of distinction between tension and compression, assuming both are equally damaging. However, this is inaccurate, as tensile loading is significantly more damaging than compressive loading and a modification of the damage model to account for this effect is necessary to improve the fatigue predictions.

- It was observed that obtaining a good optimal solution required a reliable initial guess to ensure the optimization method converged to the optimal set of damage parameters of the weakspots. Additionally, improving the optimization results might necessitate including more data points in the process, especially for fatigue data with different geometries and loading modes. Furthermore, the yield stress and VP parameters were found to significantly influence the predictions, suggesting that incorporating them into the optimization process could lead to major improvements, but at the cost of increased computational time. Taking all these factors into account, a global optimization method, such as a genetic algorithm, might be more suitable for exploring the optimization space and achieving a better solution. However, this approach would require significantly larger computational resources.

- Further validation of the proposed modeling approach against additional experimental results is necessary. The current model should be tested under more complex multiaxial loading conditions, such as combined tension and torsion.

Bibliography

[1] Mohamed Haddad Darith Anthony Hun and Issam Doghri. Modeling and simulation of viscoelastic solids under large numbers of loading cycles. *Mechanics of Advanced Materials and Structures*, 30(8):1542–1558, 2023.

[2] Mohamed Haddad, Issam Doghri, and Olivier Pierard. Viscoelastic-viscoplastic polymer composites: development and evaluation of two very dissimilar mean-field homogenization models. *International Journal of Solids and Structures*, 236-237, 11 2021.

[3] Sarra Haouala and Issam Doghri. Modeling and algorithms for two-scale time homogenization of viscoelastic-viscoplastic solids under large numbers of cycles. *International Journal of Plasticity*, 03 2015.

[4] M. Kamal and M.M. Rahman. Advances in fatigue life modeling: A review. *Renewable and Sustainable Energy Reviews*, 82:940–949, 2018.

[5] Anouar Krairi and Issam Doghri. A thermodynamically-based constitutive model for thermoplastic polymers coupling viscoelasticity, viscoplasticity and ductile damage. *International Journal of Plasticity*, 60:163–181, 2014.

[6] Zoltan Major, Michael Lackner, Anna Hössinger-Kalteis, and Thomas Lück. Characterization of the fatigue behavior of sls thermoplastics. *Procedia Structural Integrity*, 34:191–198, 2021. The second European Conference on the Structural Integrity of Additively Manufactured Materials.

[7] Anouar Krairi. *Multiscale modeling of the damage and failure of homogeneous and short-fiber reinforced thermoplastics under monotonic and fatigue loadings*. PhD thesis, Université catholique de Louvain, Ecole polytechnique de Louvain, Institute of Mechanics, Materials and Civil Engineering, 2015.

[8] Sarra Haouala. *Time and space (4D) homogenization for viscoelastic-viscoplastic solids under large numbers of cycles.* PhD thesis, Université catholique de Louvain, Ecole polytechnique de Louvain, Institute of Mechanics, Materials and Civil Engineering, 2016.

[9] L. Cobian, M. Rueda-Ruiz, J.P. Fernandez-Blazquez, V. Martinez, F. Galvez, F. Karayagiz, T. Lück, J. Segurado, and M.A. Monclus. Micromechanical characterization of the material response in a pa12-sls fabricated lattice structure and its correlation with bulk behavior. *Polymer Testing*, 110:107556, 2022.

[10] Bilel Miled, Issam Doghri, and Laurent Delannay. Coupled viscoelastic–viscoplastic modeling of homogeneous and isotropic polymers: Numerical algorithm and analytical solutions. *Computer methods in applied mechanics and engineering*, 200(47-48):3381–3394, 2011.

[11] John Douglas Eshelby and Rudolf Ernst Peierls. The determination of the elastic field of an ellipsoidal inclusion, and related problems. *Proceedings of the Royal Society of London. Series A. Mathematical and Physical Sciences*, 241(1226):376–396, 1957.

[12] T Mori and K Tanaka. Average stress in matrix and average elastic energy of materials with misfitting inclusions. *Acta Metallurgica*, 21(5):571–574, 1973.

[13] L. Wu, L. Noels, L. Adam, and I. Doghri. A combined incremental-secant mean-field homogenization scheme with per-phase residual strains for elasto-plastic composites. *International Journal of Plasticity*, 51:80–102, 2013.

[14] Guennouni, Tajeddine. Sur une méthode de calcul de structures soumises à des chargements cycliques : l'homogénéisation en temps. *ESAIM: M2AN*, 22(3):417–455, 1988.

[15] Alain Bensoussan, Jacques-Louis Lions, and George Papanicolaou. *Asymptotic analysis for periodic structures*, volume 374. American Mathematical Soc., 2011.

UNIVERSITÉ CATHOLIQUE DE LOUVAIN
École polytechnique de Louvain
Rue Archimède, 1 bte L6.11.01, 1348 Louvain-la-Neuve, Belgique | **www.uclouvain.be/epl**